Norwegian University
of Life Sciences

Master's Thesis 2022 60 ECTS
Faculty of Chemistry, Biotechnology, and Food Science

The Roles of Conserved Second Sphere Residues in Lytic Polysaccharide Monooxygenase Catalysis

Maja Mollatt
Master of Science, Biotechnology

Acknowledgments

The research presented in this thesis was part of a larger international project and performed for the Bioorganic Chemistry group and the Protein Engineering and Proteomics group at the Faculty of Chemistry, Biotechnology and Food Science at the Norwegian University of Life Sciences. The work was supervised by Professor Morten Sørlie and Dr. Kelsi Hall.

First, I would like to thank my main supervisor Professor Morten Sørlie for giving me the opportunity to be a part of this exciting project and for introducing me to the field of LPMOs. I really appreciate your guidance, and I thank you for always making me feel extremely motivated and excited after our conversations and scientific discussions.

A special thanks to my co-supervisor Dr. Kelsi Hall. I would like to express my utter most gratitude to you. I am so thankful for all the valuable time you have spent helping me with everything from lab work to scientific discussions. Your guidance in the laboratory have helped me to achieve and understand the results in this thesis. I greatly appreciate your fast feedback on my writing, your willingness to teach, and how you encourage and inspire me.

I would also like to thank Dr. Ivan Ayuso-Fernandez and Ole Golten for always taking time to answer my questions, for encouragement, and good conversations. In addition, I would like to thank all the members of the Bioorg and the PEP group for their willingness to help me with any problem I bring to the table.

A special thanks to Rannei Skaali, this year would not have been the same without your friendship and company in the lab. Special thanks to Marianne Sundet Frøseth for the friendship and laughs throughout these five years at NMBU. I would also like to thank my fellow master students in the study room for the lunches, walks around the pond, and evenings spent writing.

Finally, I would like to thank my family for always supporting me and encouraging me to go after my dreams. Thank you for all the laughter and conversation around the dinner table, and for helping me find my path. Frank, my better half, thank you for making me laugh when I cry, for cheering me on, for reminding me of what is important, and for patiently and curiously listening to my enthusiastic talks about my thesis work. Life would not have been the same without you.

Maja Mollatt

May 2022, Ås

Acknowledgments

Summary

The demand for sustainable and renewable options to generate energy and materials is increasing as we become more aware of the environmental impact of a petroleum-based economy. Biomass may be employed as a sustainable alternative and consists of recalcitrant polysaccharides. Key enzymes for disruption of crystalline polysaccharides, such as cellulose and chitin, are lytic polysaccharide monooxygenases (LPMOs). LPMOs are copper-dependent enzymes, and the catalytic mechanism is initiated by a reduction of the copper atom, coordinated in a *histidine brace*. Other residues in the catalytic center, termed second sphere residues, are not extensively studied but are likely involved in the catalytic mechanism resulting in oxidative cleavage of glycosidic bonds. Insight into how these residues affect LPMO activity may yield valuable information for optimization of polysaccharide degradation. Therefore, we aimed to investigate the interactions between and function of three second sphere residues (YQH) in cellulose-active *Ma*LPMO10B. The second sphere motif of *Ma*LPMO10B WT was mutated into the second sphere motif (FER) found in two other cellulose-active LPMOs; mgLPMO10 and *Sc*LPMO10C. Each *Ma*LPMO10B protein was assigned an amino acid code corresponding to the second sphere residues of the respective protein, e.g., YQH for *Ma*LPMO10B wild type (WT).

Eight *Ma*LPMO10B mutant proteins were generated, and several enzyme characterization assays were performed to compare the effect of the mutations with *Ma*LPMO10B WT. All *Ma*LPMO10B mutants displayed lower activity towards cellulose than *Ma*LPMO10B WT. The YEH mutant displayed higher activity towards chitin than *Ma*LPMO10B WT. This mutant also had a faster rate of oxidized cello-oligosaccharide formation and an increased generation of hydrogen peroxide *in situ*. The two other single mutants, YQR and FQH, displayed a slow rate for production of oxidized cello-oligosaccharides and a low oxidase activity but remained stable throughout the reaction time. The three double mutants inactivated prematurely, and the FEH mutant had a slow rate of oxidized product formation, whereas the rate at which the YER and the FQR mutants generated oxidized cello-oligosaccharides was fast. Both mutants with an FER second sphere motif appeared less stable upon oxidized product formation. Differences in oxidase activity were observed between the two FER mutants, mgLPMO10, and *Sc*LPMO10C, that have FER as their natural second sphere motif.

The second aim of this thesis was to study the effect of changing pH and type of reductant on the activity of *Ma*LPMO10B WT and the YEH mutant. The rate of oxidized cello-oligosaccharide formation increased from pH 6 to pH 8 when ascorbic acid or gallic acid were used as reductants. The opposite was observed when the reductant was cysteine. *Ma*LPMO10B WT appeared to withstand changes in pH better than the YEH mutant, which showed optimal activity at pH 6.

In this thesis, we show that the second sphere residues are essential for LPMO activity, and that pH and type of reductant used have a significant impact on the efficiency of LPMO catalysis. Moreover, we demonstrate that a glutamine to glutamate mutation in the presence of a tyrosine residue (YE) instead of a phenylalanine residue (FE) significantly improves *in situ* production of hydrogen peroxide. This knowledge is important to optimize LPMO activity for industrial applications.

Sammendrag

Bærekraftige og fornybare alternativer for å skape energi og materialer øker i etterspørsel ettersom vi blir mer oppmerksomme på miljøeffekten av en petroleumsbasert økonomi. Biomasse kan fungere som et bærekraftig alternativ og består av svært hardføre polysakkarider. Nøkkelenzymer for å bryte opp krystallinske polysakkarider, som cellulose og kitin, er lytisk polysakkarid monooksygenaser (LPMOer). LPMOer er kobber-avhengige enzymer, og den katalytiske mekanismen blir initiert ved reduksjon av kobberatomet som er koordinert av to histidiner. Andre aminosyrer i det aktive setet, andresfære residuer, har ikke blitt forsket mye på, men er mest sannsynlig involvert i den katalytiske mekanismen som resulterer i oksidativ spalting av glykosidbindinger. Innsikt om hvilken effekt disse aminosyrene har på LPMO aktivitet kan gi verdifull informasjon for optimalisering av polysakkarid nedbrytning. Målet vårt var derfor å studere hvordan andresfære residuene (YQH) i celluloseaktive *Ma*LPMO10B fungerer og interagerer med hverandre. Andresfære motivet i *Ma*LPMO10B villtype (WT) ble mutert til andresfære motivet (FER) som finnes i to andre celluloseaktive LPMOer; mgLPMO10 og *Sc*LPMO10C. Hvert *Ma*LPMO10B protein fikk tildelt en aminosyrekode som korresponderer til andresfære residuene i det respektive proteinet, for eksempel YQH for *Ma*LPMO10B villtype (WT).

Flere enzymatiske karakteriseringsanalyser ble utført for å sammenlikne effekten av mutasjonene med *Ma*LPMO10B WT. Alle *Ma*LPMO10B mutantene viste lavere aktivitet for cellulose enn *Ma*LPMO10B WT. YEH mutanten viste høyere aktivitet for kitin enn *Ma*LPMO10B WT. Denne mutanten produserte også oksiderte cellulose oligosakkarider raskere og genereringen av hydrogenperoksid *in situ* økte. De to andre enkeltmutantene, YQR og FQH, dannet oksiderte cellulose oligosakkarider sakte og hadde lav produksjon av hydrogenperoksid, men var stabile gjennom hele reaksjonstiden. De tre dobbelmutantene ble inaktivert før reaksjonstiden var omme, og FEH mutanten genererte oksiderte cellulose oligosakkarider sakte, mens YER og FQR mutantene dannet oksiderte cellulose oligosakkarider raskt. Begge mutantene som hadde et FER andresfære motiv virket å være mindre stabile under produktdannelse. Forskjeller i oksidaseaktivitet ble observert mellom de to mutantene med FER motiv, mgLPMO10, og *Sc*LPMO10C som har FER som deres naturlige andresfære motiv.

Det andre målet for denne mastergradsavhandlingen var å studere effekten endring av pH og type reduktant hadde på aktiviteten til *Ma*LPMO10B WT og YEH mutanten. Fra pH 6 til pH 8 økte hastigheten for generering av cellulose oligosakkarider når askorbinsyre og gallussyre ble brukt som reduktanter. Det motsatte ble observert når cystein ble brukt som reduktant.

*Ma*LPMO10B WT virket å motstå endringer i pH bedre enn YEH mutanten, som viste optimal aktivitet ved pH 6.

I denne mastergradsavhandlingen viser vi at andresfære residuene er essensielle for LPMO aktivitet, og at pH og type reduktant som blir brukt har en signifikant påvirkning på effektiviteten i LPMO katalyse. Vi viser også at en glutamin til glutamat mutasjon sammen med en tyrosin (YE) i stedet for en fenylalanin (FE) gir en signifikant økning av *in situ* produksjon av hydrogenperoksid. Denne kunnskapen er viktig for å optimalisere LPMO aktivitet i industrielle applikasjoner.

Abbreviations

2,6-DMP	2,6-dimethoxyphenol
AA	Auxiliary activity
bp	Base pair
CAZy	Carbohydrate active enzyme
CBH	Chitobiase
CBM	Carbohydrate-binding module
CBP21	Chitin-binding protein 21
CDH	Cellobiose dehydrogenases
ddH_2O	Double distilled water
DNA	Deoxyribonucleic acid
dNTP	Deoxyribonucleoside triphosphate
DP	Degree of polymerization
EDTA	Ethylenediaminetetraacetic acid
g	Relative centrifugal force
GH	Glycoside hydrolase
Hj	*Hypocrea jecorina*
HPAEC-PAD	High-performance anion exchange chromatography with pulsed amperometric detection
ICS	Ion chromatography system
kb	Kilobase
kDa	Kilodalton
LB	Lysogeny broth
LPMO	Lytic polysaccharide monooxygenase
Ls	*Lentinus similis*
Ma	*Micromonospora aurantiaca*
mAU	Milli absorbance units
mg	metagenome
MWCO	Molecular weight cut off
Nc	*Neurospora crassa*
PASC	Phosphoric acid swollen cellulose
PCR	Polymerase chain reaction

pI	Isoelectric point
PIPES	Piperazine-N,N’-bis(2-ethanesufonic acid)
PMSF	Phenylmethylsulphonyl fluoride
Rpm	Revolutions per minute
Sc	*Streptomyces coelicolor*
SDS-PAGE	Sodium dodecyl sulfate-polyacrylamide gel electrophoresis
SEC	Size exclusion chromatography
Sm	*Serratia marcescens*
SOC	Super optimal broth
Ta	*Thermoascus aurantiacus*
TB	Terrific broth
Tf	*Thermobifida fusca*
TMP	N,N,N’,N’-tetramethyl-1,4-phenylenediamine
Tr	*Trichoderma reesei*
UHPLC	Ultra high-performance liquid chromatography
UV	Ultraviolet
w/v	Weight/volume
WT	Wild type

Table of contents

1 Introduction

We are currently standing in a global climate crisis. Extreme weather increase in severity and frequency, making growth of crops and food more unpredictable. Virus pandemics hit close to home and self-sufficiency and sustainability become more important than ever. This is a consequence of greenhouse gas emission from non-renewable energy sources such as fossil fuels (Vanholme *et al.*, 2013). The urge for a renewable option to drive a bio-based economy and as a source of energy is therefore of wide interest. First generation feedstocks, such as sugars from starch or sucrose, were suggested as a sustainable and renewable energy source. However, these resources serve as food crops and were not a favorable option (Williams, 2008). Second generation feedstock, namely biomass from plants, were therefore introduced as an alternative (Vanholme *et al.*, 2013).

Biomass consists mainly of plant cell walls rich in carbohydrate polysaccharides (Duchesne & Larson, 1989). The biomass components cellulose and chitin are the two most abundant carbohydrates in Nature, but their crystalline structure makes degradation challenging. However, the carbohydrates may be derived from biomass by chemical or physical pretreatment, then degraded by enzymatic treatment. Enzymatic treatment includes degradation of the polysaccharides by carbohydrate active enzymes such as glycoside hydrolases (GHs) and lytic polysaccharide monooxygenases (LPMOs) and result in fermentable sugar units. The fermentable sugar units may be used to yield chemicals or biofuels, such as bioethanol, and thus reduce the demand for fossil fuels (Sharma *et al.*, 2019).

1.1 Carbohydrates

Carbohydrates are biomolecules that mainly consist of carbon, hydrogen, and oxygen. The three elements are arranged as ring structures with hydroxyl groups and an aldehyde or ketone group. Carbohydrates can be divided into mono-, di-, oligo-, and polysaccharides, where monosaccharides consisting of a single polyhydroxy aldehyde or ketone unit are the building blocks. Disaccharides consist of two monosaccharide units, while oligosaccharide consist of up to 20 units. Polysaccharides have more than 20 monomeric units and the monomers are linked by glycosidic bonds. Cellulose and chitin are the two most abundant carbohydrates on Earth and play a key role in the replacement of fossil fuels as a more sustainable and renewable source of energy and materials.

1.1.1 Cellulose

Cellulose is a recalcitrant polysaccharide mainly found in plant cell walls and consists of D-glucose units. The glucose units are linearly linked with β-1,4-glycosidic bonds where the monomers are rotated 180 ° relative to one another, resulting in a repetitive cellobiose unit (Figure 1) (Zugenmaier, 2001). The chain of glucose monomers is unbranched and when more than eight glucose monomers are linked, the cellulose is no longer soluble (Brown, 2004). This is because the cellulose chains will have higher affinity towards one another compared to water and hydrogen bonding between the oligomers will stabilize the interactions of the chains (Vanderhart & Atalla, 1984). Microfibrils, stabilized by van der Waals forces and hydrogen bonding, are then generated by aggregation of the cellulose chains (Parthasarathi *et al.*, 2011).

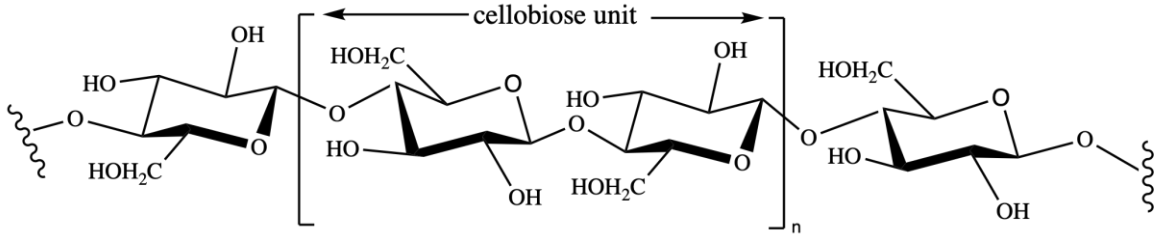

Figure 1. The non-branched cellulose chain. *D-glucose monomers linked by β-1,4-glycosidic bonds 180 ° relative to one another, resulting in the cellobiose unit. The figure is derived from unpublished work.*

Several types of cellulose polymorphs exist and are divided into cellulose I, II, III, and IV (O'Sullivan, 1997). Cellulose I is found in plant cell walls as the only naturally occurring cellulose polymorph, while cellulose II, III, and IV are synthetical derivatives (O'Sullivan, 1997). Naturally occurring cellulose I is arranged in parallel chains consisting of cellulose Iα and cellulose Iβ, which differ in their hydrogen bonding pattern (Nishiyama *et al.*, 2002; Nishiyama *et al.*, 2003; Vanderhart & Atalla, 1984). Cellulose II can be generated by alkaline treatment of cellulose I and have anti-parallel arrangement of the cellulose chains (Gardner & Blackwell, 1974; O'Sullivan, 1997). Cellulose III may be derived from either cellulose I or II, while cellulose IV is generated from heating of cellulose III in glycerol (O'Sullivan, 1997). The degree of crystallinity varies among and within cellulose polymorphs. Some areas will be more densely packed, giving a high degree of crystallinity, while other areas consist of amorphous cellulose (O'Sullivan, 1997).

1.1.2 Chitin

Chitin is abundant in the cell walls of fungi and in the hard shell of insects, crabs, and shrimps. The unbranched polysaccharide resembles cellulose as N-acetyl-D-glucosamine monomers are linked by β-1,4-glycosidic bonds (Figure 2) (Zikakis, 1984). The N-acetyl-D-glucosamine units are arranged 180 ° relative to each other, as the D-glucose monomers of cellulose (Gooday, 1990). This results in a repetitive *N,N'*-diacetylchitobiose unit.

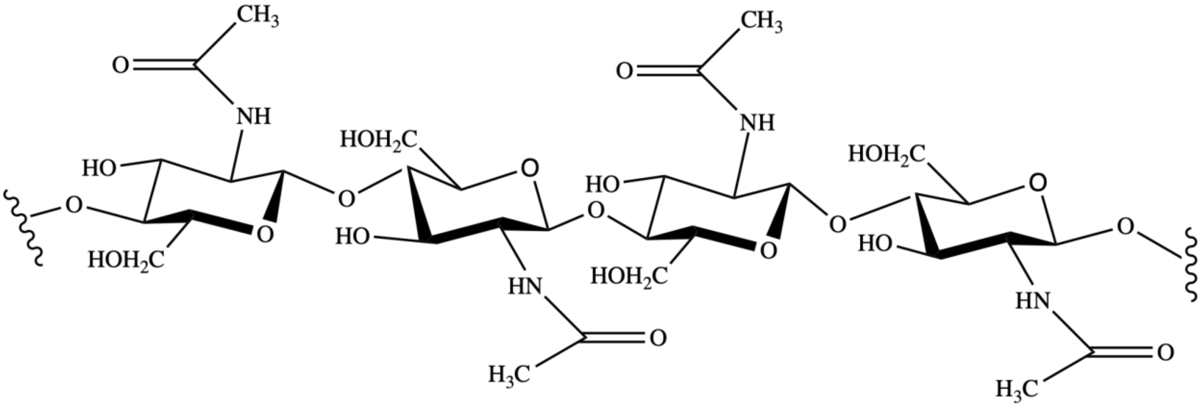

Figure 2. The unbranched chitin chain. *N-acetyl-D-glucosamine units linked by β-1,4-glycosidic bonds, where the two middle monomers are the N,N'-diacetylchitobiose unit. The figure is derived from unpublished work.*

Crystalline chitin exists as two polymorphs; α-chitin and β-chitin (Rudall & Kenchington, 1973). The two polymorphs differ in the alignment of the chitin chains, both connected by hydrogen bonding. In α-chitin, the chains are arranged anti-parallel to each other, while β-chitin chains are arranged parallelly (Gardner & Blackwell, 1975; Minke & Blackwell, 1978). α-chitin is more abundant in Nature compared with β-chitin, likely because the N-acetyl-D-glucosamine units in an anti-parallel arrangement are closer in proximity, causing a more recalcitrant and stable polysaccharide (Gardner & Blackwell, 1975).

1.2 Degradation of Biomass

Biomass can be degraded to yield fermentable sugar units as a source of renewable energy. Conversion of the biomass carbohydrates into monomeric sugar units requires a break of the glycosidic bonds connecting the monomers. Due to the crystalline structure of the carbohydrates, the glycosidic bonds are not easily accessible and the natural enzymatic degradation of polysaccharides, i.e., cellulose and chitin, is slow (Wolfenden *et al.*, 1998). However, the biomass may be exposed to pretreatment methods to separate the polysaccharide components, making them accessible for enzymatic degradation.

Pretreatment is considered the most expensive step in biomass degradation (Cheah *et al.*, 2020). The importance of preserving the different components upon separation, e.g., cellulose, lignin, and hemicellulose in lignocellulosic biomass, is therefore crucial to maximize the utilization (Tran *et al.*, 2019). Higher saccharification yields due to easier hydrolysis of the carbohydrates and minimizing costs and energy consumption are other important factors to consider when applying pretreatment technologies (Kumar *et al.*, 2016; Prasad *et al.*, 2016). Available pretreatment technologies are physical, chemical, physiochemical, or biological pretreatments, and the choice of pretreatment depends on the components of the biomass, environmental impact, and capital (Limayem & Ricke, 2012; Menon & Rao, 2012). Regardless of the pretreatment technology of choice, the overall goal is to prepare the biomass for enzymatic degradation by making the crystalline structure less rigid and thus more accessible.

In biological pretreatment, naturally occurring enzymes in fungi and bacteria disrupt the polysaccharides in the biomass. Delignification by lignin-degrading enzymes is a biological pretreatment method that can increase cellulose accessibility, but this method is not a popular pretreatment technique because the method is time-consuming. Another drawback is that the naturally occurring enzymes in fungi and bacteria may consume the polysaccharides (Cheah *et al.*, 2020).

Physical pretreatment is also termed mechanical pretreatment due to the physical interruption of the carbohydrate structure. Temperatures up to 300 °C can be applied in a physical pretreatment technique called extrusion (Maurya *et al.*, 2015). Mixing the biomass at this temperature result in shortening and removal of biomass fibers (Maurya *et al.*, 2015). Milling is another pretreatment technique that reduces the particle size and thus increases the surface area available for enzymatic hydrolysis (Baruah *et al.*, 2018). A third technique is freezing. Freezing will disrupt the cell wall structure of the biomass due to volumetric change of water in the cells and a higher glucose yield upon enzymatic degradation may be achieved (Rooni *et al.*, 2017). Both milling and freezing pretreatment techniques can be performed without generation of inhibitors, which is common upon chemical pretreatment.

Chemical pretreatment is mostly applied on lignocellulosic biomass for separation of cellulose from hemicellulose and lignin (Cheah *et al.*, 2020). Usually, hemicellulose is removed with acid pretreatment, while lignin is removed with alkali pretreatment. Sulfuric, phosphoric, nitric, or hydrochloric acid are commonly used in acid pretreatment (Cheah *et al.*, 2020). A range of temperatures may be applied depending on the acid concentration. Low temperatures are used with concentrated acids, while high temperatures may be applied when dilute acids are used (Kumar & Sharma, 2017). In alkali pretreatment technologies, hydroxide salts are commonly added to remove lignin by altering the structure (Cheah *et al.*, 2020). This type of pretreatment may also alter the structure of cellulose by swelling (Cheah *et al.*, 2020). However, inhibitors may be formed during chemical pretreatment and acid corrosion in bioreactors is a problem (Kumar & Sharma, 2017).

Physical and chemical pretreatment may be combined into physiochemical pretreatment. Physiochemical pretreatment may give higher saccharification yields; for example, when milling (physical) was combined with alkali (chemical) pretreatment for corn stover, enzymatic degradation improved by over 100 % (Kumar & Sharma, 2017). Steam explosion is another popular physiochemical pretreatment due to the low energy consumption and low costs. First, high pressure stream is applied to the biomass, before a sudden reduction in pressure cause explosive decompression of the biomass (Cheah *et al.*, 2020). Steam explosion pretreatment includes hydrolysis of hemicellulose due to *in situ* production of acids and further disruption of the biomass components (Cheah *et al.*, 2020). As the biomass is disrupted and the accessibility of polysaccharides is improved, carbohydrate active enzymes, such as glycoside hydrolases (GHs) or lytic polysaccharide monooxygenases (LPMOs), may be applied for enzymatic degradation.

1.3 Carbohydrate Active Enzymes

A group of canonical carbohydrate active hydrolases, GHs, break down polysaccharides such as cellulose, starch, or chitin (Hamre *et al.*, 2019; Igarashi *et al.*, 2011; Reilly, 2007). Cellulases, amylases, or chitinases degrade the respective polysaccharide by catalyzing the hydrolysis of the glycosidic bonds that link the monomeric units of the polysaccharide (Teeri, 1997). GHs may be processive or non-processive, and exo- or endo-acting. Processive exo-acting GHs cleave the glycosidic bonds from the chain ends without completely dissociating from the crystalline surface of the polysaccharide (Payne *et al.*, 2012). Non-processive endo-acting GHs cleave the glycosidic bonds at random, internal sites and may completely release from the polysaccharide surface, providing new sites for the processive GHs to bind (Payne *et al.*, 2012). Degradation of polysaccharides by GHs results in a β-1,4-glycosidic dimer which further can be degraded to monomeric glucose by β-glucosidases (Teeri, 1997).

Initially, it was believed that the synergistic actions between GHs were the main driving force of recalcitrant polysaccharide degradation. However, in 2010, Vaaje-Kolstad *et al.* (2010) discovered the oxidative nature of LPMOs. LPMOs are powerful redox enzymes that can access the most crystalline and densely packed parts of the polysaccharide, creating new chain ends for exo-acting GHs (Vaaje-Kolstad *et al.*, 2010). Synergistic actions between GHs and LPMOs have been shown effective upon degradation of recalcitrant polysaccharides. Hamre *et al.* (2015) reported an enhanced initial rate upon chitin degradation with the processive exo-acting chitinases, *Sm*ChiA and *Sm*ChiB, and the chitin-active *Sm*LPMO10A. *Sm*LPMO10A in synergy with a non-processive endo-acting chitinase, *Sm*ChiC, did not show an increased product yield under conditions with high substrate saturation (Hamre *et al.*, 2015). However, under different conditions it has been shown that degradation was enhanced due to synergistic activity between *Sm*ChiA and *Sm*LPMO10A (Vaaje-Kolstad *et al.*, 2010). The synergistic activity between cellulases and cellulose-active LPMOs, such as *Tr*Cel7A and *Ls*LPMO9A, enhanced degradation of cellulose (Tokin *et al.*, 2020).

1.4 Lytic Polysaccharide Monooxygenases

The unraveling of the oxidative activity of LPMOs by Vaaje-Kolstad *et al.* (2010) and the extensive LPMO research in the following years lead to a complete reclassification in the carbohydrate active enzyme (CAZy) database with the addition of the auxiliary activity (AA) family (Levasseur *et al.*, 2013). The AA family includes enzymes related to degradation of plant cell walls, such as lignin peroxidases, cellobiose dehydrogenases (CDH), and most related to this thesis; LPMOs (Levasseur *et al.*, 2013).

1.4.1 Auxiliary Activity Families of LPMOs

The primary discovery of LPMOs revealed activity towards recalcitrant chitin, and in the following year, cellulose activity of LPMOs was also demonstrated (Forsberg *et al.*, 2011; Vaaje-Kolstad *et al.*, 2010). Chitin-binding protein 21 (CBP21), today known as *Sm*LPMO10A and the first chitin-active LPMO discovered, was found to enhance enzymatic hydrolysis of crystalline chitin (Vaaje-Kolstad *et al.*, 2005a). Five years later, CBP21 was demonstrated to oxidatively cleave the glycosidic bonds of recalcitrant chitin (Vaaje-Kolstad *et al.*, 2010). Cellulose-active CelS2, also known as *Sc*LPMO10C, was demonstrated to cleave the glycosidic bonds of cellulose polysaccharides using an oxidative mechanism (Forsberg *et al.*, 2011). In the CAZy database, CBP21 and CelS2 were initially classified as carbohydrate-binding modules of family 33 (CBM33) but reclassified as AA10s once the oxidative nature of the enzyme was revealed (Levasseur *et al.*, 2013). Fungal enzymes, initially classified as GHs of family 61, exhibited oxidative cleavage of the glycosidic bonds in recalcitrant cellulose, and were classified as AA9s (Levasseur *et al.*, 2013; Phillips *et al.*, 2011).

Today, the CAZy database includes eight AA families of LPMOs; AA9, AA10, AA11, AA13, AA14, AA15, AA16, and AA17. The most extensively studied families are AA9 and AA10. Family AA9 includes fungal LPMOs, mainly active on cellulose, but hemicellulose activity has also been exhibited (Agger *et al.*, 2014; Phillips *et al.*, 2011). Family AA10 consists of bacterial LPMOs active on cellulose or chitin (Forsberg *et al.*, 2011; Vaaje-Kolstad *et al.*, 2010). In addition, some LPMOs of family AA10 have displayed activity towards both chitin and cellulose (Forsberg *et al.*, 2018). Chitin activity on soluble substrate has been reported for

LPMOs belonging to family AA11, while starch and xylan active LPMOs are found in family AA13 and AA14, respectively (Couturier *et al.*, 2018; Rieder *et al.*, 2021; Vu *et al.*, 2014). The remaining three families are not much studied, but family AA15 and AA16 consist of cellulose-active LPMOs, while the recently discovered family AA17 includes LPMOs active on pectin in plant cell walls (Filiatrault-Chastel *et al.*, 2019; Sabbadin *et al.*, 2018; Sabbadin *et al.*, 2021). LPMOs that prefer different substrates are grouped in the same AA family in the CAZy database. This is because the CAZy database group the LPMO families based on sequence identity, rather than structure similarity (Levasseur *et al.*, 2013).

1.4.2 The Structure and Active Site of LPMOs

Many LPMO crystal structures, especially from the well-studied families AA9 and AA10, have been solved. The first LPMO crystal structure that was solved from family AA10 was for CBP21, even before the oxidative nature of the enzyme was discovered (Vaaje-Kolstad *et al.*, 2005b). Similarly, the structure of an LPMO from family AA9, *Hj*LPMO9B, was solved prior to understanding the function of the enzyme (Karkehabadi *et al.*, 2008). All LPMOs have a triangular shape, with a flat side particularly suited for binding crystalline polysaccharides and hence called the substrate binding surface. The residues of the substrate binding surface may vary between LPMO families. In AA9-type LPMOs, the substrate binding surface includes two or three aromatic residues, such as tyrosine, where the aromatic rings are parallel to the crystalline surface of the polysaccharide (Li *et al.*, 2012; Wu *et al.*, 2013). AA10-type LPMOs only contain one aromatic residue parallel to the polysaccharide surface, but the substrate binding surface includes several polar residues not found in LPMOs from family AA9 (Vaaje-Kolstad *et al.*, 2005b). Vaaje-Kolstad *et al.* (2005b) showed that a mutation to the aromatic residue in the substrate binding surface of CBP21 reduced the affinity towards chitin. Further, it was discovered that the polar residues on the surface of CBP21 were involved in substrate binding (Aachmann *et al.*, 2012).

The substrate binding surface of LPMOs includes the catalytic center, and the residues involved in substrate binding situate the active site in close proximity to the glycosidic bonds (Aachmann *et al.*, 2012). LPMOs are metalloenzymes since a copper atom, crucial for the activity of the enzyme, is located at the active site (Quinlan *et al.*, 2011). The copper binds to the active site through a type II copper site, where a strictly conserved histidine residue at the N-terminus of the enzyme is involved (Quinlan *et al.*, 2011). Another conserved histidine residue also holds the copper atom in place and the coordination of the copper atom is therefore termed the *histidine brace* (Figure 3) (Chylenski *et al.*, 2019). Several other residues in the catalytic center are also of interest, as some combinations of residues are conserved (Section 1.5).

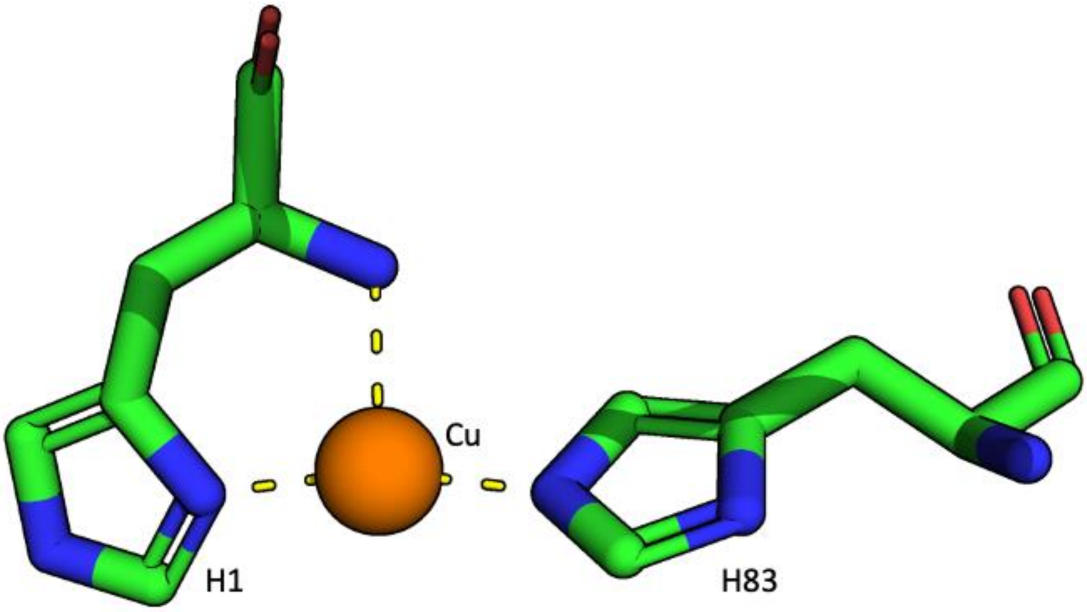

Figure 3. The histidine brace. *The histidine brace in NcLPMO9C where the copper (orange) is coordinated by the histidine residues at position 1 and 83. The figure is derived from unpublished work and prepared in PyMol (NcLPMO9C PDB: 4D7U).*

The active site of LPMOs is located close to the glycosidic bonds when the LPMO binds to the recalcitrant polysaccharide (Aachmann *et al.*, 2012). Upon oxidative cleavage of the glycosidic bonds between the monomeric units in the polysaccharide, the new oxidized chain ends will serve as binding sites for GHs that further degrade the polysaccharide. The oxidation of a glycosidic bond takes place either at the C1- or C4-position of the monomeric unit of the polysaccharide, deciding the regioselectivity of the LPMO (Beeson *et al.*, 2012; Vaaje-Kolstad *et al.*, 2010). Some LPMOs have also been reported to form both C1- and C4-oxidized chain ends upon cleavage of glycosidic bonds (Forsberg *et al.*, 2014; Phillips *et al.*, 2011; Quinlan *et al.*, 2011). The regioselectivity depends on the substrate specificity of the LPMO that is related to the residues at the substrate binding surface (Danneels *et al.*, 2019). C1-oxidation of chitin or cellulose substrates results in lactone as the primary oxidized product where the hydrated form is aldonic acid (Figure 4) (Phillips *et al.*, 2011; Vaaje-Kolstad *et al.*, 2010). C4-oxidation has only been observed for cellulose-active LPMOs where the primary oxidized product, 4-ketoaldose, is in equilibrium with the hydrated form, 4-gemdiol-aldose (Figure 4) (Beeson *et al.*, 2012; Phillips *et al.*, 2011).

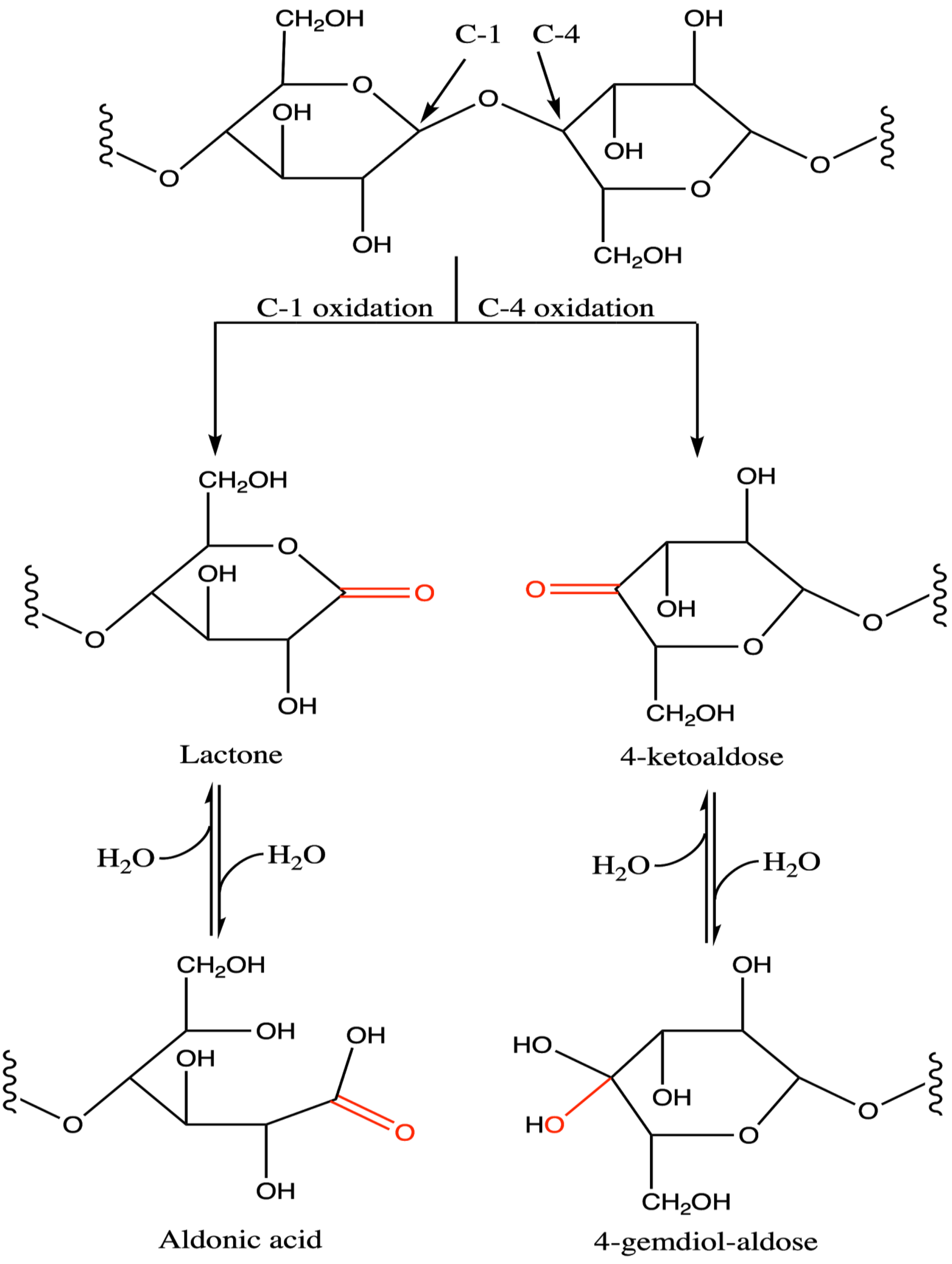

Figure 4. C1- and C4-oxidation of cellulose. *Oxidative cleavage of cellulose in the C1-position of the glucose monomer result in a lactone in equilibrium with aldonic acid. C4-oxidation of cellulose result in the primary oxidized product, 4-ketoaldose, in equilibrium with the hydrated form, 4-gemdiol-aldose. The figure is derived from unpublished work.*

1.4.3 Proposed Catalytic Mechanism of LPMOs

Vaaje-Kolstad *et al.* (2010) established the oxidative nature of LPMOs with isotope-labelling of molecular oxygen and water. Chitin-active CBP21 facilitates C1-oxidation of the glycosidic bonds and generates aldonic acid as an end-product (Vaaje-Kolstad *et al.*, 2010). The mass of aldonic acid increased with 2 Da when the reaction was performed with isotope-labelled molecular oxygen and water. These results suggested a catalytic mechanism that included both oxidation and hydrolysis. Another reaction performed under anaerobic conditions yielded no product, which strengthened the theory of LPMOs oxidative nature (Vaaje-Kolstad *et al.*, 2010). Cellulose-active LPMOs were also found to yield aldonic acid as an end-product, as well as 4-ketoaldose, with similar experimental conditions (Beeson *et al.*, 2012; Forsberg *et al.*, 2011). The oxidative nature of LPMOs were considered established and following studies on the catalytic mechanism involved the oxidative reaction intermediates and the nature of the co-substrate.

A reaction mechanism using hydrogen peroxide as a co-substrate was suggested by Wang *et al.* (2018) after Bissaro *et al.* (2017) demonstrated that the true co-substrate of LPMOs likely was hydrogen peroxide. Wang *et al.* (2018) used molecular simulations, quantum mechanical/molecular mechanical calculations, and density functional theory calculations to assess the pathway from which LPMO-Cu(II) is reduced to the oxidative cleavage of the glycosidic bond (Figure 5A). The suggested mechanism was tested using a C1- and C4-oxidizing LPMO, *Ls*LPMO9A (Wang *et al.*, 2018). Reduction of the LPMO in the LPMO-Cu(II) resting state results in the active LPMO-Cu(I) state. Hydrogen peroxide interacts with the LPMO through hydrogen bonding with second sphere residues in the catalytic center. An electron transfer from the LPMO-Cu(I) complex was proposed to break the O-O bond in hydrogen peroxide, leading to formation of an hydroxyl radical ($^{\bullet}$OH) and LPMO-Cu(II)-OH (Wang *et al.*, 2018). The $^{\bullet}$OH radical was preferably stabilized through hydrogen bonding with the LPMO through amino acid residues close to the active site and the substrate. Further, hydrogen atom abstraction from LPMO-Cu(II)-OH by the hydroxyl radical was favored as the calculated transition energy was low (Wang *et al.*, 2018). This hydrogen atom abstraction would result in formation of an LPMO-Cu(II)-oxyl species and water. At this point in the catalytic mechanism, LPMO-Cu(II)-O$^{\bullet}$ was located close to the C4-hydrogen of the glucose monomer. The LPMO-Cu(II)-oxyl species was likely to perform a hydrogen atom abstraction at this position due to the calculated low transition energy, resulting in a glycosidic bond cleavage (Wang *et al.*, 2018).

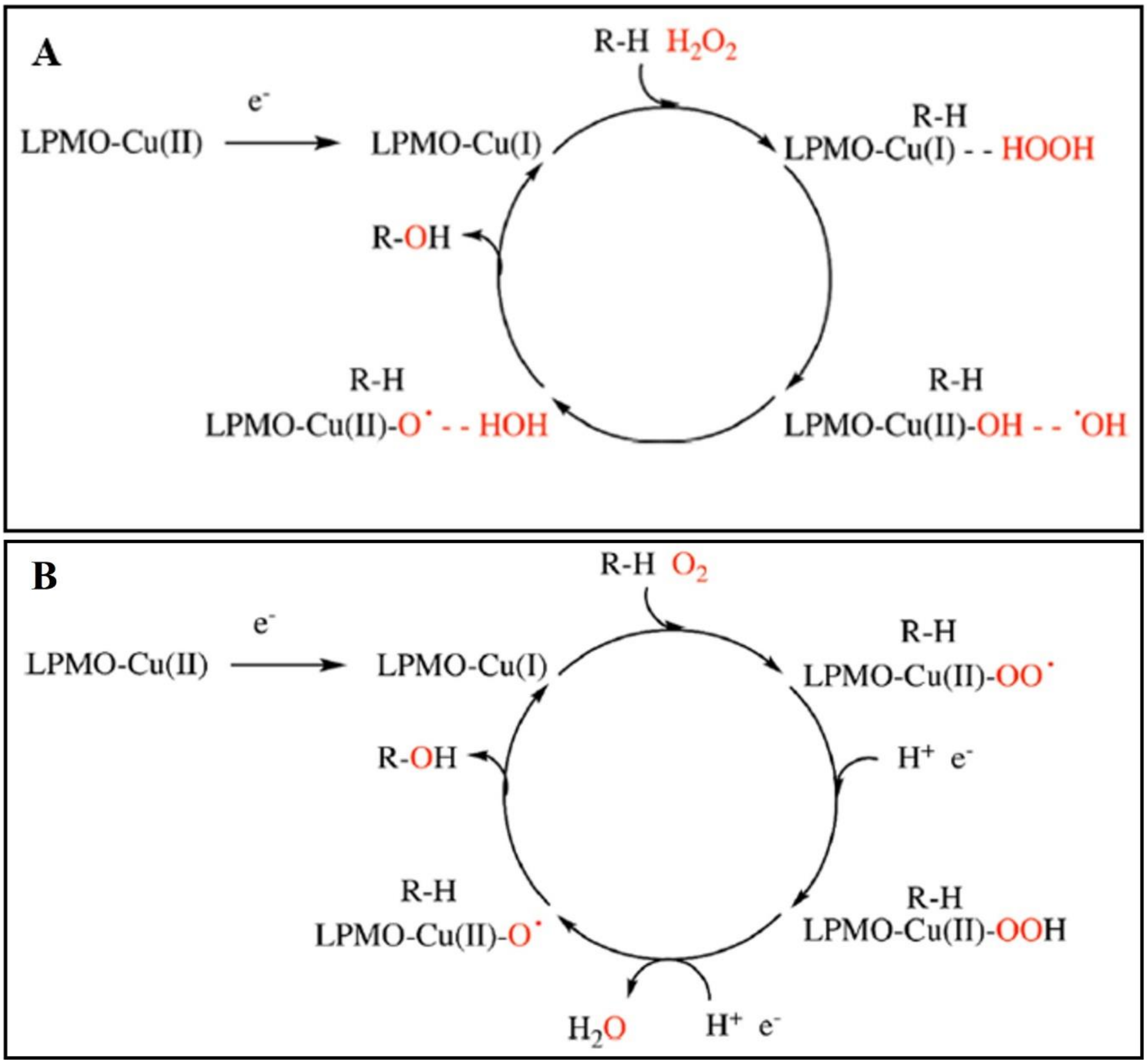

Figure 5. Two proposed catalytic mechanisms for glycosidic bond cleavage by the LPMO with different co-substrates. *(A) Catalytic mechanism using hydrogen peroxide as a co-substrate suggested by Wang et al. (2018). (B) Catalytic mechanism using oxygen as a co-substrate suggested by Bertini et al. (2018). The figure is derived from Chylenski et al. (2019).*

A reaction mechanism using molecular oxygen as a co-substrate has also been proposed (Figure 5B). Bertini *et al.* (2018) used density functional theory calculations, and suggested that an LPMO-Cu(II)-OO$^\bullet$ radical could form upon binding of molecular oxygen to LPMO-Cu(I). Calculations further favored proton coupled electron transfer that formed the LPMO-Cu(II)-OOH complex. A second proton coupled electron transfer would generate the LPMO-Cu(II)-oxyl species, also suggested in the mechanism proposed by Wang *et al.* (2018). An oxygen rebound mechanism would result in a glycosidic bond break and regeneration of LPMO-Cu(I) (Bertini *et al.*, 2018; Kim *et al.*, 2014). However, there is an ongoing debate about whether hydrogen peroxide or molecular oxygen is the true co-substrate of LPMOs.

1.4.4 The Co-Substrate and Reductant of LPMOs

LPMOs act as electron acceptors upon initiation of LPMO catalysis. A reductant will donate an electron to the LPMO-Cu(II) complex and the copper at the active site will be reduced to Cu(I). Ascorbic acid, gallic acid, and cysteine are chemical compounds commonly used as reductants in LPMO reactions (Quinlan *et al.*, 2011; Stepnov *et al.*, 2022a; Vaaje-Kolstad *et al.*, 2010). Ascorbic acid, which is the most commonly used reductant among the aforementioned reducing agents, has recently been shown to be highly sensitive to free copper with respect to *in situ* production of hydrogen peroxide (Stepnov *et al.*, 2021). In contrast, sensitivity towards free copper was close to none when gallic acid was used as a reductant (Stepnov *et al.*, 2021). Variation in LPMO activity have also been observed when using either ascorbic acid, gallic acid, or cysteine as the reductant (Stepnov *et al.*, 2022a). This may be due to various copper sensitivity, but is more likely related to *in situ* hydrogen peroxide production (Stepnov *et al.*, 2021; Stepnov *et al.*, 2022a). Hydrogen peroxide may also be generated in side-reactions involving molecular oxygen and ascorbic acid under aerobic LPMO reaction conditions (Bissaro *et al.*, 2017). Other reductants may also be used to initiate LPMO reactions. An oxidoreductase secreted by fungi, cellobiose dehydrogenase (CDH), can act as a natural reductant for fungal LPMOs (Loose *et al.*, 2016; Phillips *et al.*, 2011). Lignin have also been shown to function as a natural reductant to LPMOs (Müller *et al.*, 2018). However, lignin is involved in redox reactions not related to the LPMO reaction, which makes the reduction of Cu(II) to Cu(I) difficult to control (Müller *et al.*, 2018). However, the need for an externally delivered electron to initiate catalysis is highly acknowledged regardless of co-substrate.

The co-substrates suggested for LPMOs are molecular oxygen and hydrogen peroxide. In monooxygenase reactions, an additional electron must be delivered by the reductant in order for the LPMO to cleave the glycosidic bond (Figure 5B). In contrast, an additional electron donation is not required for glycosidic bond cleavage in a peroxygenase reaction (Bissaro *et al.*, 2017; Kuusk *et al.*, 2018). In theory, only one electron is needed to initiate continuous cleavage of glycosidic bonds when hydrogen peroxide is used as a co-substrate in LPMO mediated catalysis (Figure 5A). Bissaro *et al.* (2017) showed that in a reaction where hydrogen peroxide was externally supplemented, the final oxidized product concentration (45 µM) was higher than the concentration of reductant added (10 µM). This supports the concept that the LPMO-Cu(II) complex only must be reduced once when hydrogen peroxide is used as a co-substrate. However, electrons are consumed in the peroxygenase reaction, e.g., if the hydroxyl radicals formed are not contained by the protein, they will "leak" into solution and interact with the reductant or other components in the reaction (Kuusk *et al.*, 2018). Hydroxyl radicals in solution may also interact with residues near the catalytic center and thus inactivate the LPMO (Section 1.4.5). Donation of additional electrons is therefore necessary in peroxygenase reactions, and crucial in monooxygenase reactions.

The debate about the true co-substrate of LPMOs began with compelling research provided by Bissaro *et al.* (2017). An LPMO reaction with isotope-labelled hydrogen peroxide and a high surplus of molecular oxygen showed that the oxygen that was present in the oxidized product originated from hydrogen peroxide and not oxygen (Bissaro *et al.*, 2017). Additionally, externally added hydrogen peroxide increased the product formation rate tremendously compared with monooxygenase reactions. External addition of hydrogen peroxide yielded a 17.8-fold increase the catalytic rates from 0.7 min^{-1} to 13 min^{-1} (Bissaro *et al.*, 2017). An even higher increase in catalytic rates upon addition of hydrogen peroxide to an LPMO reaction were observed by Kuusk *et al.* (2018).

In situ hydrogen peroxide generation by LPMOs were initially suggested to only occur in the absence of substrate (Kittl *et al.*, 2012). However, as hydrogen peroxide is likely the preferable co-substrate of LPMOs, the rate and product yield under standard aerobic reaction conditions are determined by the LPMOs ability to generate hydrogen peroxide *in situ* or by hydrogen peroxide generation in side-reactions with molecular oxygen and a reductant (e.g., ascorbic acid) (Bissaro *et al.*, 2017; Stepnov *et al.*, 2021). Hydrogen peroxide is also the limiting factor in LPMO reactions with externally added hydrogen peroxide (Bissaro *et al.*, 2017; Müller *et al.*, 2018). This was shown by Müller *et al.* (2018) as an LPMO reaction was not reinitiated by supplementing ascorbic acid, but by addition of hydrogen peroxide. However, the supply of hydrogen peroxide must be controlled, as high concentrations of hydrogen peroxide may damage the catalytic center and inactivate the LPMO (Bissaro *et al.*, 2017; Müller *et al.*, 2018)

1.4.5 LPMO Inactivation

LPMO inactivation occur due to excess amounts of hydrogen peroxide in the reaction. Accumulation of hydrogen peroxide occurs upon depletion of substrate or reductant because then the LPMOs will not be able to effectively consume the hydrogen peroxide (Bissaro *et al.*, 2017). Upon depletion of substrate binding sites, hydrogen peroxide will accumulate in solution, as will non-bound reduced LPMOs (Bissaro *et al.*, 2017; Müller *et al.*, 2018). The non-bound reduced LPMOs are then prone to oxidative self-inactivation as excess hydrogen peroxide will react with the non-bound LPMOs and generate reactive oxygen species (Bissaro *et al.*, 2017; Müller *et al.*, 2018). Supplementing high concentrations of hydrogen peroxide in reactions where substrate binding sites are still available will also cause LPMO inactivation (Bissaro *et al.*, 2017; Müller *et al.*, 2018). The excess hydrogen peroxide can engage in side-reaction with the reductant (or other compounds in the reaction) and generate reactive oxygen species (Bissaro *et al.*, 2017; Müller *et al.*, 2018). The reactive oxygen species will react with crucial residues in the catalytic center of LPMOs and thus cease catalysis (Bissaro *et al.*, 2017).

1.5 Second Sphere Residues of LPMOs

The second sphere residues of LPMOs are the residues in the catalytic center beyond the *histidine brace*. These residues have been studied to a lesser extent than residues involved in substrate binding. However, Banerjee *et al.* (2022) recently devoted a study to the protonation state of a second sphere histidine residue structurally conserved throughout the AA9 family. In this study, they showed that this histidine residue (e.g., H147 in *Ls*LPMO9A or H164 in *Ta*LPMO9A) was generally not protonated at pH 6, and therefore did not act as a proton donor during LPMO catalysis. A computational study by Wang *et al.* (2018) on the catalytic mechanism of LPMOs with hydrogen peroxide as co-substrate also investigated the role of the second sphere residues of *Ls*LPMO9A. Hydrogen peroxide was suggested to be stabilized by the conserved histidine at position 147, the glutamate at position 148, and the glutamine at position 162, in addition to by one of the histidine residues in the *histidine brace* (Wang *et al.*, 2018). The structurally conserved histidine (H147) in the AA9 family and the second sphere glutamine at position 162 was also proposed to stabilize the hydroxyl radical generated in the peroxygenase reaction (Figure 5A) (Wang *et al.*, 2018). In another recent study, Bissaro *et al.* (2020) investigated a second sphere glutamate residue (E60) in *Sm*LPMO10A, equivalent to the glutamine residue (Q162) in *Ls*LPMO9A. The second sphere glutamate residue was mutated to either a glutamine, asparagine, serine, or aspartate residue. All four mutants displayed a lower initial rate of product generation and an overall lower substrate concentration after 24 hours. This suggests that the second sphere glutamate residue is important for peroxygenase activity in *Sm*LPMO10A (Bissaro *et al.*, 2020).

Different LPMOs contain structurally conserved motifs of second sphere residues. Insight into these motifs was previously identified by Kelsi Hall (K. Hall, pers.com., 2022) A multiple sequence alignment of all LPMO sequences in the CAZy database, generated by Ivan Ayuso-Fernandez (I. Ayuso-Fernandes, pers. com., 2022), was used to determine the prevalence of these motifs. In the AA9 family of LPMOs, a YQH motif is most common (84 %) among the aligned sequences. This motif is also evident in some LPMOs of family AA10 (6 %). Second sphere motifs in the AA10 family vary substantially compared to the AA9 family. The most prevalent motif in the AA10 family is the FEN motif (49 %), while the second most conserved motif is the FER motif (31 %) (Figure 6). The multiple sequence alignment also showed that there is a close correlation between the residues of the FER motif, as if a second sphere arginine residue is present, the two other residues in the motif are always a glutamate and a phenylalanine. The residues of the YQH motif are also closely related in the AA10 family as the only other motif observed with a second sphere glutamine and histidine residue was an FQH motif. The FQH motif have also been observed in the AA9 family, along with FEH and YEH second sphere motifs.

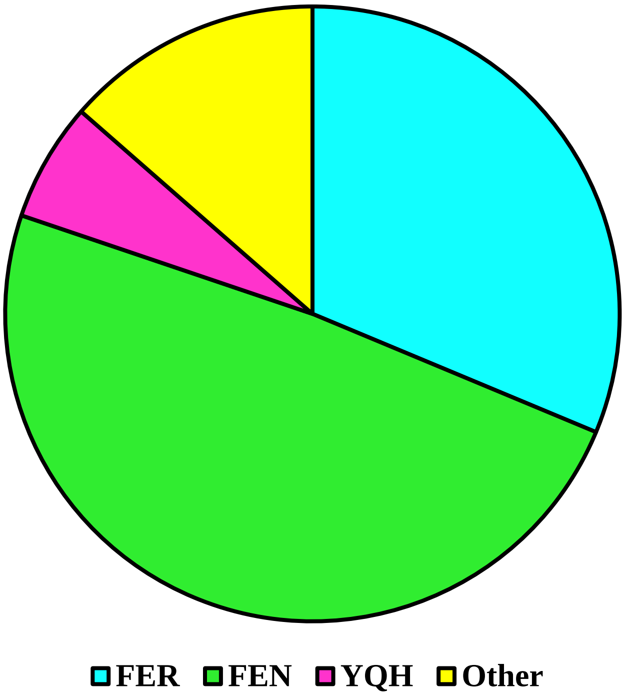

Figure 6. Second sphere residue motifs in the AA10 family. *The structurally conserved FER (blue), FEN (green), and YQH (pink) second sphere motifs in the AA10 family (identified by Kelsi Hall). A multiple sequence alignment was generated by Ivan Ayuso-Fernandez from all LPMO sequences available in the CAZy database. This pie chart was generated from 3826 LPMO sequences from the AA10 family.*

1.6 The Second Sphere Residues of *Ma*LPMO10B and Research Aim

*Ma*LPMO10B, the LPMO of interest in this thesis, is a bacterial LPMO from *Micromonospora aurantiaca* classified in the AA10 family (Forsberg *et al.*, 2018). The LPMO consist of a catalytic domain, a linker region, and a carbohydrate-binding module (CBM) (amino acid sequence in Table A 1). *Ma*LPMO10B is active on insoluble cellulose and chitin, and C1- and C4-oxidized cello-oligosaccharides are generated upon glycosidic bond cleavage of cellulose (Forsberg *et al.*, 2018). The second sphere motif of *Ma*LPMO10B wild type (WT) is YQH and was previously identified by Kelsi Hall (K. Hall, pers. com., 2022).

In this thesis, we aimed to investigate the function and interplay of three second sphere residues in *Ma*LPMO10B. Mutagenesis was performed to obtain mutants where either one, two, or three of the second sphere residues in the YQH motif were altered. The residues introduced were from the FER motif that naturally occurs in cellulose-active LPMOs such as mgLPMO10 and *Sc*LPMO10C. This catalytic triad is one of the most common motifs in the AA10 family and was therefore of interest. Due to the large number of mutants produced in this study, all mutants were assigned an amino acid code indicating the new second sphere motif generated (Figure 7). The amino acid sequence of *Ma*LPMO10B WT and the mutants are shown in Table A 1.

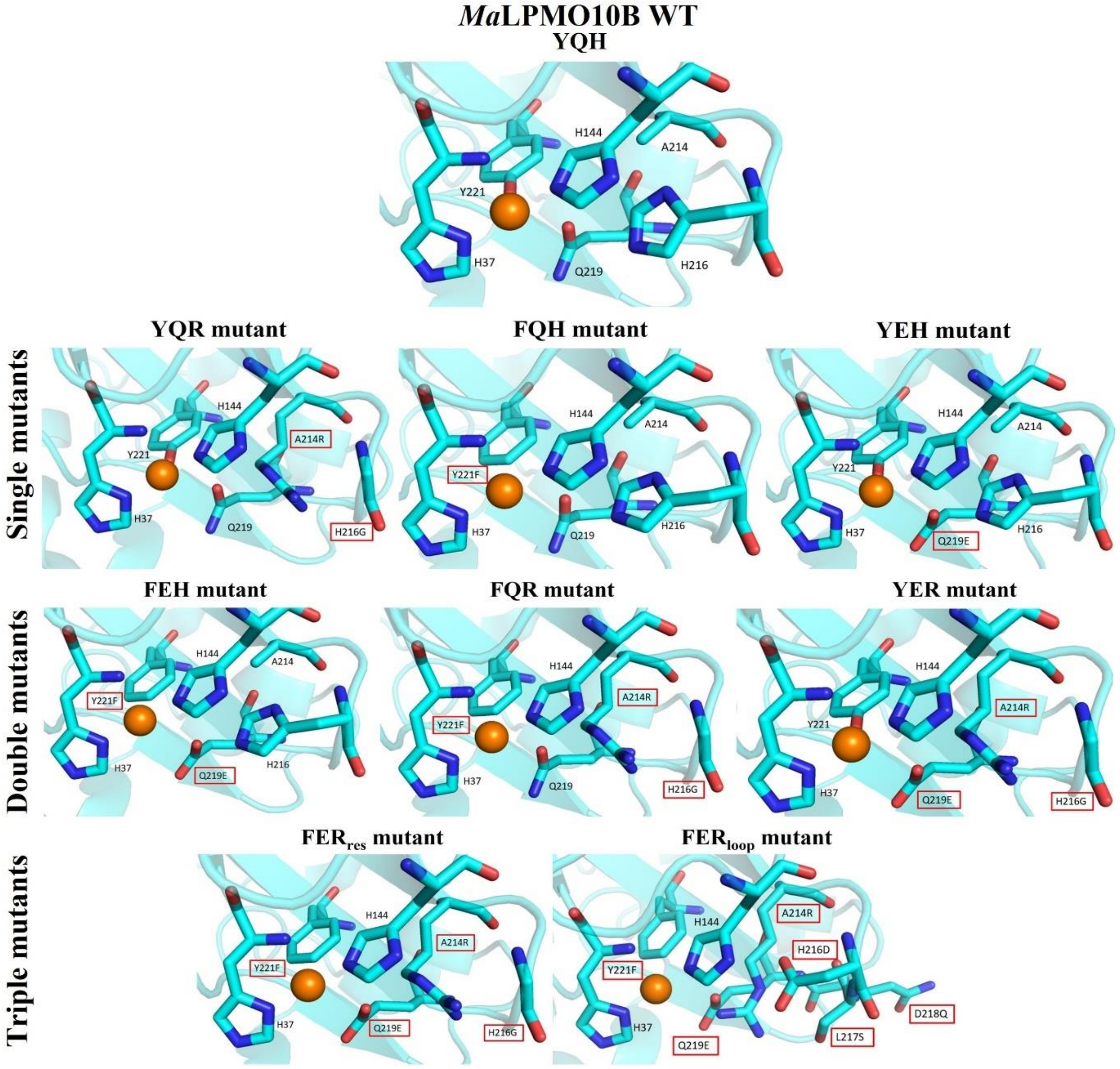

*Figure 7. **The catalytic center of MaLPMO10B WT and the mutants.** MaLPMO10B WT and the mutants with amino acid codes where a red square indicate a mutation. The catalytic center contains a copper atom (orange) coordinated by the histidine brace (H37 and H144) and the second sphere residues of interest in this study. The mutant structures are not solved crystal structures but were generated in PyMol using the mutagenesis wizard and the most likely conformation of the mutated residues. (MaLPMO10B PDB: 5OPF)*

The YQR mutant is here termed a single mutant, although two mutations have been introduced (Figure 7). This is because the histidine at position 216 must be mutated to a glycine (or another small residue) in order to fit the alanine to arginine mutation at position 214 (Figure 7). Therefore, two mutations were required to investigate this position. The same reasoning applies for all mutants with an alanine to arginine mutation at position 214. The triple mutants, FER$_{loop}$ (loop exchange) and FER$_{res}$ (residue exchange), have the exact same second sphere motif. However, the FER$_{res}$ mutant has a glycine instead for an aspartate residue at position 216 due to the previously discussed space issues. For this reason, a second mutant, FER$_{loop}$, was created which had the entire loop region exchanged into the loop region of mgLPMO10, allowing space for an aspartate residue (Figure 8). The loop that contains some of the second sphere residues in mgLPMO10 is larger than the loop in *Ma*LPMO10B, allowing the aspartate residue that is present in both mgLPMO10 and *Sc*LPMO10C to be introduced. This aspartate residue is not present in all LPMOs with an FER motif, however it may be important for activity and a mutant containing this residue was therefore generated.

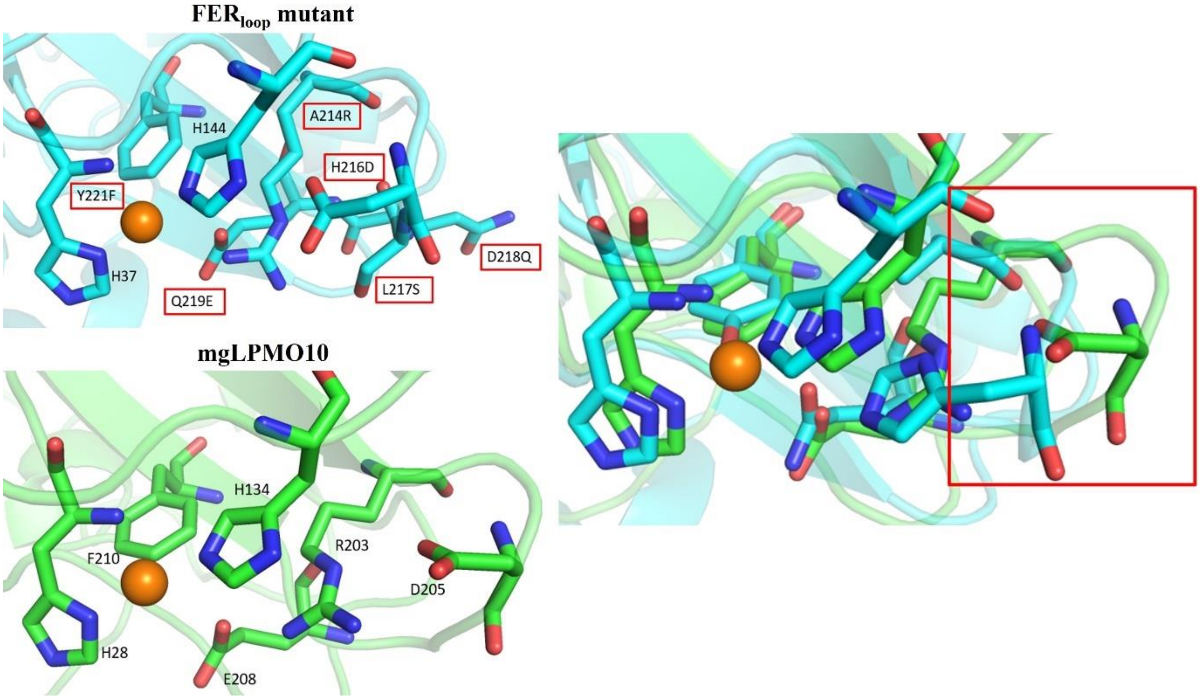

FER$_{loop}$ mutant

mgLPMO10

Figure 8. The catalytic center of FER$_{loop}$ mutant and mgLPMO10B. *The catalytic center contains a copper atom (orange) coordinated in a histidine brace (H37 and H144 for the FER$_{loop}$ mutant, H28 and H134 for mgLPMO10). The MaLPMO10B WT (blue) crystal structure has been structurally aligned with mgLPMO10 (green) to show the difference in loop size. The large red square outlines the loops. The structure of the FER$_{loop}$ mutant have not been solved from a crystal structure but generated in PyMol using the mutagenesis wizard and choosing the most likely conformation of each residue. (The crystal structure of mgLPMO10 was solved by Ole Golten, unpublished)*

The scope was broadened after performing enzyme characterization assays on *Ma*LPMO10B WT and the mutants, where the YEH mutant appeared to have interesting properties. Therefore, the second aim of this thesis was to analyze the effect pH and type of reductant had on *Ma*LPMO10B WT and the YEH mutant.

2 Materials

2.1 Laboratory Equipment

Table 1. The laboratory equipment used in this thesis, including specifications and supplier.

Category	Equipment	Specifications	Supplier
Centrifuges	4530 R centrifuge		Eppendorf
	MiniSpin centrifuge		Eppendorf
	Sorvall LYNX 6000 centrifuge	F21-8 x 50y rotor F9-6 x 1000 LEX rotor	ThermoFisher Scientific
Columns	Dionex CarboPac^{TM} PA200 1 x 250 mm analytical column and 1 x 50 mm guard column		ThermoFisher Scientific
	HiLoad® 16/600 Superdex® 75 pg 120 mL column		Cytiva
	HiTrap^{TM} DEAE Sepharose FF 5 mL column		Cytiva
	Rezex RFQ-Fast Acid H^+ (8 %) 7.8 x 100 mm column		Phenomenex
Instruments	ÄktaPure		Cytiva
	ÄktaPurifier		Cytiva
	Dionex ICS-6000		ThermoFisher Scientific
	Dionex UltiMate 3000		ThermoFisher Scientific
	GelDoc Go Imaging system	UV/Stain Free Tray Blue Tray	BioRad

	Multiscan FC plate reader		ThermoFisher Scientific
	NanoDrop^{TM} One/One^{C} Microvolume UV/Vis spectrophotometer		ThermoFisher Scientific
	NanoPhotometer® C4 spectrophotometer		Implen
	T100^{TM} Thermal Cycler		BioRad
Other equipment	96-Well Microtiter^{TM} microplate		ThermoFisher Scientific
	Aeration system with sparger lids		Made in-house
	Amicon® Ultra-15 centrifugal filter units	10 000 Da MWCO	Merck
	AV-100 laminar air flow cabinet		Telstar
	Balancers		VWR
	Blue-cap bottles and lids		VWR
	Centrifugal bottles	1 L and 30 mL	ThermoFisher Scientific
	Cryotubes		Sarstedt
	Eppendorf tubes	2 mL 1.5 mL	VWR
	Falcon tubes	15 and 50 mL	Greiner Bio-One
	Glass equipment	Beakers Volumetric flasks Measuring cylinders Bottles with rubber stopper lids	VWR
	Heating cabinet	37 °C	Termaks

	HPLC vials and lids		VWR
	Julabo 5A water bath	42 °C	Julabo
	Magnetic stirrer		ThermoFisher Scientific
	Mini-PROTEAN® tetra cell		BioRad
	Mini-PROTEAN® TGX stain-free precast gel		BioRad
	Multichannel pipette		VWR
	MultiScreen® HTS 96-well filter plates		Merck
	MultiScreen® HTS vacuum manifold		Merck
	Multitron Standard shaking incubator		Infors HT
	pH meter	pH110M	VWR
	Pipette tips	Next Generation Tip Refill	VWR
	PowerPac^{TM} basic power supply		BioRad
	Schlenk system for nitrogen flushing		Made in-house
	Single channel pipettes		ThermoFisher Scientific
	Steritop filter	0.45 µm	Merck
	Syringe	20, 30, and 60 mL	Merck
	Syringe filter	0.45 µm	Sarstedt
	Thermomixer C		Eppendorf
	Vortex	MS2 Minishaker	IKA
	Whitley A95 TG anaerobic workstation		Don Whitley Scientific

2.2 Software for Analysis

Table 2. The software used during analysis of various enzymatic applications and the supplier of each software.

Software	Application	Supplier
Chromeleon 7.0	HPAEC-PAD UHPLC	Chromeleon
ProtParam	Determine physiochemical properties of enzymes	Expasy
SkanIt RE 6.1.1	Amplex red assay Breslmayr assay	ThermoFisher Scientific
SnapGene	Aligning gene sequences	SnapGene
Translate tool	Translate a nucleotide sequence to an amino acid sequence	Expasy
Unicorn 5.2	Size exclusion chromatography	Cytiva
Unicorn 6.4	Anion exchange chromatography	Cytiva

2.3 Chemicals

Table 3. The chemicals used during this thesis and the supplier for each chemical.

Chemical	Supplier
2,6-dimethoxyphenol (2,6-DMP)	Merck
Agar	Merck
Ampicillin	Merck
Amplex red	ThermoFisher Scientific
Antifoam 204	Merck
Ascorbic acid	Merck
Benchmark^{TM} protein ladder	ThermoFisher Scientific
Bis-Tris propane	Merck
Copper(II) sulphate	VWR
Cysteine	Merck

Dipotassium hydrogen phosphate	Merck
DpnI restriction enzyme	New England BioLabs
Ethanol	VWR
Ethylenediaminetetraacetic acid (EDTA)	Merck
Gallic acid	Merck
Gel Loading Dye, Purple (6 x)	New England BioLabs
GeneRuler 1 kB DNA ladder	ThermoFisher Scientific
Glycerol	Merck
Horseradish Peroxidase (HRP)	Merck
Hydrochloric acid	Merck
Hydrogen peroxide	Merck
Magnesium chloride	Merck
N,N,N’,N’-tetramethyl-1,4-phenylenediamine (TMP)$_{red}$	Merck
NEBuilder HiFi DNA Assembly master mix	New England BioLabs
NuPage® LDS Sample buffer (4 x)	ThermoFisher Scientific
NuPage® Sample reducing agent (10 x)	ThermoFisher Scientific
One Shot® BL21 Star^{TM} (DE3) chemically competent *E. coli* cells	ThermoFisher Scientific
One Shot® TOP10 chemically competent *E. coli* cells	ThermoFisher Scientific
Phenylmethylsulphonyl fluoride (PMSF)	Merck
Phosphoric acid swollen cellulose (PASC)	Made in-house
piperazine-N,N’-bis(2-ethanesufonic acid) (PIPES)	Merck
Potassium dihydrogen phosphate	Merck
Potassium hydroxide	ThermoFisher Scientific
Potassium methanesulfonate (KMSA)	ThermoFisher Scientific
Q5® High-Fidelity 2 x master mix	New England BioLabs
RedTaq DNA Polymerase 2 x master mix	VWR
Sodium acetate	VWR
Sodium chloride	VWR
Sodium phosphate dibasic	Merck

Sodium phosphate monobasic	Merck
Sucrose	Merck
Sulfuric acid	Merck
Super optimal broth (SOC) media	ThermoFisher Scientific
SYBR^{TM} Safe DNA Gel Stain	ThermoFisher Scientific
TraceSELECT® water	Honeywell
Tris	ThermoFisher Scientific
Tris Acetate-EDTA buffer (10 x)	BioRad
Tris/Glycine/SDS buffer (1 x)	BioRad
Tryptone	ThermoFisher Scientific
Ultrapure Agarose^{TM}	ThermoFisher Scientific
Yeast extract	ThermoFisher Scientific
β-chitin extracted from squid pen	Glentham Life Sciences Batch: 20140101

2.4 Media and Buffers

Table 4. The content and description of how each media and buffer was created during this thesis.

Media or buffer	**Content**
Bis-Tris propane pH 9.5 Bis-Tris propane pH 9.5, 1 M NaCl	A 500 mM Bis-Tris propane stock solution was made. Bis-Tris propane was dissolved in ddH$_2$O and adjusted to pH 9.5 with HCl. After pH-adjustment, ddH$_2$O was added to the final volume. The solution was filtered through a 0.45 µm filter. 25 mM Bis-Tris propane pH 9.5 was made from the 500 mM stock solution. NaCl was added to a final concentration of 1 M and the 500 mM stock solution was diluted to create 25 mM Bis-Tris propane pH 9.5, 1 M NaCl. The buffer was filtered through a 0.45 µm filter.
Lysogeny broth (LB) agar	10 g tryptone 10 g NaCl

	Materials
	5 g yeast extract 15 g of agar All the dry ingredients were weighed out and dissolved in ddH_2O up to 1 L. The agar was then autoclaved at 121 °C for 15 minutes.
LB media	10 g tryptone 10 g NaCl 5 g yeast extract All the dry ingredients were weighed out and dissolved in ddH_2O up to 1 L. The media was then autoclaved at 121 °C for 15 minutes.
PIPES buffer pH 6	PIPES was dissolved in ddH_2O to a final concentration of 200 mM and filtered through a 0.45 µm filter. The stock solution was diluted to 20 mM upon use.
Sodium phosphate buffer pH 6 or pH 8	A 1 M stock solution of NaH_2PO_4 and a 1 M stock solution of Na_2HPO_4 was made. Na_2HPO_4 was heated slightly upon dissolving the powder. Both solutions were filtered through a 0.45 µm filter. The sodium phosphate buffer was pH adjusted by adding 1 M Na_2HPO_4 to 1 M NaH_2PO_4 until pH 6 or pH 8 was reached. The 1 M stock solution of sodium phosphate buffer was further diluted upon use.
Spheroplast buffer	100 mM sucrose 100 mM Tris-HCl pH 8 0.5 mM EDTA pH 8 Sucrose was weighed out and dissolved in ddH_2O. 10 mL of 1 M Tris-HCl pH 8 and 100 µL of 0.5 M EDTA pH 8 was added to the dissolved sucrose.

	ddH_2O was added up to 100 mL. The spheroplast buffer was stored at 4 °C.
Terrific broth (TB) media	24 g yeast extract 20 g tryptone 4 mL glycerol 100 mL 0.17 M KH_2PO_4 0.72 M K_2HPO_4 Yeast extract and tryptone was weighed out and ddH_2O was added to dissolve the powder. Concentrated glycerol was added and dissolved. ddH_2O was added to 900 mL and the bottle was autoclaved at 121 °C for 15 minutes. After autoclaving, 100 mL of autoclaved 0.17 KH_2PO_4 0.72 M K_2HPO_4 was added to the media in a sterile cabinet.
Tris-HCl pH 7.5, 200 mM NaCl	A 1 M Tris-HCl pH 7.5 stock solution was made by dissolving Tris powder in ddH_2O. The solution pH-adjusted to pH 7.5 and then filtered through a 0.45 µm filter. 200 mM NaCl was dissolved in ddH_2O and the stock solution of Tris-HCl pH 7.5 was diluted to 50 mM. The solution was filtered through a 0.45 µm filter.

2.5 Kits

Table 5. The kits used in this thesis and the supplier of each kit.

Kit	**Supplier**
DNA clean and concentrator® -5	Zymo research
E.Z.N.A.® Plasmid DNA Mini Kit I	Omega Bio-Tek

2.6 Primers

Table 6. The name, DNA sequence, and application of each primer used in this thesis.

Name	**Sequence 5’-3’**	**Application**
pRSETB_insert_fwd	ACAACGGTTTCCCTCTAGAAATAATTTTGT	Verify transformation
pRSETB_insert_rev	TTATGCTAGTTATTGCTCAGCGGTGGCAGC	Verify transformation
pRSETB_amplify_fwd	TGCAGCGATGTTGACTTTGGCGGTTCTGGT	Amplify the pRSETB backbone
pRSETB_amplify_rev	GCGACGATACGGCGTTGACATATGTATATCTC	Amplify the pRSETB backbone
SignalP_fwd	AGCGAGTCAGTGAGCGAGGAAGCGGATGAGCGCCCAATACGCAAACC	Verify correct gene sequence
*Ma*LPMO10B_Y221F_fwd	CCAATCGTTTTACCTGTGCAGCGATGTTGACTTTGGCGGTTCT	Create the FQH mutant
*Ma*LPMO10B_Y221F_rev	CACAGGTAAAACGATTGGTCCAGGTGTGACGCCTGCCAGATGG	Create the FQH mutant
*Ma*LPMO10B_Q219E_fwd	CACCTGGACGAATCGTATTACCTGTGCAGCGATGTTGACTTTG	Create the YEH mutant
*Ma*LPMO10B_Q219E_rev	ATACGATTCGTCCAGGTGTGACGCCTGCCAGATGGTATACACG	Create the YEH mutant
*Ma*LPMO10B_A214R_H216G_fwd	GGCAGCGGTCAGGCCTGGACCAATCGTATTACCTGTGCAGCGA	Create the YQR mutant
*Ma*LPMO10B_A214R_H216G_rev	CCAGGCCTGACCGCTGCCAGATGGTATACACGACATGGCGGCC	Create the YQR mutant
*Ma*LPMO10B_Q219E_Y221F_fwd	TGGACGAATCGTTTTACCTGTGCAGCGATGTTGACTTTGGCGG	Create the FEH mutant

*Ma*LPMO10B_Q219E_Y221F_rev	GGTAAAACGATTCGTCCAGGTGTGACGCCTGCCAGATGGTATA	Create the FEH mutant

2.7 Gene Fragments

Table 7. The DNA sequence of the ordered gene fragments used for DNA assembly of the YER, FQR, FER$_{res}$, and FER$_{loop}$ mutants. The overhangs are shown in yellow and the codons where mutations were introduced are shown in cyan. The gene fragments were designed and ordered by Kelsi Hall.

Mutant	Sequence 5'-3'
YER	GATATACATATGTCAACGCCGTATCGTCGCCCGCTGCCGCTGGCCGCCGCAATCCTGGGTGTTTGTGCCGTCGTCGCTGCTCTGCTGACCACCGCTTTTAGCGGTCCGGCCAGCGCGCATGGCAGCGTGGTTGATCCGGCCAGCCGTTCTTATAGTTGCTGGCAGCGCTGGGGCGGTGATTTCCAAAACCCGGCAATGGCTACCCAGGACCCGATGTGTTGGCAGGCGTGGCAAGCCGATCCGAACGCAATGTGGAACTGGAATGGCCTGTTTCGTGAAGGTGTGGCGGGCAATCATCAAGGCGCCATTCCGGATGGTCAGCTGTGCTCGGGCGGTCGTACCCAGAGCGGCCGTTATAATGCACTGGATACCGTGGGTGCTTGGAAAACGGTTCCGGTCACCAACAACTTCCGTGTTAAATTTTTCGATCAAGCGAGCCACGGCGCCGACTATATTCGCGTGTACGTTACGAAACAGGGTTACAACGCACTGACCAGTCCGCTGCGTTGGTCCGACCTGGAACTGGTGGGTCAAATTGGTAATACGCCGGCCTCCCAGTGGACCCGCGAAGTTGATGGTGTCTCAATTCAGATTCCGGCCAATGCACCGGGTCGTACCGGCCGCCATGTCGTGTATACCATCTGGCAGCGCTCAGGTCTGGACGAATCGTATTACCTGTGCAGCGATGTTGACTTTGGCGGTTCTGGT
FQR	GATATACATATGTCAACGCCGTATCGTCGCCCGCTGCCGCTGGCCGCCGCAATCCTGGGTGTTTGTGCCGTCGTCGCTGCTCTGCTGACCACCGCTTTTAGCGGTCCGGCCAGCGCGCATGGCAGCGTGGTTGATCCGGCCAGCCGTTCTTATAGTTGCTGGCAGCGCTGGGGCGGTGATTTCCAAAACCCGGCAATGGCTACCCAGGACCCGATGTGTTGGCAGGCGTGGCAAGCCGATCCGAACGCAATGTGGAACTGGAATGGCCTGTTTCGTGAAGGTGTGGCGGGCAATCATCAAGGCGCCATTCCGGATGGTCAGCTGTGCTCGGGCGGTCGTACCCAGAGCGGCCGTTATAATGCACTGGATACCGTGGGTGCTTGGAAAACGGTTCCGGTCACCAACAACTTCCGTGTTAAATTTTTCGATCAAGCGAGCCACGGCGCCGACTATATTCGCGTGTACGTTACGAAACAGGGTTACAACGCACTGACCAGTCCGCTGCGTTGGTCCGACCTGGAACTGGTGGGTCAAATTGGTAATACGCCGGCCTCCCAGTGGACCCGCGAAGTTGATGGTGTCTCAATTCAGATTCCGGCCAATGCACCGGGTCGTACCGGCC

	GCCATGTCGTGTATACCATCTGGCAGCGCTCAGGTCTGGACCAATCGTTTTACCTGTGCAGCGATGTTGACTTTGGCGGTTCTGGT
FER$_{res}$	GATATACATATGTCAACGCCGTATCGTCGCCCGCTGCCGCTGGCCGCCGCAATCCTGGGTGTTTGTGCCGTCGTCGCTGCTCTGCTGACCACCGCTTTTAGCGGTCCGGCCAGCGCGCATGGCAGCGTGGTTGATCCGGCCAGCCGTTCTTATAGTTGCTGGCAGCGCTGGGGCGGTGATTTCCAAAACCCGGCAATGGCTACCCAGGACCCGATGTGTTGGCAGGCGTGGCAAGCCGATCCGAACGCAATGTGGAACTGGAATGGCCTGTTTCGTGAAGGTGTGGCGGGCAATCATCAAGGCGCCATTCCGGATGGTCAGCTGTGCTCGGGCGGTCGTACCCAGAGCGGCCGTTATAATGCACTGGATACCGTGGGTGCTTGGAAAACGGTTCCGGTCACCAACAACTTCCGTGTTAAATTTTTCGATCAAGCGAGCCACGGCGCCGACTATATTCGCGTGTACGTTACGAAACAGGGTTACAACGCACTGACCAGTCCGCTGCGTTGGTCCGACCTGGAACTGGTGGGTCAAATTGGTAATACGCCGGCCTCCCAGTGGACCCGCGAAGTTGATGGTGTCTCAATTCAGATTCCGGCCAATGCACCGGGTCGTACCGGCCGCCATGTCGTGTATACCATCTGGCAGCGCTCAGGTCTGGACGAATCGTTTTACCTGTGCAGCGATGTTGACTTTGGCGGTTCTGGT
FER$_{loop}$	GATATACATATGTCAACGCCGTATCGTCGCCCGCTGCCGCTGGCCGCCGCAATCCTGGGTGTTTGTGCCGTCGTCGCTGCTCTGCTGACCACCGCTTTTAGCGGTCCGGCCAGCGCGCATGGCAGCGTGGTTGATCCGGCCAGCCGTTCTTATAGTTGCTGGCAGCGCTGGGGCGGTGATTTCCAAAACCCGGCAATGGCTACCCAGGACCCGATGTGTTGGCAGGCGTGGCAAGCCGATCCGAACGCAATGTGGAACTGGAATGGCCTGTTTCGTGAAGGTGTGGCGGGCAATCATCAAGGCGCCATTCCGGATGGTCAGCTGTGCTCGGGCGGTCGTACCCAGAGCGGCCGTTATAATGCACTGGATACCGTGGGTGCTTGGAAAACGGTTCCGGTCACCAACAACTTCCGTGTTAAATTTTTCGATCAAGCGAGCCACGGCGCCGACTATATTCGCGTGTACGTTACGAAACAGGGTTACAACGCACTGACCAGTCCGCTGCGTTGGTCCGACCTGGAACTGGTGGGTCAAATTGGTAATACGCCGGCCTCCCAGTGGACCCGCGAAGTTGATGGTGTCTCAATTCAGATTCCGGCCAATGCACCGGGTCGTACCGGCCGCCATGTCGTGTATACCATCTGGCAGCGCAGCGACTCTCAAGAATCGTTTTACCTGTGCAGCGATGTTGACTTTGGCGGTTCTGGT

3 Methods

3.1 Site-Directed Mutagenesis

Site-directed mutagenesis was performed using primers that introduced the desired mutations during whole-plasmid polymerase chain reaction (PCR) amplification or by ordering gene fragments containing the desired mutations for direct use in DNA assembly. Whole-plasmid PCR amplification was performed for the three single mutants and the FEH double mutant, while DNA assembly was performed for the remaining mutants. *Ma*LPMO10B with the native signal peptide from *M. aurantiaca* was previously cloned into the bacterial expression vector pRSETB. *Escherichia coli* BL21 (DE3) cells expressing this construct were provided by Zarah Forsberg (Forsberg *et al.*, 2018).

3.1.1 Primer Preparation and Gene Fragment Resuspension

Primers are used for sequence verification and in PCR reactions to amplify DNA and insert mutations. If the desired mutations could not be introduced by a single set of primers due to the number of mutations or that the mutations were too far apart from one another, gene fragments were designed to introduce the desired mutations. The primers and gene fragments were designed and kindly provided by co-supervisor Kelsi Hall. The nucleotide sequence of the primers is shown in Table 6.

Materials:

- Gene fragments (ThermoFisher Scientific) (Table 7)
- Primers (ThermoFisher Scientific) (Table 6)

Method:

Designed primers were received as lyophilized pellets and had to be resuspended before use. The amount of DNA in the tube was reported in nmol and ddH$_2$O was added to a final concentration of 100 µM. Before use, the solution was vortexed to resuspend the pellet. Working stocks of primers were created at a concentration of 10 µM to avoid contamination and excessive freeze-thaw cycles of the 100 µM primer stocks.

The gene fragments ordered from ThermoFisher Scientific did not include the CBM or linker region of *Ma*LPMO10B due to sequence complexity. Therefore, primers were designed to amplify both the pRSETB backbone, and linker region and CBM of *Ma*LPMO10B. The gene fragments were delivered as lyophilized pellets and resuspended with ddH$_2$O to a final concentration of 40 ng/µL.

3.1.2 Site-Directed Mutagenesis using Whole-Plasmid PCR Amplification

Site-directed mutagenesis by whole-plasmid PCR amplification is performed to introduce desired mutations into a specific gene while simultaneously amplifying the plasmid. Forward and reverse primers are designed to introduce the mutations in the nucleotide sequence of the targeted gene. The primers contain overlapping base pairs and point away from one another. Site-directed mutagenesis by whole-plasmid PCR amplification was performed to create the single mutants YEH, FQH, and YQR, as well as the double mutant FEH. YQR is here described as a single mutant since the histidine residue at position 216 is only mutated to a glycine in order to fit the arginine residue at position 214 as previously described in Section 1.6.

Materials:

- DpnI restriction enzyme (New England BioLabs)
- *Ma*LPMO10B_pRSETB template (obtained as described in Section 3.1.9)
- Primers (ThermoFisher Scientific) (Section 3.1.1 and Table 6)
- Q5® High-Fidelity 2 x master mix (New England BioLabs)
- T100^{TM} Thermal Cycler (BioRad)

Method:

To introduce the desired mutations into *Ma*LPMO10B_pRSETB, Q5® High-Fidelity 2 x master mix was used. The master mix includes deoxyribonucleoside triphosphates (dNTPs), Mg^{2+}, buffer, and Q5® DNA polymerase which copies the plasmid. Sample reactions containing the appropriate forward and reverse primers, Q5® High-Fidelity master mix and ddH_2O were made up in PCR tubes for each mutant (Table 8). A 5 µL excess of each reaction was made to be used as a negative control during PCR amplification. Once the components of each sample reaction were prepared and 5 µL was taken out as a negative control, 1 ng of *Ma*LPMO10B_pRSETB plasmid was added to each sample reaction to serve as the template (plasmid isolated from BL21 (DE3) *E. coli* cells as described in Section 3.1.10).

*Table 8. Content of sample reactions to create MaLPMO10B YEH, FQH, YQR, and FEH mutants. *Template was only added to the positive control.*

Components	x 1 reaction	x 1.2 reactions	Final concentration
10 µM forward primer	1.3 µL	1.6 µL	0.5 µM
10 µM reverse primer	1.3 µL	1.6 µL	0.5 µM
Q5® High-Fidelity 2 x master mix	12.5 µL	15.0 µL	1 x
Template*	1.0 µL		1 ng
ddH_2O	8.9 µL	11.8 µL	
Total volume	25.0 µL	30.0 µL	

Whole-plasmid PCR amplification was performed as outlined in Table 9. The eight different primers used to create YQR, FQH, YEH, and FEH have different annealing temperatures due to differences in GC content. The primer annealing temperatures were found using SnapGene or NEB Tm Calculator (https://tmcalculator.neb.com/#!/main). The Q5® High-Fidelity 2 x master mix protocol recommends using an annealing temperature 3 degrees higher than the lowest annealing temperature (NewEnglandBioLabsInc., 2022b). The annealing temperature used for whole-plasmid PCR amplification was 66 °C, 4 °C higher than the lowest annealing temperature of 62 °C. The extension time was determined based on the length of the desired product size. *Ma*LPMO10B_pRSETB is 3847 bp therefore the extension time was set to 1 minute and 50 seconds, as the protocol recommends 20-30 seconds per kb (NewEnglandBioLabsInc., 2022b).

Table 9. PCR conditions for whole PCR amplification of YQR, FQH, YEH, and FEH.

Cycle step	Temperature (°C)	Time (min:sec)	Cycles
Initial denaturation	98	0:30	1 x
Denaturation	98	0:10	30 x
Annealing	66	0:30	
Extension	72	1:50	
Final extension	72	2:00	1 x

Once the PCR was finished, 0.5 µL DpnI was added to each sample reaction and incubated for 1 hour at 37 °C. DpnI is a restriction enzyme which digests methylated DNA, assuring that only newly amplified, non-methylated DNA remains intact in the sample reaction. DpnI was heat inactivated by incubating at 80 °C for 20 minutes. Whole-plasmid PCR amplification was verified by analyzing the PCR product size using DNA agarose gel electrophoresis (Section 3.1.3). Successful whole-plasmid PCR amplification would show a band at approximately 3847 bp for the sample reactions and no band for the negative controls.

3.1.3 DNA Agarose Gel Electrophoresis

DNA fragments can be analyzed by gel electrophoresis in an agarose gel matrix. DNA is negatively charged and will travel towards a positive electrode when an electric current is applied. The gel matrix will separate the DNA fragments based on size, as smaller fragments will travel longer than larger fragments. SYBR^{TM} safe dye is added to the agarose which bind to the DNA and allows it to be visualized using UV light or a blue light transilluminator. DNA agarose gel electrophoresis can be used to verify successful PCR amplification or transformation.

Materials:

- Gel Loading Dye, Purple (6 x) (New England BioLabs)
- GelDoc Go Imaging system (BioRad)
- GeneRuler 1 kB DNA ladder (ThermoFisher Scientific)
- PowerPac^{TM} Basic power supply (BioRad)
- SYBR^{TM} Safe DNA gel stain (ThermoFisher Scientific)
- Tris Acetate-EDTA (10 x) buffer (BioRad)
- Ultrapure Agarose^{TM} (ThermoFisher Scientific)

Method:

A 1 % agarose gel was prepared containing 1 x Tris Acetate-EDTA buffer. The agarose was dissolved in a microwave and once cooled 1 x SYBR Safe DNA gel stain was added. The solution was poured into a casting tray with combs to form wells and set after approximately 20 minutes. GeneRuler 1 kB DNA ladder and PCR reactions mixed with 2 x gel loading dye were added to separate wells and 120 V was applied for 20 minutes to separate the DNA fragments. The gel was analyzed using a blue tray and GelDoc Go Imaging system.

3.1.4 PCR Clean Up

PCR products contain impurities and need to be cleaned to obtain purified DNA. The DNA clean and concentrator® kit from Zymo research removes free dNTPs and modifying enzymes, among other impurities (ZymoResearch, 2021). The PCR product produced in Section 3.1.2

contained DpnI, digested methylated DNA fragments and other contaminants from the PCR which required removal.

Materials:

- DNA clean and concentrator® -5 (Zymo research)
- DpnI-treated PCR product (Section 3.1.2)
- NanoDrop™ One/One^C Microvolume UV-Vis spectrophotometer (ThermoFisher Scientific)

Method:

The PCR product and 5 volumes of DNA binding buffer were combined and vortexed. The sample was transferred to a Zymo Spin™ column and centrifuged for 30 seconds. Next, 200 µL of DNA wash buffer diluted in 100% ethanol was added to the column and centrifuged for 30 seconds. The wash step was performed twice. The column was dried by 2 minutes centrifugation prior to addition of 15 µL warm ddH_2O and incubated at room temperature for 1 minute. The column was transferred to a clean microcentrifuge tube and centrifuged for 1 minute to elute the purified PCR product.

The concentration of purified DNA was measured at 260 nm using a NanoDrop™ One/One^C Microvolume UV-Vis spectrophotometer, then stored at -20 °C.

3.1.5 Preparation of pRSETB Backbone for DNA Assembly

Materials:

- *Ma*LPMO10B_pRSETB template (obtained as described in Section 3.1.9)
- Primers (ThermoFisher Scientific) (Table 6)
- Q5® High-Fidelity 2 x master mix (New England BioLabs)

Method:

The pRSETB backbone was amplified from the *Ma*LPMO10B_pRSETB WT template to generate a linear backbone to be assembled with the gene fragments. As previously mentioned, the linker region and CBM were also amplified. Figure 9 shows were the primers bound to the template.

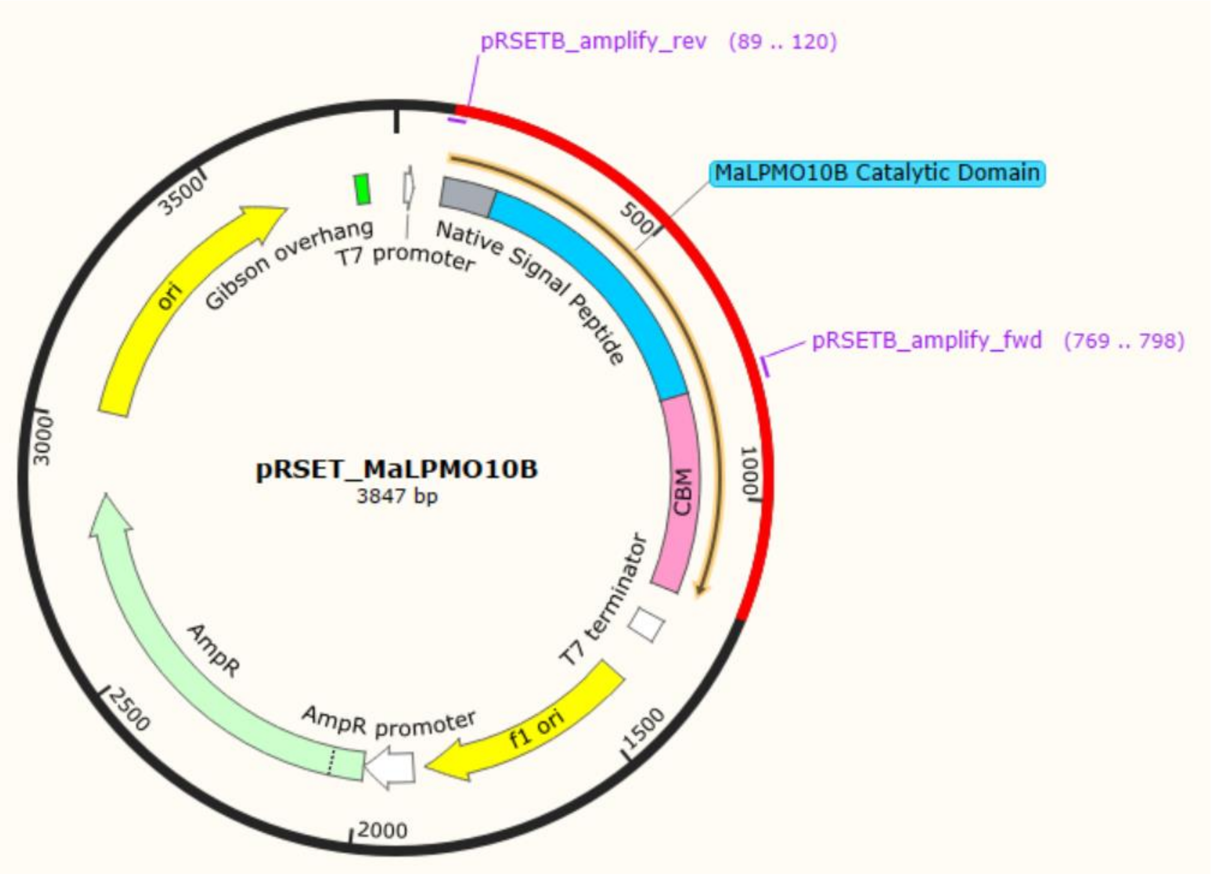

Figure 9. ***The pRSETB backbone with the MaLPMO10B WT gene.*** *The pRSETB_amplify_fwd primer binds at the end of the MaLPMO10B catalytic domain (blue) and beginning of the CBM (pink). The pRSETB_amplify_rev primer (purple) binds the native signal peptide (grey) of MaLPMO10B.*

Q5® High-Fidelity 2 x master mix was used to amplify the backbone with pRSETB_amplify_fwd and rev primers (Table 6) in the same way site-directed mutagenesis with whole-plasmid PCR amplification was performed (Table 8). PCR amplification of the pRSETB backbone was performed as depicted in Table 10. Once PCR amplification was completed, the sample reaction was incubated with DpnI for 1 hour at 37 °C. DpnI was then heat inactivated at 80 °C for 20 minutes. The PCR reaction was verified as described in Section 3.1.3, where a successful PCR amplification of the pRSETB backbone would show a band around 3199 bp. The sample was purified as per Section 3.1.4.

Table 10. PCR conditions for the amplification of pRSETB backbone.

Cycle step	Temperature (°C)	Time (min:sec)	Cycles
Initial denaturation	98	0:30	1 x
Denaturation	98	0:10	30 x
Annealing	70	0:30	
Extension	72	1:30	
Final extension	72	2:00	1 x

3.1.6 Site-Directed Mutagenesis using DNA Assembly

Gene fragments containing the desired mutations were kindly designed and provided by co-supervisor Kelsi Hall and resuspended as per Section 3.1.1. Site-directed mutagenesis by DNA assembly was performed for both triple mutants, FER_{res} and FER_{loop}, and the two double mutants YER and FQR.

Materials:

- Gene fragments (ThermoFisher Scientific) (Table 7)
- NEBuilder HiFi DNA Assembly master mix (New England BioLabs)
- Primers (ThermoFisher Scientific) (Table 6)
- T100^{TM} Thermal Cycler (BioRad)

The pRSETB backbone and gene fragments were incubated with NEBuilder HiFi DNA Assembly master mix to create a plasmid containing the gene with desired mutations. The HiFi DNA assembly protocol recommends 50 to 100 ng vector and a 2-fold molar excess of gene fragments (NewEnglandBioLabsInc., 2022a). Previous attempts using a 2-fold molar excess (not described here) had not been successful, therefore a 4-fold molar excess of gene fragments were used. The pmol amount of backbone was calculated using formula 1.

$$pmols = \frac{weight\ in\ ng \times 1000}{number\ of\ base\ pairs \times 650\ daltons} \tag{1}$$

50 ng of pRSETB backbone equals 0.0276 pmol, meaning that 0.1104 pmol of gene fragments was included in the reaction. This was in line with the protocol that states 0.03 to 0.2 pmol of total DNA fragments should be used (NewEnglandBioLabsInc., 2022a). The amount in ng of DNA fragments can further be calculated by rearranging formula 1. A 10 µL sample reaction is shown in Table 11 and was incubated for 1 hour at 50 °C.

Table 11. Content of sample reactions to create MaLPMO10B FER$_{res}$, FER$_{loop}$, YER and FQR mutants.

Components	Volume (µL)	Amount
Vector (pRSETB backbone)	1.6	0.0276 pmol
2 x NEBuilder master mix	5.0	1 x
Insert (DNA fragment)	2.0	0.1104 pmol
ddH$_2$O	1.4	
Total	10.0	

3.1.7 Transformation into One Shot® TOP10 Chemically Competent *E. coli* Cells

Transformation is performed to insert DNA into chemically competent cells. Chemically competent cells are created by treating cells with calcium chloride which promotes plasmid uptake (ThermoFisherScientific, 2022). The DNA assembly reactions (Section 3.1.6) and whole-plasmid PCR products (Section 3.1.2) are mixtures, containing both the correct plasmid, but also small amounts of incorrectly mutated or truncated versions. The DNA is first transformed into One Shot® TOP10 chemically competent *E. coli* cells which have a high transformation efficiency. One Shot® TOP10 chemically competent *E. coli* cells will not express the protein and will take up either truncated or correct plasmid, while an expression strain such as One Shot® BL21 Star^{TM} (DE3) chemically competent *E. coli* cells would select for plasmids expressing a truncated form of the protein as this would provide a smaller metabolic burden on the cells.

Materials:

- DNA assembly reaction (Section 3.1.6) and whole-plasmid PCR product (Section 3.1.2)
- LB agar plates with 100 µg/mL ampicillin (Table 4)
- One Shot® TOP10 chemically competent *E. coli* cells

The whole-plasmid PCR product (Section 3.1.2) and DNA assembly reaction (Section 3.1.6) were transformed into One Shot® TOP10 chemically competent *E. coli* cells. The cells were thawed on ice, then divided in two, leaving 25 µL of chemically competent cells for each transformation. 1 µL of whole-plasmid PCR product or DNA assembly reaction were added to the cells, mixed gently by tapping and then incubated on ice for 30 minutes. The vials were then incubated at 42 °C for 30 seconds and placed on ice for 1-2 minutes. This heat shock process causes the cells to take up exogenous DNA. Transformants were recovered with the addition of 125 µL of prewarmed SOC-media and incubated at 37 °C and 225 rpm for 1 hour. Dilutions

(20 and 100 µL) of each transformation reaction were plated out on LB agar plates containing 100 µg/mL ampicillin and incubated at 37 °C overnight (~16 hours).

3.1.8 Verifying Successful Transformation and Correct Gene Sequence

Transformation can be verified by screening with PCR to check that cells have taken up plasmid containing the correct insert size followed by sequencing to ensure the correct gene sequence. PCR screening is performed by picking colonies and mixing them with primers and RedTaq DNA Polymerase 2 x master mix which includes thermostable Taq DNA polymerase, dNTPs, buffer, and dye mix for direct application on an agarose gel.

Materials:

- LB media supplemented with 100 µg/mL ampicillin (Table 4)
- Primers (ThermoFisher Scientific) (Table 6)
- RedTaq DNA Polymerase 2 x master mix (VWR)
- T100^{TM} Thermal Cycler (BioRad)

Method:

A PCR reaction mix was prepared by mixing RedTaq 2 x master mix, pRSETB_insert_fwd and rev primers, and ddH$_2$O as displayed in Table 12. The reaction mix contained a total volume of 10 µL and a sample of a single colony. A negative control was also included containing no colony sample. On average, 5 colonies were screened per plasmid.

Table 12. Content of PCR reactions to verify successful transformation of MaLPMO10B plasmids into One Shot® TOP10 chemically competent E. coli cells.

Components	**x 1 reaction**	**Final concentration**
RedTaq 2 x Master Mix	5.0 µL	1 x
pRSETB_insert_fwd (10 µM)	0.5 µL	0.5 µM
pRSETB_insert_rev (10 µM)	0.5 µL	0.5 µM
ddH$_2$O	4.0 µL	
Colony	Colony stab	
Total	10.0 µL	

Table 13 shows the PCR conditions used to amplify the *Ma*LPMO10B gene from the pRSETB plasmid in transformed cells. The annealing temperature was set to 60 °C based on the annealing temperature of the primers used. The extension time was set to 1 minute and 15 seconds as the length of the *Ma*LPMO10B gene sequence is 1140 bp and the RedTaq master mix protocol recommends a 1 minute extension time per kb (VWR, 2022).

Table 13. PCR conditions for the amplification of MaLPMO10B gene sequence in transformed cells.

Cycle step	**Temperature (°C)**	**Time (min:sec)**	**Cycles**
Initial denaturation	98	0:30	1 x
Denaturation	98	0:10	30 x
Annealing	60	0:30	
Extension	72	1:15	
Final extension	72	2:00	1 x

The PCR reactions were analyzed by DNA agarose gel electrophoresis (Section 3.1.3). A successful transformation would show a band at approximately 1140 bp.

Colonies with successful transformation were used to inoculate 3 mL LB media supplemented with 100 µg/mL ampicillin and incubated overnight at 37 °C and 200 rpm. Plasmids from the cell cultures were isolated and sent to Eurofins Genomics for sequence verification as described in Section 3.1.9.

3.1.9 Plasmid Isolation and Glycerol Stock Preparation

Glycerol stocks contain a dense cell culture mixed with glycerol for long-term storage of bacterial strains. Plasmids are isolated from dense cell cultures by using kits, such as E.Z.N.A.® Plasmid DNA Mini Kit I. The solutions in the kit cause the cells to lyse and the plasmids are purified and separated from genomic DNA and other cellular debris.

Materials:

- 5430 R centrifuge (Eppendorf)
- AV-100 laminar air flow cabinet (Telstar)
- Cryotubes (Sarstedt)
- Colonies from agar plates (Section 3.1.7 and Section 3.1.10)
- E.Z.N.A.® Plasmid DNA Mini Kit I (Omega Bio-Tek)
- LB agar supplemented with 100 µg/mL ampicillin (Table 4)
- MiniSpin centrifuge (Eppendorf)
- Multitron Standard shaking incubator (Infors HT)
- NanoDrop™ One/One^{C} Microvolume UV-Vis spectrophotometer (ThermoFisher Scientific)

Method:

E. coli TOP10 or BL21 (DE3) cells containing *Ma*LPMO10B_pRSETB WT or mutant plasmid were picked from a single colony into a 50 mL falcon tube containing 5 mL LB media and 100 µg/mL ampicillin under sterile conditions. Cells were grown at 37 °C and 180 rpm in a shaking incubator overnight. Prior to plasmid isolation, 700 µL of cell culture was mixed 1:1 with autoclaved 80 % glycerol in a cryotube and stored at -80 °C.

Plasmid isolation was performed using E.Z.N.A.® Plasmid DNA Mini Kit I, spinning down the remaining cell culture at 5000 x g for 5 minutes. The supernatant was decanted, and the pellet was resuspended in 250 µL of solution I. Solution I contains RNAase to eliminate any RNA contamination.

The resuspended cells were moved to a 1.5 mL Eppendorf tube and 250 µL of solution II was added to lyse the cells during a 2-3 minute incubation. 350 µL of solution III was then added and the tube was inverted several times to form a white flocculent which was centrifuged at 13 400 x g for 10 minutes, forming a white pellet. The supernatant containing the plasmid was transferred to a HiBind® Mini Column included in the kit and centrifuged for 1 minute. 500 µL of HBC buffer diluted in isopropanol was added to the column and centrifuged for 1 minute. The column was washed twice with 700 µL DNA wash buffer diluted in ethanol and centrifuged for 30 seconds upon each addition. Centrifugation for 2 minutes dried the column. The plasmid was eluted by adding 50 µL of warm ddH_2O and incubating for 1 minute at room temperature. The column was placed in a clean 1.5 mL Eppendorf tube and the plasmid was collected by centrifuging the column for 1 minute. The plasmid was stored at -20 °C.

The plasmid concentration was measured at 260 nm using a NanoDrop^{TM} One/One^{C} Microvolume UV-Vis spectrophotometer. If sequencing was required, 6 µL of plasmid DNA (at 100 ng/µL) and 6 µL of SignalP_fwd primer (at 5 pmol/µL) (Table 6) were mixed and sent for sequencing at Eurofins Genomics to verify the correct *Ma*LPMO10B gene sequence.

3.1.10 Transformation into One Shot® BL21 Star^{TM} (DE3) Chemically Competent *E. coli* Cells

One Shot® BL21 Star^{TM} (DE3) chemically competent *E. coli* cells have a lower transformation efficiency compared with One Shot® TOP10 chemically competent *E. coli* cells. However, the strain is suited for protein expression as it contains the gene encoding T7 RNA polymerase which is required for protein expression from the pRSETB plasmid. If the plasmids were not transformed into One Shot® TOP10 chemically competent *E. coli* cells and sequence verified first, One Shot® BL21 Star^{TM} (DE3) chemically competent *E. coli* cells would preferentially select for plasmids expressing a truncated form of the protein as this would cause less metabolic burden on the cells.

Materials:

- LB Agar plates supplemented with 100 µg/mL ampicillin (Table 4)
- One Shot® BL21 Star^{TM} (DE3) chemically competent *E. coli* cells
- Sequence verified *Ma*LPMO10B mutant plasmids (Section 3.1.8)

After the correct gene sequence was verified, *Ma*LPMO10B mutant plasmids were transformed into One Shot® BL21 Star^{TM} (DE3) chemically competent *E. coli* cells. Transformation was performed as described in Section 3.1.7 using One Shot® BL21 Star^{TM} (DE3) chemically competent *E. coli* cells mixed with 1 ng of plasmid DNA. Dilutions (20 µL and 100 µL) of each transformation reaction were plated out on LB agar plates supplemented with 100 µg/mL ampicillin. The agar plates were incubated at room temperature for three days as slower growth appeared to give healthier colonies.

3.2 Expression and Purification of *Ma*LPMO10B WT and Mutants

3.2.1 Cultivation of *Ma*LPMO10B WT and Mutants

Bacteria containing a desired gene are cultivated in large scale to obtain a fully folded protein of interest.

Materials:

- Aeration system with sparger lids
- Antifoam 204 (Merck)
- AV-100 laminar air flow cabinet (Telstar)
- Freshly transformed BL21 (DE3) colonies containing pRSETB mutant plasmid (Section 3.1.10) or *Ma*LPMO10B WT glycerol stock (Section 3.1.9)
- LB media supplemented with 100 µg/mL ampicillin (Table 4)
- Multitron Standard shaking incubator (Infors HT)
- TB media supplemented with 100 µg/mL ampicillin (Table 4)

Method:

*Ma*LPMO10B_pRSETB WT was picked with a sterile pipette tip into a 50 mL falcon tube with 5 mL LB media supplemented with 100 µg/mL ampicillin in a sterile cabinet. The cells were incubated for 20 hours at 30 °C and 200 rpm to have a starting culture for large scale cultivation.

Large scale cultivation was performed using an aeration system similar to the Harbinger system (Epiphyte, 2022). Sparger lids were connected to an airflow, allowing aeration of the cell culture in glass bottles. Glass bottles containing 500 mL sterile and rich TB media, ideal for bacterial growth, was supplemented with 100 µg/mL ampicillin and 50 µL of antifoam prior to adding the starting culture of *Ma*LPMO10B WT or a freshly transformed mutant colony. *Ma*LPMO10B WT was grown at 30 °C for 20 hours, while the mutants were grown at 37 °C overnight. The mutants expressed better at 37 °C and the WT expressed better at 30 °C.

3.2.2 Periplasmic Extract of *Ma*LPMO10B WT and Mutants

Gram-negative *E. coli* BL21 (DE3) strain with *Ma*LPMO10B_pRSETB plasmid produce the protein with a signal peptide. The signal peptide ensures export of the protein to the periplasmic space, located between the inner and the outer membrane. Therefore, a periplasmic extract is required to harvest the protein from the cell culture.

Materials:

- 0.45 µm syringe filter (Sarstedt)
- 5430 R centrifuge (Eppendorf)
- Cell culture (Section 3.2.1)
- $MgCl_2$ (10 mM)
- PMSF (50 mM)
- Sorvall LYNX 6000 centrifuge (ThermoFisher Scientific)
  - F21-8 x 50y rotor
  - F9-6 x 1000 LEX rotor
- Spheroplast buffer (Table 4)

Method:

The cell culture was poured into 1 L centrifuge bottles and centrifuged at 4 °C and 7 808 x g for 12 minutes in the F9-6 x 1000 LEX rotor to obtain a cell pellet. The supernatant was decanted, and the pellet resuspended with 100 mL ice-cold spheroplast buffer and 62.5 µL of the protease inhibitor, phenylmethylsulphonyl fluoride (PMSF). Once resuspended, the pellet was divided in three 50 mL falcon tubes and centrifuged at 4 °C and 7197 x g for 12 minutes with a 5430 R centrifuge. 1 mL of the supernatant was collected as the sucrose fraction for SDS-PAGE analysis to ensure that the protein remained in the pellet. The remaining supernatant was decanted, and the pellets were incubated at room temperature for 30 minutes. 25 mL of ice-cold ddH_2O water and 700 µL of 10 mM $MgCl_2$ was divided over the three tubes and used to resuspend the pellets. The resuspended pellets were poured into a 30 mL centrifuge bottle and centrifuged at 4 °C and 47 850 x g for 12 minutes using a F21-8 x 50y rotor. The supernatant containing the protein was filtered through 0.45 µm syringe filters and stored at 4 °C until use.

3.2.3 Anion Exchange Chromatography

Anion exchange chromatography is a technique which exploits a protein's surface charge to separate molecules. The column resin, also called stationary phase, consists of a cross-linked beaded matrix with positively charged sites which interact with anions (Miller, 2005). Anions interacting with the resin are displaced by the negatively charged molecules in the sample applied to the column. The salt content and pH of the aqueous mobile phase are crucial to the technique since a salt gradient is normally applied to elute the protein of interest, and the pH decide the protein's affinity for the column (Miller, 2005). When an anion exchange column is used, the protein's affinity for the column will increase if the pH of the mobile phase is higher than the isoelectric point (pI) of the protein (when the net charge of the protein is zero). This is because in a solution where the pH is higher than the pI of the protein, the protein is negatively charged. Theoretical pI of a protein can be found using the ProtParam tool provided by Expasy (https://web.expasy.org/protparam/).

Materials:

- 25 mM Bis-Tris propane pH 9.5, 1 M NaCl (Table 4)
- 25 mM Bis-Tris propane pH 9.5 (Table 4)
- Filtered periplasmic extract (Section 3.2.2)
- HiTrap™ DEAE Sepharose FF 5 mL column (Cytiva)
- Software: Unicorn 6.4
- System: ÄktaPure (Cytiva)

Method:

A HiTrap™ DEAE Sepharose FF 5 mL column was used to purify *Ma*LPMO10B WT and the mutants. This column consisted of a resin where the functional group was a weak anion exchanger. In this case, *Ma*LPMO10B WT and the mutants exhibited a low affinity for the column resin and eluted in the flow-through, despite the proteins having a theoretical pI of 7.1 (Table 14) and using a buffer at pH 9.5. However, most other proteins present in the sample interacted with the stationary phase and *Ma*LPMO10B WT and the mutants eluted relatively pure in the unbound flow-through (Forsberg *et al.*, 2018).

The column was washed with 4 column volumes of ddH_2O, then 4 column volumes of buffer B (25 mM Bis-Tris propane pH 9.5, 1 M NaCl), to ensure no proteins remained bound to the column. Buffer A (25 mM Bis-Tris propane pH 9.5) was applied for 4 column volumes until the UV and conductivity trace lines stabilized, ensuring column equilibration. The sample line was flushed with buffer A and the periplasmic extract was equilibrated to buffer A by addition of Bis-Tris propane to a final concentration of 25 mM. The periplasmic extract (Section 3.2.2) was then loaded onto the column through the sample line using a flow rate of 1 mL/min. Flow-through containing *Ma*LPMO10B started to elute after approximately 2 column volumes and was collected in 2 mL fractions. Following elution of the *Ma*LPMO10B protein, the column was washed with buffer B and then buffer A, each for 4 column volumes. This wash step was performed twice. Further, the column and system were washed with ddH_2O, then stored in 20 % ethanol.

3.2.4 Physiochemical Properties of *Ma*LPMO10B WT and the Mutants

The physiochemical properties of a protein, such as molecular weight, extinction coefficient, and theoretical pI is essential when calculating protein concentration and yield, and when deciding the pH of the buffer during purification. A tool such as ProtParam from Expasy can be used to find the physiochemical properties. However, the theoretical pI calculated by the software is only based on the amino acid sequence and does not consider how the protein folds. The pI provided may therefore not be correct.

Materials:

- ProtParam tool provided by Expasy
- Translate tool provided by Expasy

Method:

The nucleotide sequence of *Ma*LPMO10B WT and the mutants without the signal peptide were translated using the translate tool from by Expasy (https://web.expasy.org/translate/). The physiochemical properties of protein were then obtained from Expasy using the ProtParam tool (https://web.expasy.org/protparam/). The amino acid sequence without the signal peptide for each protein was entered into the tool and the software calculated the molecular weight (Da), the extinction coefficient (M^{-1} cm^{-1}), and the theoretical pI (Table 14).

Table 14. The physiochemical properties of MaLPMO10B WT and the mutants. The molecular weight in Da, the extinction coefficient in M^{-1} cm^{-1} and the theoretical pI calculated by the ProtParam tool for each protein without the signal peptide is shown.

	Amino acid code	**Molecular weight (Da)**	**Extinction coefficient (ε in M^{-1} cm^{-1})**	**Theoretical pI**
WT	YQH	34 906	93 765	7.1
Single mutants	YQR	34 911	93 765	7.8
	FQH	34 890	92 275	7.1
	YEH	34 907	93 765	6.6
Double mutants	FEH	34 891	92 275	6.6
	YER	34 912	93 765	7.0
	FQR	34 895	92 275	7.8
Triple mutants	FER_{res}	34 896	92 275	7.1
	FER_{loop}	34 941	92 275	7.1

3.2.5 Sodium Dodecyl Sulfate-Polyacrylamide Gel Electrophoresis (SDS-PAGE)

SDS-PAGE is used to analyze protein size and purity by applying charge through an SDS-PAGE gel in a cell. Proteins are reduced and denatured by treatment with a reducing agent and boiling. Sodium dodecyl sulfate in the gel ensures a negative charge of the denatured protein and migration through the gel from negative to positive charge. Small molecules will migrate further than large molecules and the size of a protein band can be determined using a protein ladder. If the gel is stained with Coomassie blue it can be analyzed directly, or if the gel is stain-free, an imager with fluorescent light can be used for analysis.

Materials:

- Benchmark™ protein ladder (ThermoFisher Scientific)
- Dye mix (2 x NuPage® LDS Sample buffer containing NuPage® Sample reducing agent) (ThermoFisher Scientific)
- GelDoc Go Imaging System (BioRad)
- Mini-PROTEAN® tetra cell (BioRad)
- Mini-PROTEAN® TGX stain-free precast gel (BioRad)
- PowerPac™ basic power supply (BioRad)
- Protein fractions (Section 3.2.3)

- T100^{TM} Thermal Cycler (BioRad)
- Tris/Glycine/SDS buffer (1 x) (BioRad)

Method:

The fractions collected during anion exchange chromatography (or later from size exclusion chromatography (SEC)) were analyzed by SDS-PAGE to determine which fractions contained *Ma*LPMO10B protein. 2 x dye mix and fractions were mixed 1:1 in a PCR tube to a final volume of 20 µL and incubated for 5 min at 95 °C to denature the protein. The samples and Benchmark^{TM} protein ladder were loaded on a mini-PROTEAN® TGX stain-free precast gel fitted in a gel chamber in the mini-PROTEAN® tetra cell filled with tris/glycine/SDS buffer. The PowerPac^{TM} basic power supply was connected to the cell and 180 V was applied for 37 minutes. The gel was analyzed using a GelDoc Go Imaging system with a UV/Vis stain-free tray under fluorescent light. Fractions which included a band around 34.9 kDa, corresponding to the size of *Ma*LPMO10B, were pooled for further purification.

3.2.6 Copper Saturation

The active site of LPMOs contain a Cu(II) atom that need to be reduced to Cu(I) in order to oxidatively cleave a substrate, as described in Section 1.4.4 (Quinlan *et al.*, 2011; Vaaje-Kolstad *et al.*, 2010). Purified LPMOs must therefore be copper saturated to achieve activity. However, excess copper content in the protein solution will give false results in some assays and it is therefore crucial that free copper is properly removed (Stepnov *et al.*, 2021). Excess copper can be removed by a range of methods, but desalting methods such as SEC or small gravity-flow gel filtration columns, as well as centrifugation of the protein solution with centrifugal filter units, are the most common options for removal. In this instance, copper removal by centrifugation lead to protein precipitation and loss of protein (not described here), so SEC was used to remove excess copper. Protein solutions which have undergone SEC for removal of copper have previously been shown to contain only negligible amounts of free copper (Stepnov *et al.*, 2021).

Materials:

- 5430 R centrifuge (Eppendorf)
- Amicon® Ultra-15 centrifugal filter units with 10 000 Da MWCO (Merck)
- $Cu(II)SO_4$ (150 mM)
- NanoDrop^{TM} One/One^{C} Microvolume UV-Vis spectrophotometer (ThermoFisher Scientific)

- Pooled fractions (Section 3.2.3)

Methods:

The protein concentration of the pooled fractions from anion exchange chromatography were measured at 280 nm using a NanoDrop^{TM} One/One^{C} Microvolume UV-Vis spectrophotometer. The extinction coefficient for each protein was found using the ProtParam tool provided by Expasy (Table 14). 3 x molar excess of Cu(II)SO_4 was added to the pooled fractions and incubated for 30 minutes on ice. The copper saturated pooled fractions were concentrated down to 1 mL using an Amicon® centrifugal filter unit with a 10 kDa molecular weight cut off (MWCO). Simultaneously, the protein was buffer exchanged into Tris-HCl pH 7.5.

3.2.7 Size Exclusion Chromatography

Size exclusion chromatography is a technique which separates molecules, such as proteins, based on size. The resin consists of inert porous beads, where smaller molecules will enter the beads, while larger molecules will travel around the beads (Miller, 2005). This causes the smaller molecules to have longer retention times and high molecular weight molecules will elute first. Protein elution from the column is monitored at 280 nm by UV detection.

Materials:

- 50 mM Tris-HCl pH 7.5, 200 mM NaCl (Table 4)
- Amicon® Ultra-15 centrifugal filter units with 10 000 Da MWCO (Merck)
- Copper saturated protein (Section 3.2.6)
- Ethanol (20 %)
- HiLoad® 16/600 Superdex® 75 pg 120 mL column (Cytiva)
- NanoDrop^{TM} One/One^{C} Microvolume UV-Vis spectrophotometer (ThermoFisher Scientific)
- Sodium acetate (0.2 M in 20 % ethanol)
- Software: Unicorn 5.2
- System: ÄktaPurifier (Cytvia)

Method:

A HiLoad® 16/600 Superdex® 75 pg 120 mL column was used to purify *Ma*LPMO10B with a size of 34.9 kDa since the column can separate molecules between 3 and 70 kDa. The column and ÄktaPurifier system were washed with 1 column volume of ddH_2O and then equilibrated with 1 column volume of 50 mM Tris-HCl pH 7.5, 200 mM NaCl. Column pressure was monitored by increasing the flow rate stepwise from 0.2 to 1 mL/min over a period of 5 minutes. Once the UV and conductivity traces were stabilized, the system was paused and 20 mL of 50 mM Tris-HCl pH 7.5, 200 mM NaCl was flushed through the sample loop. The 1 mL protein sample was injected onto the sample loop while the system was paused, then loaded onto the column with a flow rate of 1 mL/min. The protein eluted after approximately 0.5 column volumes and 2 mL fractions were collected. After the protein had eluted, the system and column were washed with ddH_2O for 1 column volume. The column was stored in 0.2 M sodium acetate in 20 % ethanol, while the system tubing was stored in 20 % ethanol.

The protein fractions collected during SEC were analyzed by SDS-PAGE as described in Section 3.2.5, and the pure protein fractions were pooled. The pooled protein fractions were concentrated using Amicon® centrifugal filter units with a 10 kDa MWCO. Simultaneously, the protein was buffer exchanged into 20 mM sodium phosphate buffer pH 6 for storage. Buffer exchanging a protein into an alternative buffer was performed in the same manner. The flow-through from concentrating the samples were collected to measure the amount of free copper (Section 3.3.4). A NanoDrop^{TM} One/One^{C} Microvolume UV-Vis spectrophotometer was used to measure the final protein concentration at 280 nm. The proteins were stored at 4 °C.

3.3 Enzyme Activity Assays

3.3.1 Enzyme Reactions

LPMOs cleave the glycosidic bonds of recalcitrant polysaccharides at either the C1- or C4-position as previously described in Section 1.4.2. Reactions with LPMO, substrate, buffer, and reductant are incubated for up to 24 hours with or without external addition of hydrogen peroxide. Samples are collected at specific time point for analysis of soluble C1- and C4-oxidized cello-oligosaccharides or of C1-oxidized chito-oligosaccharides depending on whether cellulose or chitin was used as substrate. *Ma*LPMO10B is strictly active on insoluble substrate and the reactions are therefore stopped by separating the insoluble substrate from the LPMO. HPAEC-PAD analysis can be used to detect the C1- and C4-oxidized cello-oligosaccharides, whereas UHPLC can be used to detect the C1-oxidized chito-oligosaccharides.

Materials:

- 2 mL Eppendorf tubes
- 96-Well Microtiter^{TM} microplate (ThermoFisher Scientific)
- Ascorbic acid (10 mM)

- Cysteine (10 mM)
- Gallic acid (10 mM)
- H_2O_2 (500 µM)
- *Ma*LPMO10B WT and mutants (50 µM) (Section 3.2.7)
- MultiScreen® HTS 96-well filter plates (Merck)
- MultiScreen® HTS vacuum manifold (Merk)
- Phosphoric acid swollen cellulose (PASC) (0.9 % w/v)
- *Sm*CHB (6.2 µM) (provided by Ole Golten)
- Sodium phosphate buffer pH 6 or pH 8 (500 mM)
- *Tf*Cel6A (2 µM) (provided by Kelsi Hall)
- Thermomixer C (Eppendorf)
- β-chitin (2 % w/v)

Method:

All enzyme reactions were performed using 1 µM *Ma*LPMO10B WT or mutants, 50 mM sodium phosphate buffer pH 6 or pH 8, and 0.1 % w/v PASC or 1 % w/v β-chitin. The LPMO reactions under O_2 conditions also contained 1 mM reductant (ascorbic acid, gallic acid, or cysteine), while the reactions where hydrogen peroxide was externally added contained 10 µM ascorbic acid and 100 µM H_2O_2. All the components except reductant and hydrogen peroxide were mixed in 2 mL Eppendorf tubes. The hydrogen peroxide-driven reactions were pre-heated for 2 minutes prior to addition of hydrogen peroxide and reductant. The reductant was added to initiate the reaction. All reactions were incubated in a thermomixer C at 40 °C and 1000 rpm. Samples were collected at specific time points (30 seconds to 24 hours) and directly filtered using a MultiScreen® HTS 96-well filter plate with a MultiScreen® vacuum manifold to stop the reaction.

The samples containing PASC substrate were incubated at 37 °C and 180 rpm overnight with 0.67 µM of GH6 cellobiohydrolase from *Thermobifida fusca* (*Tf*Cel6A), provided by Kelsi Hall. This was to break down the larger oxidized cellulose products to a degree of polymerization of 2 and 3 (DP2 and DP3). The samples containing β-chitin as substrate were incubated at 37 °C with 0.25 µM of chitobiase from *Serratia marcescens* (*Sm*CHB) overnight. *Sm*CHB degraded the oxidized chito-oligosaccharides to a degree of polymerization of 2 (DP2; A2ox). This allowed for simpler and more accurate quantification of the oxidized products.

3.3.2 HPAEC-PAD Analysis of Oxidized Cellulose Oligosaccharides

High-performance anion exchange chromatography with pulsed amperometric detection (HPAEC-PAD) is a method which separates oligosaccharides with high resolution and sensitivity (Westereng *et al.*, 2013). The column consists of an anion resin, where deprotonated hydroxyl groups on the oligosaccharides will interact with the anion exchange sites in the resin (Cataldi *et al.*, 2000). Hydroxyl groups on the oligosaccharides are deprotonated by the high pH of the eluents (Cataldi *et al.*, 2000). A salt gradient is applied to the column and the oligosaccharides will elute according to their size (Østby *et al.*, 2022). Small oligosaccharides will have a shorter retention time than longer oligosaccharides. The Dionex ICS-6000 includes an eluent generator which mixes ddH_2O with the eluents to a desired concentration at specific times during the analysis. A gold electrode is used for detection of the oligosaccharides.

Materials:

- C1-oxidized standards (provided by Thales de Freitas Costa)
- C4-oxidized standards (provided by Kelsi Hall)
- Dionex CarboPac^{TM} PA200 1 x 250 mm analytical column and 1 x 50 mm guard column (ThermoFisher Scientific)
- Eluents: concentrated potassium hydroxide (KOH) and potassium methanesulfonate (KMSA) (ThermoFisher Scientific)
- HPLC vials and lids (VWR)
- Software: Chromeleon 7
- System: Dionex ICS-6000 (ThermoFisher Scientific)
- Time course samples (Section 3.3.1)

Method:

The Dionex ICS-6000 with a Dionex CarboPac^{TM} PA200 1 x 250 mm analytical column and a 1 x 50 mm guard column was used to analyze the concentration of DP2 and DP3 cellulose oligosaccharides in the samples collected in Section 3.3.1. The potassium hydroxide (KOH) eluent ensured a high pH to deprotonate the sugar hydroxyl groups and a salt gradient of potassium methanesulfonate (KMSA) was applied to elute the oxidized cellulose oligosaccharides. The column oven was set to 30 °C and the flow rate was at 0.063 mL/min. The low flow rate combined with the small-diameter column ensured high quality separation of the oxidized products and a stable baseline.

Two different methods were used; a 50-minute method that gave high quality separation of both C1- and C4-oxidized products, and a 26-minute method most suited for analyzing C1-oxidized products but DP2 and DP3 C4-oxidized products could still be detected, albeit at a lower resolution. For both methods, KOH was applied at a 100 mM concentration for the entire analysis. The 50-minute method had a KMSA gradient increasing from 0 to 100 mM over 27 minutes, while the KMSA gradient for the 26-minute method increased from 1 to 100 mM over 14 minutes. The KMSA concentration was set to 0 mM after 36 minutes for the 50-minute method and 1 mM after 17 minutes for the 26-minute method for the remaining analysis time.

Varying concentrations of DP2 and DP3 C1- and C4-oxidized standards were analyzed to provide a standard curve and determine the concentration of oxidized cellulose oligosaccharides in the samples. The C1-oxidized standard was provided by Thales de Freitas Costa and produced as described previously (Zamocky *et al.*, 2008). The C4-oxidized standard was provided by Kelsi Hall and produced as previously described in Müller *et al.* (2015). The filtered time course samples (Section 3.3.1) were diluted with ddH$_2$O prior to analysis due to the high sensitivity of the Dionex ICS-6000 with the specific column.

3.3.3 UHPLC Analysis of Oxidized Chitin Oligosaccharides

Ultra high-performance liquid chromatography (UHPLC) is a rapid method which can be used to accurately analyze sugar units such as oxidized chito-oligosaccharides. The oligosaccharides will be separated based on size and are detected by a UV detector. The amount of detected product can then be quantified.

Materials:

- A2ox standard (3 mM) (provided by Rannei Skaali)
- Rezex RFQ-Fast Acid H$^+$ (8 %) 7.8 x 100 mm column (Phenomenex)
- System: Dionex UltiMate 3000 (ThermoFisher Scientific)
- Sulfuric acid (5 mM)
- HPLC vials and lids (VWR)
- Software: Chromeleon 7
- Time course samples (Section 3.3.1)

Method:

The Rezex RFQ-Fast Acid H$^+$ (8 %) 7.8 x 100 mm column attached to the Dionex UltiMate 3000 system was used to analyze the concentration of A2ox from the collected samples (Section 3.3.1). A 6-minute method was used with a flow rate of 1 mL/min at 85 °C. This method applied isocratic elution with 5 mM sulfuric acid and the A2ox products were detected at 194 nm using a UV detector. To quantify the A2ox product, a standard curve was generated using various concentrations of an A2ox standard provided by Rannei Skaali. The standard was prepared as previously described by Loose *et al.* (2014).

3.3.4 Amplex Red Assay – the Oxidase Activity Assay

The amplex red assay, also called the Kittl assay, looks at the LPMO's ability to convert molecular oxygen to hydrogen peroxide in the presence of a reductant and absence of substrate (Kittl *et al.*, 2012). This is a coupled enzyme assay, where the hydrogen peroxide produced by the LPMO is used in a reaction between amplex red and horseradish peroxide (HRP), where amplex red is converted to resorufin. HRP consumes hydrogen peroxide rapidly, ensuring that the enzyme will not inactivate during the reaction (Kittl *et al.*, 2012). The stochiometric conversion of hydrogen peroxide to resorufin is 1:1, therefore hydrogen peroxide production by the enzyme can be measured by monitoring the resorufin signal. Resorufin has an absorbance which can be measured at 540 nm using a plate reader. A hydrogen peroxide standard curve is created to determine the hydrogen peroxide concentration in the sample reactions at each time point.

Materials:

- 96-Well Microtiter^{TM} Microplate (ThermoFisher Scientific)
- Amplex red (10 mM)
- Ascorbic acid (10 mM)
- Cu(II)SO_4 (50 µM)
- Cysteine (10 mM)
- Flow-through (to test copper content) (Section 3.2.7)
- Gallic acid (10 mM)
- H_2O_2 (200 µM)
- HRP (100 U/mL)
- *Ma*LPMO10B WT and mutants (50 µM) (Section 3.2.7)
- mgLPMO10 (50 µM) (provided by Kelsi Hall)
- Multichannel pipette (VWR)
- Multiscan FC plate reader (ThermoFisher Scientific)
- *Sc*LPMO10C (50 µM) (provided by Kelsi Hall)
- Sodium phosphate buffer pH 6 or pH 8 (500 mM) (Table 4)

- Software: SkanIt RE 6.1.1
- TraceSELECT® water (Honeywell)

Method:

The amplex red assay was performed on *Ma*LPMO10B WT, all the mutants, mgLPMO10 and, *Sc*LPMO10C at pH 6 with ascorbic acid as reductant. Additionally, the assay was performed with gallic acid and cysteine at pH 6 and ascorbic acid, gallic acid, and cysteine at pH 8 for *Ma*LPMO10B WT and the YEH mutant.

Amplex red and HRP were mixed in 50 mM sodium phosphate buffer and TraceSELECT® water to create the dye mix. The amount of dye mix created was equivalent to the number of reactions, and the final concentration of amplex red and HRP in the samples were 100 µM and 5 U/mL, respectively. 40 µL sample reactions were created with 2 µM of enzyme in 50 mM sodium phosphate buffer and TraceSELECT® water. A hydrogen peroxide standard curve was created with 0, 2, 5, 20, and 40 µM hydrogen peroxide in 50 mM sodium phosphate buffer and TraceSELECT® water. Control reactions with flow-through, free copper, no enzyme, and no reductant were created. Flow-through was collected when concentrating and equilibrating the purified protein to the storage buffer (Section 3.2.7) and was tested to ensure that free copper was removed from the protein solution (see Section 3.2.6 for further explanation). The copper control reactions contained 2 µM of Cu(II)SO_4 and the flow-through control reactions contained 4 µL of flow-through. The control reaction without enzyme contained 50 mM sodium phosphate buffer and TraceSELECT® water. 40 µL of the no reductant control was created with 2 µM enzyme, and 10 µL of TraceSELECT® water was added since the reductant was not going to be included.

50 µL of dye mix was added to all sample and control reactions, then the 96-well plate was incubated for 5 minutes at 30 °C in the Multiscan FC plate reader. After the 5-minute incubation, 10 µL of reductant, to a final concentration of 1 mM, and 50 µL of dye mix was added to the hydrogen peroxide standard curve samples with a multichannel pipette. The standard curve was measured at 540 nm every 10 seconds for 2-3 minutes. The standard curve goes to complete conversion, therefore only one time point is necessary. However, it was monitored over a short period of time to ensure stability. The sample reactions were then initiated with 10 µL of reductant to a final concentration of 1 mM. The reactions were measured at 540 nm every 10 seconds for a minimum of 344 seconds.

3.3.5 Breslmayr Assay – the Peroxidase Activity Assay

LPMOs can use hydrogen peroxide as a co-substrate to oxidize glycosidic bonds, as previously described in Section 1.4.4. The Breslmayr assay is a peroxidase activity assay where 2,6-dimethoxyphenol (2,6-DMP) is oxidized by the LPMO to form a 2,6-DMP radical. Two 2,6-DMP radicals will form a dimer in solution called hydrocoerulignone. Hydrocoerulignone is then oxidized by the LPMO to coerulignone. The presence of coerulignone in the reaction can be measured at 473 nm. Oxidation of 2,6-DMP is the rate limiting step in the reaction, as oxidation of hydrocoerulignone is approximately 15 times faster than oxidation of 2,6-DMP (Breslmayr *et al.*, 2018). The assay therefore estimates how well the LPMO can utilize hydrogen peroxide to oxidize 2,6-DMP. In this assay, no external molecule is exclusively added for reduction of Cu(II) to Cu(I). 2,6-DMP is therefore used as both the reductant and the substrate. In addition, 2,6-DMP is not a natural substrate for LPMOs, which may be a drawback to this method.

Materials:

- 2,6-DMP (100 mM)
- 96-Well Microtiter^{TM} Microplate (ThermoFisher Scientific)
- H_2O_2 (1 mM)
- *Ma*LPMO10B WT and mutants (50 µM) (Section 3.2.7)
- Multichannel pipette (VWR)
- Multiscan FC plate reader (ThermoFisher Scientific)
- Sodium phosphate buffer pH 6 (500 mM)
- Software: SkanIt RE 6.1.1
- TraceSELECT® water (Honeywell)

Method:

The reaction contained a final reaction concentration of 100 µM hydrogen peroxide, 50 mM sodium phosphate buffer pH 6, and 1 mM 2,6-DMP. The Breslmayr assay was performed by adding a master mix containing the above reagents to 1 µM of *Ma*LPMO10B WT or mutants. All the reactions had a final volume of 100 µL and the master mix was created to a volume corresponding with the number of reactions. 2 µL of the desired 50 µM protein solution was added to each well and mixed with 20 µL ddH$_2$O to avoid evaporation during the 5-minute incubation time prior to starting the assay. The master mix was added to separate wells in the 96-well plate so it could also be warmed in the incubation step. After the 5-minute incubation at 30 °C, 78 µL of master mix was added to the wells containing enzyme and ddH$_2$O using a multichannel pipette. A plate reader was used to measure the formation of coerulignone at 473 nm every 10 seconds for 300 seconds.

3.3.6 Redox Potential Measurements

LPMOs need an electron transfer to reduce Cu(II) to Cu(I) in order to initiate the oxidative cleavage of recalcitrant substrates as described in Section 1.4.4. The redox potential reflects the LPMO's ability to accept electrons. N,N,N',N'-tetramethyl-1,4-phenylenediamine (TMP) in its reduced form can be used as an electron transfer mediator to determine the cell potential of the LPMO-Cu^{2+}/LPMO-Cu^{1+} redox couple (Aachmann *et al.*, 2012). Equation 2 shows the redox reaction between TMP and an LPMO.

$$\mathrm{TMP_{red}} + \text{LPMO-Cu}^{2+} \leftrightharpoons \mathrm{TMP_{ox}} + \text{LPMO-Cu}^{1+} \qquad (2)$$

The equilibrium constant of equation 2 can be determined as oxidized TMP has an absorbance which can be measured at 610 nm and the concentration of TMP$_{\mathrm{ox}}$ equals the concentration of LPMO-Cu^{1+} at reaction equilibrium. The equilibrium constant of the reaction is displayed in equation 3. The Beer-Lambert law is used to find the concentration of TMP$_{\mathrm{ox}}$ (and therefore LPMO-Cu^{1+}) at equilibrium using the extinction coefficient of TMP determined to be 14.0 mM^{-1} cm^{-1} (Sorlie *et al.*, 2000). The concentration of TMP$_{\mathrm{red}}$ and LPMO-Cu^{2+} is known.

$$K = \frac{[\mathrm{TMP_{ox}}][\text{LPMO-Cu}^{1+}]}{[\mathrm{TMP_{red}}][\text{LPMO-Cu}^{2+}]} \qquad (3)$$

The cell potential of the reaction shown in equation 2 is determined by equation 4.

$$\Delta G_r^o = -RT\ln K = -nFE^o \qquad (4)$$

Equation 4 shows that the free energy change (ΔG_r^o) is dependent on the temperature in kelvin (T) and the equilibrium constant (K), or the number of electron transfers in the reaction (n) and the cell potential of the reaction (E^o). R represents the gas constant and F represents the Faraday constant. Once the cell potential of the reaction is calculated, the cell potential of the LPMO-Cu^{2+}/LPMO-Cu^{1+} redox couple can be determined using equation 5.

$$E_{cell}^o = E_{cathode}^o - E_{anode}^o \qquad (5)$$

E^o_{cell} is the cell potential of the redox reaction between TMP and an LPMO (equation 2) and E^o_{anode} is the cell potential of TMP, previously determined to be 273 mV (Liu *et al.*, 1997). Adding E^o_{anode} to the cell potential of the reaction (E^o_{cell}) will determine $E^o_{cathode}$, the cell potential of the LPMO-Cu^{2+}/LPMO-Cu^{1+} redox couple. The measurement of cell potential is performed under anaerobic conditions as TMP is sensitive to oxidation in contact with molecular oxygen.

Materials:

- Airtight glass bottles with rubber stopper lids
- HPLC vials and stoppered lids (VWR)
- *Ma*LPMO10B WT and mutants (70 µM) (Section 3.2.7)
- mgLPMO10 (50 µM) (provided by Kelsi Hall)
- NanoPhotometer® C4 spectrophotometer (Implen)
- PIPES buffer pH 6 (200 mM)
- Schlenk system for nitrogen flushing
- *Sc*LPMO10C (70 µM) (provided by Kelsi Hall)
- Sodium phosphate buffer pH 6 (200 mM)
- TMP_{red} powder (Merck)
- TraceSELECT® water (Honeywell)
- Whitley A95 TG anaerobic workstation (Don Whitley Scientific)

Method:

The buffers and TraceSELECT® water were transferred to airtight bottles and nitrogen flushed for 30 minutes. The TMP_{red} powder, buffer, and TraceSELECT® water were placed in the anaerobic chamber one day prior to measurement. *Ma*LPMO10B WT was exchanged into 20 mM piperazine-N,N'-bis(2-ethanesufonic acid) (PIPES) buffer pH 6, as described in Section 3.2.7, to compare results with PIPES and sodium phosphate buffer pH 6. The amount of protein needed to create a 70 µM solution for three replicates was transferred to an HPLC vial with stoppered lids and carefully nitrogen flushed for 5 minutes. In the anaerobic chamber, the buffers were diluted to 20 mM and a 300 µM TMP_{red} solution was created by dissolving the TMP_{red} powder in 20 mM anaerobic buffer.

The samples were mixed directly in cuvettes and consisted of 30 µL of LPMO-Cu^{2+} and 30 µL of TMP_{red} with final concentrations of 35 µM and 150 µM, respectively. A blank was also created to determine the baseline absorbance at 610 nm and contained buffer instead of protein. Once the samples were created, the reaction was monitored at 610 nm until it reached equilibrium. The absorbance of TMP_{ox} when the reaction had reached equilibrium was measured at 610 nm with a portable NanoPhotometer® C4 spectrophotometer. The redox potential was calculated from the absorbance measurement as described above.

4 Results

4.1 Cloning

4.1.1 Constructing *Ma*LPMO10B Mutant Plasmids

Plasmids containing the YQR, FQH, and YEH single mutants and the FEH double mutant were generated by whole-plasmid PCR amplification (Section 3.1.2). Specific forward and reverse primers for each mutant were used to introduce the desired mutations while simultaneously amplifying the entire plasmid. Amplification of the entire plasmid was verified by agarose gel electrophoresis, showing a band size around 3800 bp (expected size of 3847 bp) in the positive control for each mutant (Figure 10A). In addition, the negative control did not show any bands for either of the mutants. For the remaining YER, FQR, $\mathrm{FER}_{\mathrm{res}}$, and $\mathrm{FER}_{\mathrm{loop}}$ mutants, the pRSETB backbone with the CBM and linker region of *Ma*LPMO10B was amplified. The pRSETB backbone was then assembled with the ordered gene fragments containing the desired mutations (Table 7) by site-directed mutagenesis using DNA assembly (Section 3.1.6). The PCR product from amplification of the pRSETB backbone with linker region and the CBM showed a band at approximately 3200 bp which corresponded with the expected size of 3199 bp (Figure 10B).

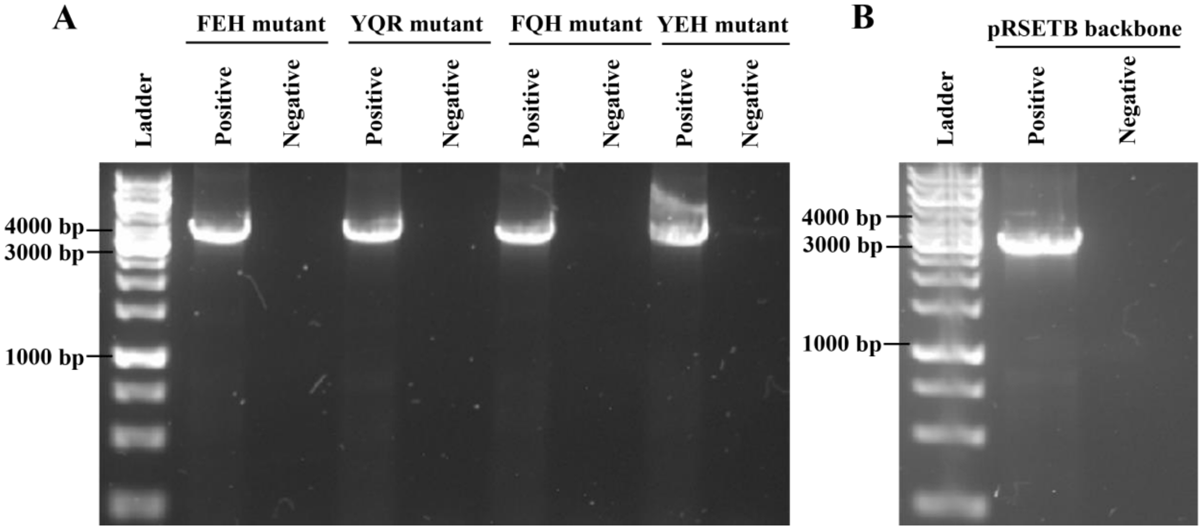

Figure 10. Agarose gel electrophoresis image of whole-plasmid PCR amplified MaLPMO10B mutants and PCR amplified pRSETB backbone. *(A) Bands indicating successful whole-plasmid PCR amplification of the mutants FEH, YQR, FQH, and YEH. (B) Band indicating successful amplification of the pRSETB backbone. The ladder is shown on the left side in both images and 1000 bp, 3000 bp, and 4000 bp are labelled. All samples had a positive control which included a plasmid template and a negative control without template.*

4.1.2 Transformation and Sequence Verification of *Ma*LPMO10B Mutants

The DNA assembly reactions (Section 3.1.6) and the whole-plasmid PCR products (Section 3.1.2) were transformed into *E. coli* TOP10 cells. Selected colonies were screened by PCR to verify that a plasmid with a gene size corresponding to the size of *Ma*LPMO10B was taken up by the cells. The pRSETB_insert forward and reverse primers were used for the PCR screening because they annealed to the beginning of the *Ma*LPMO10B gene and at the end of the CBM, respectively. The PCR screen could only verify if a plasmid with the correct gene size of *Ma*LPMO10B had been taken up and not if the specific mutations had been introduced.

Figure 11 shows the PCR product of the screened colonies from transformation of all mutants into *E. coli* TOP10. At least one colony screened for each mutant (Figure 11) displayed a band at around 1200 bp, corresponding to the size of *Ma*LPMO10B (1140 bp). The PCR screen of the transformed colonies containing the single mutants (YQR, FQH, and YEH) and one double mutant (FEH), cloned using whole-plasmid PCR, showed a 100 % success rate (Figure 11A and B). However, the PCR of the transformed colonies from the YER and FQR double mutants, and the $\mathrm{FER_{res}}$ and $\mathrm{FER_{loop}}$ triple mutants, cloned using DNA assembly, was successful for only approximately half of the colonies screened (Figure 11C).

In the colonies with non-successful transformation, a band appeared at approximately 500 bp (Figure 11C). This indicated that error occurred during DNA assembly and plasmids containing smaller gene inserts were generated. The error may have been avoided by designing a gene fragment with more base pairs in the overhang for more specific homologous recombination. In addition, some wells displayed less prominent bands of the wrong size (250 bp) (Figure 11C). This is likely due to non-specific binding of the primers to the DNA during the PCR screen. A higher primer annealing temperature could have been used during the PCR screen to avoid this.

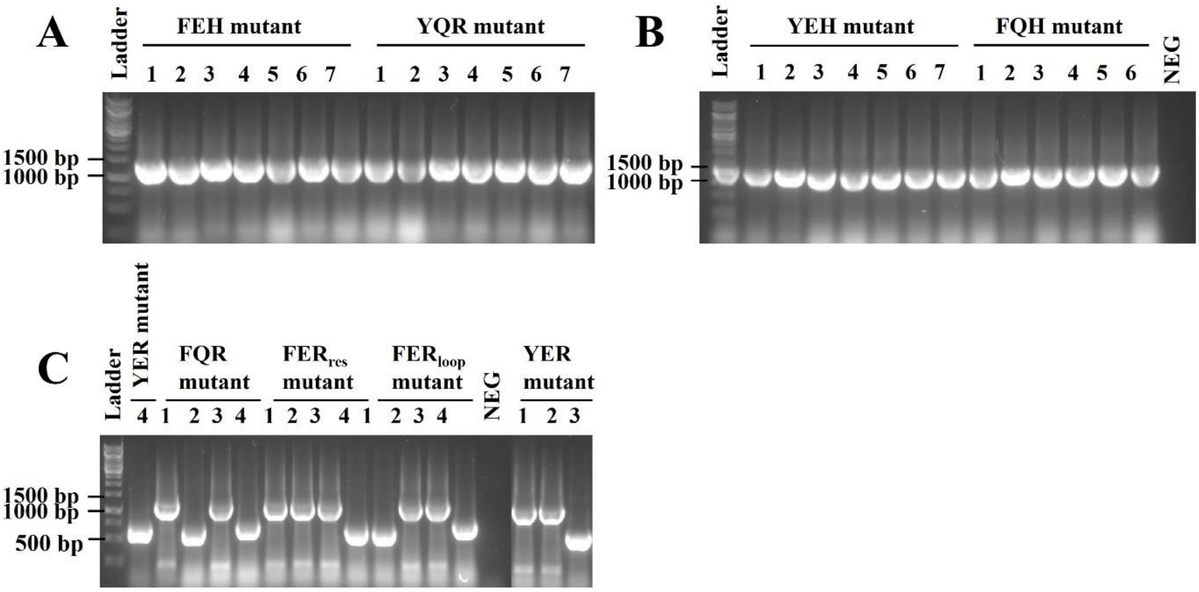

Figure 11. PCR screen of MaLPMO10B mutants transformed into E. coli TOP10. *(A) PCR screen for the FEH double mutant and YQR single mutant transformed into E. coli TOP10. (B) PCR screen for the YEH and FQH single mutants transformed into E. coli TOP10. (C) PCR screen for the FQR and YER double mutants, and the FER$_{res}$ and FER$_{loop}$ triple mutants transformed into E. coli TOP10. All images display the ladder on the left side where 1000 bp and 1500 bp are labelled. In addition, 500 bp is labelled in (C). The negative control (NEG) contains the reaction mix without a colony sample.*

The second sphere residues of *Ma*LPMO10B (tyrosine, glutamine, and alanine at position 221, 219, and 214, respectively) were mutated to phenylalanine, glutamate, and arginine, respectively, by using two different techniques of site-directed mutagenesis. To verify that the desired mutations were introduced, two or three transformed colonies containing the correct insert size for each mutant were cultivated, purified, and sent for sequencing. Figure 12 shows the sequence alignment of the mutants against *Ma*LPMO10B WT. For all the single mutants, the FEH double mutant, and the FER$_{loop}$ triple mutant, the sequencing analysis clearly showed that the correct nucleotides had been mutated, with no insertions or deletions. The loop region of mgLPMO10 was introduced into the *Ma*LPMO10B FER$_{loop}$ mutant (Figure 8). Therefore, this mutant contained additional mutations (H216D, L217S, and D218Q). The *Ma*LPMO10B mutants with an alanine to arginine mutation at position 214 also had an additional histidine to glycine mutation at position 216 to allow space to introduce the arginine residue of interest, as previously explained (Section 1.6).

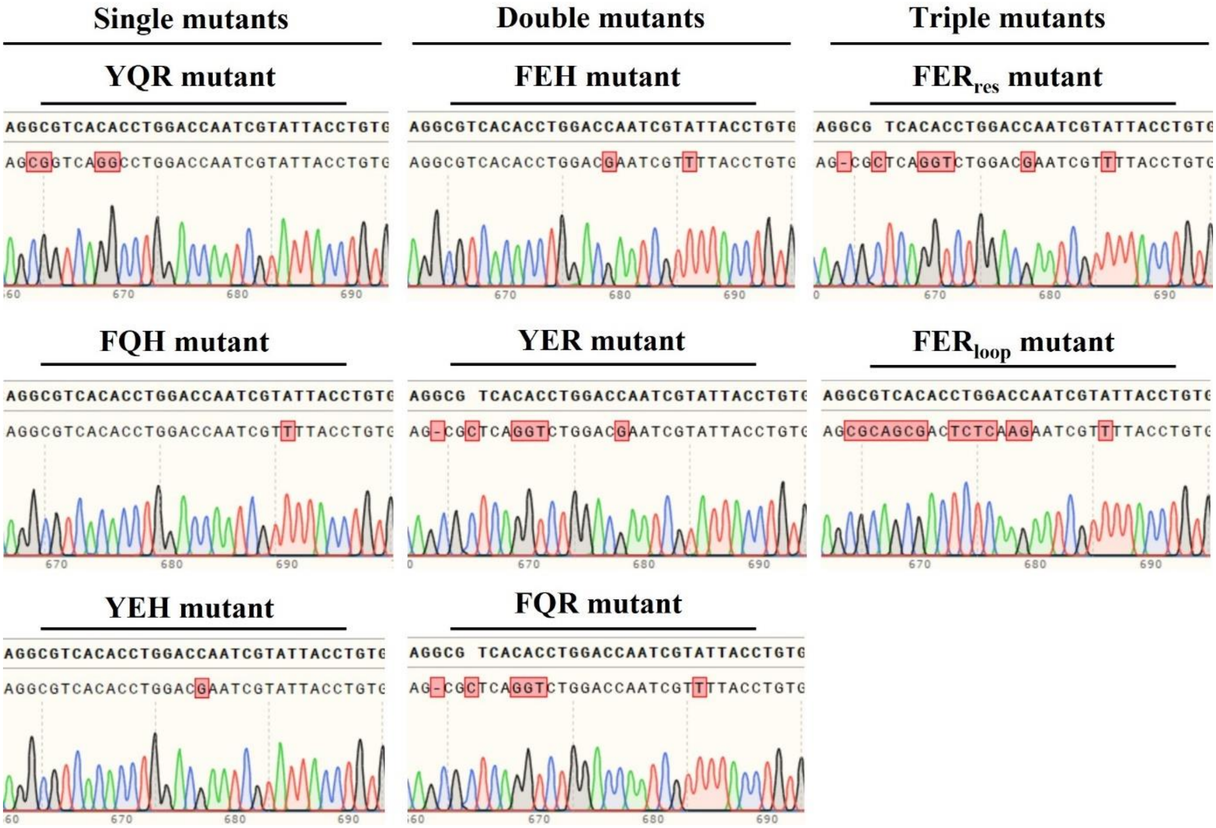

Figure 12. Sequence alignment of the MaLPMO10B mutant plasmids. *Sequence alignment of the YQR, FQH, YEH, FEH, YER, FQR, FER$_{res}$, and FER$_{loop}$ mutants (black letters) against MaLPMO10B WT (bold black letters). The chromatogram indicates where adenine (green), cytosine (blue), thymine (red), or guanine (black) nucleotides were detected. Nucleotides highlighted in red indicates that a mutation have occurred. The numbers at the bottom of each chromatogram indicate the nucleotide position in the gene. Sequence alignment was performed using SnapGene.*

The double mutants YER and FQR, and the triple mutant FER$_{res}$, displayed one deletion and one insertion upon sequence alignment with *Ma*LPMO10B WT in SnapGene (Figure 12). These deletions and insertions are artifacts from the SnapGene software which commonly occurs when aligning a sequence which contains multiple consecutive mutations. The order of the nucleotides (CGCTCA) in the area where the deletion and insertion appeared correlates with the order of nucleotides expected for the alanine to arginine mutation. We thus considered that the site-directed mutagenesis was successful.

The sequence verified plasmids were transformed into *E. coli* BL21 (DE3). Errors in the plasmid normally occur during the cloning steps, and a PCR screen to verify successful transformation into *E. coli* BL21 (DE3) is usually not necessary. This is because the plasmid used to transform the *E. coli* BL21 (DE3) cells originated from one single *E. coli* TOP10 cell containing the correct plasmid, unlike the plasmids in the PCR products (Section 3.1.2) and

DNA assembly reactions (Section 3.1.6) which contained a mixture of truncated and correct plasmids (Section 3.1.7). However, the *E. coli* BL21 (DE3) transformed colonies appeared unhealthy compared with the *E. coli* TOP10 transformed colonies. Therefore, up to seven *E. coli* BL21 (DE3) transformed colonies were PCR screened to confirm the presence of a correct sized gene (Figure A 1).

4.2 Protein Expression and Purification

4.2.1 Purification of *Ma*LPMO10B WT and Mutants

Expression cultures of *Ma*LPMO10B WT and the mutants were prepared in TB media supplemented with 100 µg/mL ampicillin, then incubated at 30 and 37 °C, respectively. Initially, the *Ma*LPMO10B mutants were grown at 30 °C, but due to low yield (Table 15), expression cultures were prepared at 37 °C. Expression appeared to be higher at 37 °C, and the sucrose fractions showed a lower yield than the periplasmic extract (Figure A 2). We thus decided to grow all mutants at 37 °C for all subsequent purifications.

After periplasmic extract of the protein, *Ma*LPMO10B was first purified with anion exchange chromatography as described in Section 3.2.3. Figure 13A shows an example chromatogram from anion exchange chromatography of *Ma*LPMO10B WT. *Ma*LPMO10B WT and the mutants did not bind to the column and eluted in the flow-through (Forsberg *et al.*, 2018). The chromatogram therefore shows the UV signal obtained during the binding of the periplasmic extract to the column. *Ma*LPMO10B WT eluted after approximately 12 mL (2 to 3 column volumes) which was confirmed by analysis of the collected fractions on an SDS-PAGE gel (Figure 13B). The flow-through collected from approximately 12 to 42 mL (2 to 8 column volumes and fraction 4 to fraction 10) showed a band at approximately 35 kDa in the SDS-PAGE analysis, corresponding to the size of *Ma*LPMO10B WT of 34.9 kDa (Figure 13B). We observed similar behavior during anion exchange chromatography of the *Ma*LPMO10B mutants, and the chromatograms and SDS-PAGE gel analysis of the mutants are shown in Figure A 3, Figure A 4, Figure A 5, Figure A 6, and Figure A 7.

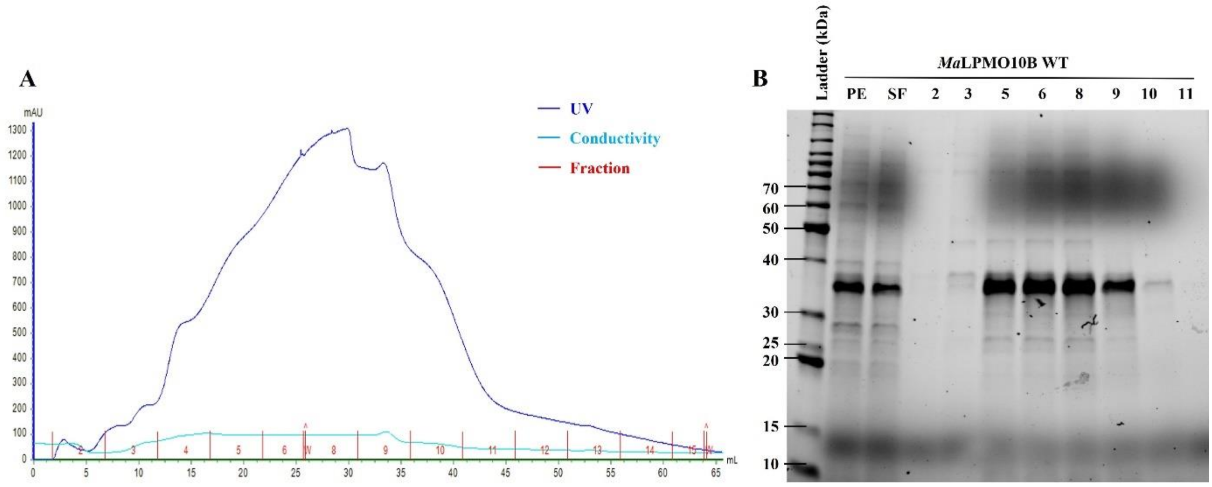

Figure 13. Anion exchange chromatography of MaLPMO10B WT. (A) A representative example of anion exchange chromatography of MaLPMO10B WT showing the UV signal obtained during binding of the periplasmic extract to the column. The Y-axis displays the UV absorbance (mAU) and the X-axis shows the volume of eluent used in mL. The UV trace line (dark blue) indicates protein eluting from the column. The light blue trace line displays the conductivity over the column and the red lines show the collected fractions. (B) SDS-PAGE analysis of the fractions collected during anion exchange chromatography, and the periplasmic extract (PE) and sucrose fraction (SF) collected during periplasmic extract of the protein. The ladder is located on the left, showing protein size in kDa. The numbers at the top of each well in (B) corresponds to the fractions (red) in (A).

Figure 13B showed that the protein fractions that included *Ma*LPMO10B WT also included other contaminating proteins, displayed as fainter bands (e.g., at approximately 25 and 45 kDa). Purification with SEC was therefore necessary to remove the other proteins. The fractions containing *Ma*LPMO10B WT were pooled and copper saturated (Section 3.2.6). The solution was then equilibrated to 50 mM Tris-HCl pH 7.5 and simultaneously concentrated down to 1 mL.

The resulting chromatogram from SEC of *Ma*LPMO10B WT shows that elution of *Ma*LPMO10B WT began after 58 mL (approximately 0.5 column volumes) (Figure 14A). The collected fractions were analyzed by SDS-PAGE (Figure 14B). The fractions collected between 58 and 73 mL (approximately 0.5 and 0.6 column volumes and fraction 9 to fraction 13) displayed a band at approximately 35 kDa, corresponding to the size of *Ma*LPMO10B WT (34.9 kDa) (Figure 14B). These fractions were pooled and equilibrated to the storage buffer (20 mM sodium phosphate buffer pH 6). The results from purification of the *Ma*LPMO10B mutant proteins are comparable to the results shown for the *Ma*LPMO10B WT. The chromatograms from SEC and the SDS-PAGE analysis for the mutants are shown in Figure A 8, Figure A 9, Figure A 10, and Figure A 11.

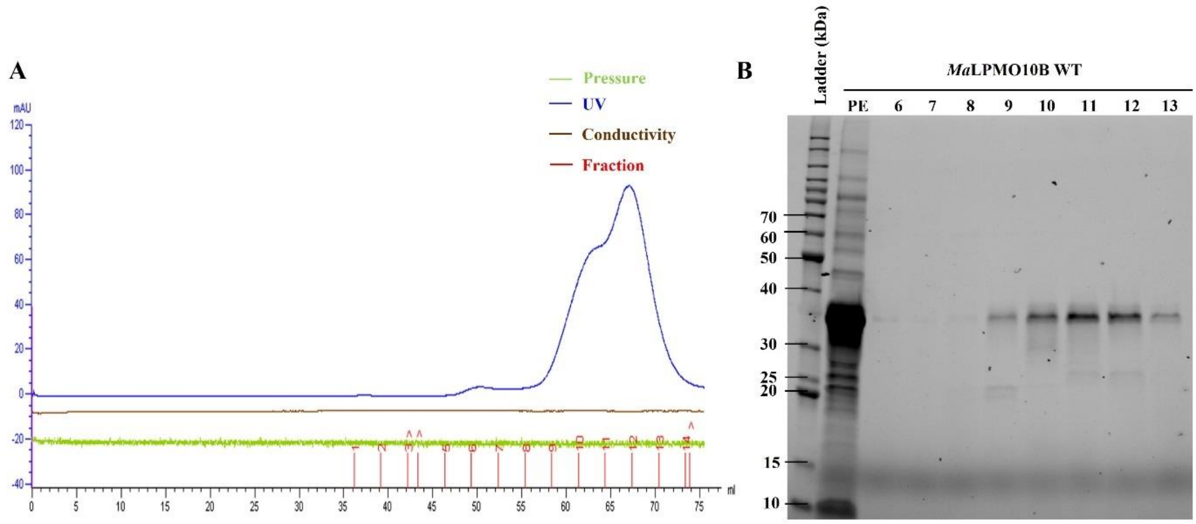

Figure 14. Size exclusion chromatography of MaLPMO10B WT. *(A) A representative example of SEC performed on MaLPMO10B WT. The Y-axis shows the UV absorbance (mAU) and the X-axis shows the volume of eluent in mL used during elution of the protein. The UV trace line (blue) indicates protein eluting from the column. The brown line represents the conductivity over the column, while the green line displays the pressure over the column. The red lines show the fractions that were collected. (B) SDS-PAGE analysis of the fractions collected during SEC of MaLPMO10B WT and the periplasmic extract (PE). The ladder is displayed on the left side and shows protein size in kDa. The numbers on the top correspond to the fractions (red) in (A).*

4.2.2 Final Protein Yield and Quality

The absorbance at 280 nm for each purified protein, and the respective extinction coefficient and molecular weight (Table 14) was used to determine the protein yield. The protein yield (mg) per 500 mL culture for each purification is shown in Table 15. *Ma*LPMO10B WT was purified three times and yielded of 1.35, 1.21, and 1.14 mg, respectively. These three yields were higher than any yield obtained for the mutants.

All the mutated residues in the *Ma*LPMO10B variants were located at the active site of the *Ma*LPMO10B protein and changing amino acids at the active site could yield unstable proteins. We were therefore fortunate that all the *Ma*LPMO10B mutants were soluble and could be purified. The highest yield obtained among the mutants were 0.60, 0.53, and 0.50 mg for the YQR, YEH, and FER_{res} mutants, respectively. The FER_{loop} mutant obtained the lowest yield in all purifications (0.02, 0.11, and 0.10 mg). However, this is not unexpected since the FER_{loop} mutant has six mutations in total and was likely more unstable than *Ma*LPMO10B WT and the other mutants.

*Table 15. Purification yield table of MaLPMO10B WT and the mutants. The protein yield in mg is shown per 500 mL of cell culture. The purifications performed at 30 °C are labelled with * and the purifications performed at 37 °C are not labelled.*

	Amino acid code	**Yield (mg) per 500 mL of culture**		
Purification		**1**	**2**	**3**
WT	YQH	1.35*	1.21*	1.14*
Single mutants	YQR	0.10*	0.60	
	FQH	0.15*	0.04	0.24
	YEH	0.03*	0.39	0.53
Double mutants	FEH	0.06*	0.31	
	YER	0.02*	0.48	
	FQR	0.08*	0.31	
Triple mutants	FER_{res}	0.50		
	FER_{loop}	0.02	0.11	0.10

The yields obtained here were much lower than expected, even for *Ma*LPMO10B WT. Normally, a minimum yield of 2 mg for *Ma*LPMO10B WT is expected, but low expression is currently an on-going problem in our group (Z. Forsberg, pers. com., 2022). We think this may be due to change in media manufacturing or the ddH_2O used. However, two to three purifications yielded enough protein to perform the characterization assays in this thesis. Again, it was remarkable that all the *Ma*LPMO10B mutants could be purified, despite these on-going expression issues.

The purity of the purified *Ma*LPMO10B WT and mutants is presented in Figure 15. All *Ma*LPMO10B proteins showed a strong band at approximately 35 kDa, corresponding to the size of the *Ma*LPMO10B protein (34.9 kDa) (Table 14). *Ma*LPMO10B WT and the YQR, YEH, FQH, YER, FQR, and FER_{res} mutants displayed a lower proportion of other contaminating proteins than the FEH and FER_{loop} mutants. The FEH mutant had a prominent band at 70 kDa which was not as prominent in *Ma*LPMO10B WT or the other mutants. The FER_{loop} mutant contained more contaminating proteins than the other *Ma*LPMO10B variants, as a distinct band at approximately 26 kDa was shown along with several less prominent bands ranging from 10 to 35 kDa. A negative control without reductant was included in all assays to detect any activity not dependent on a reductant. We could then ensure that the observed activity was truly from the *Ma*LPMO10B WT and mutants.

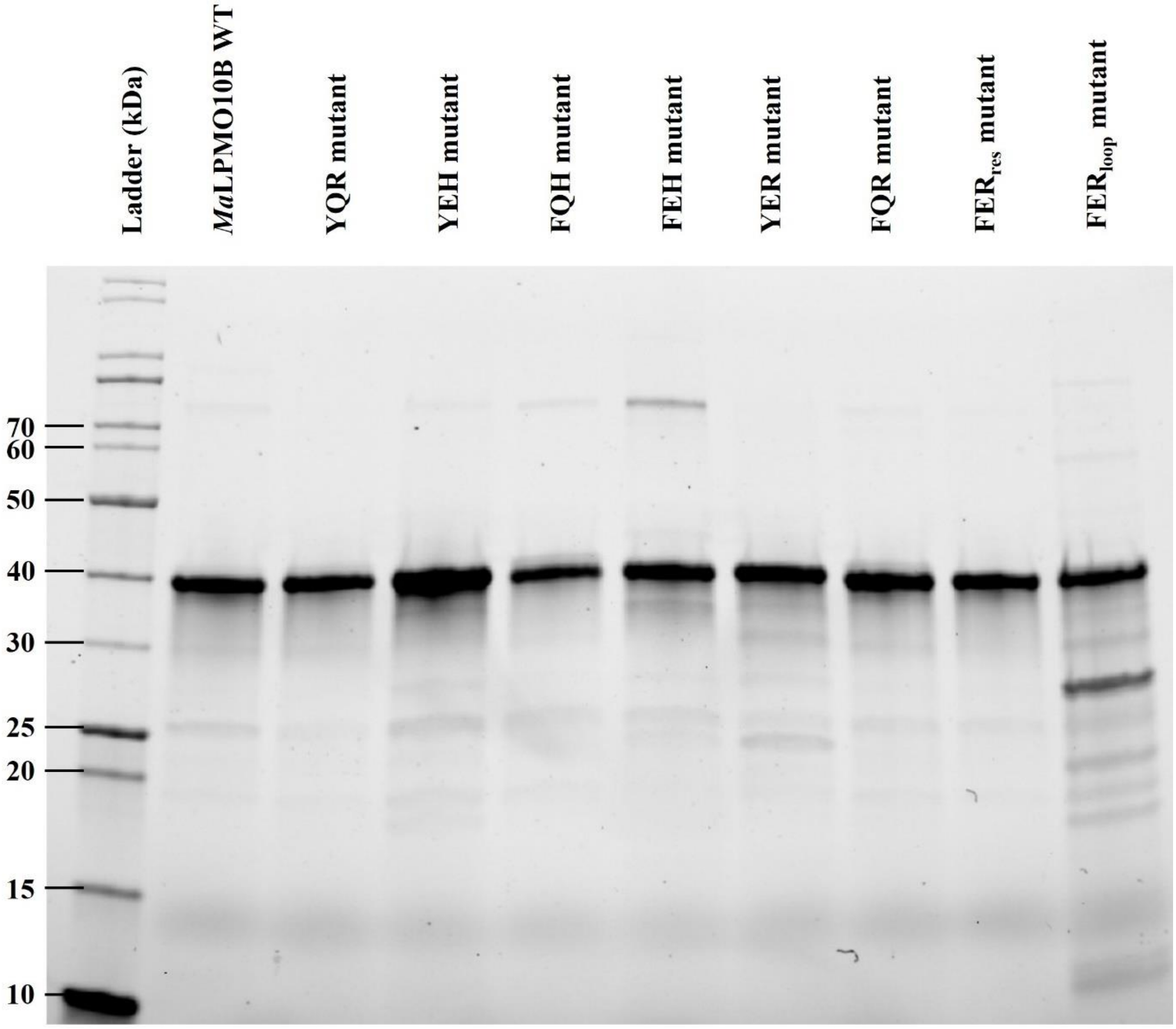

Figure 15. SDS-PAGE gel of purified MaLPMO10B WT and the mutants. *The protein ladder is displayed on the left side showing the sizes of each band from 10 to 70 kDa. 1 µg of each protein was applied to the gel and each well is labelled with the respective protein.*

4.3 Characterization of *Ma*LPMO10B WT and Mutants

4.3.1 Analysis of C1- and C4-Oxidized Cello-Oligosaccharides

The ability of *Ma*LPMO10B WT and the mutants to oxidatively cleave PASC was monitored by measuring C1- and C4-oxidized cello-oligosaccharides. *Ma*LPMO10B WT and the mutants were incubated with 0.1% w/v PASC and 1 mM ascorbic acid in 50 mM sodium phosphate buffer pH 6. A sample was taken after 24 hours and then incubated with *Tf*Cel6A to break down larger products to DP2 and DP3 cello-oligosaccharides. The samples were analyzed by HPAEC-PAD using the 50-minute method (described in Section 3.3.2) and standard curves for DP2 and DP3 C1-oxidized cello-oligosaccharides (Figure A 12) and DP2 and DP3 C4-oxidized cello-oligosaccharides were generated (Figure A 13). This was an initial experiment to observe whether *Ma*LPMO10B WT and the mutants were active on PASC, which is why only one sample was collected after 24 hours.

Figure 16 shows the C1-oxidized product concentration (µM) after 24 hours generated by *Ma*LPMO10B WT and the mutants. *Ma*LPMO10B WT produced 206 ± 12 µM of C1-oxidized cello-oligosaccharides. This was approximately 3.3 times more than the YEH mutant (62 ± 6 µM) which displayed the highest C1-oxidized product formation among the mutants. High activity was also observed for the FQH (44 ± 2 µM) and FEH (19 ± 0.4 µM) mutant. The YQR single mutant and the YER double mutant displayed low activity towards C1-oxidation, albeit not as low as the triple mutants and the FQR double mutant. Even though C1-activity was low for five of the mutants, peaks in the chromatograms were evident above the background noise, indicating true activity.

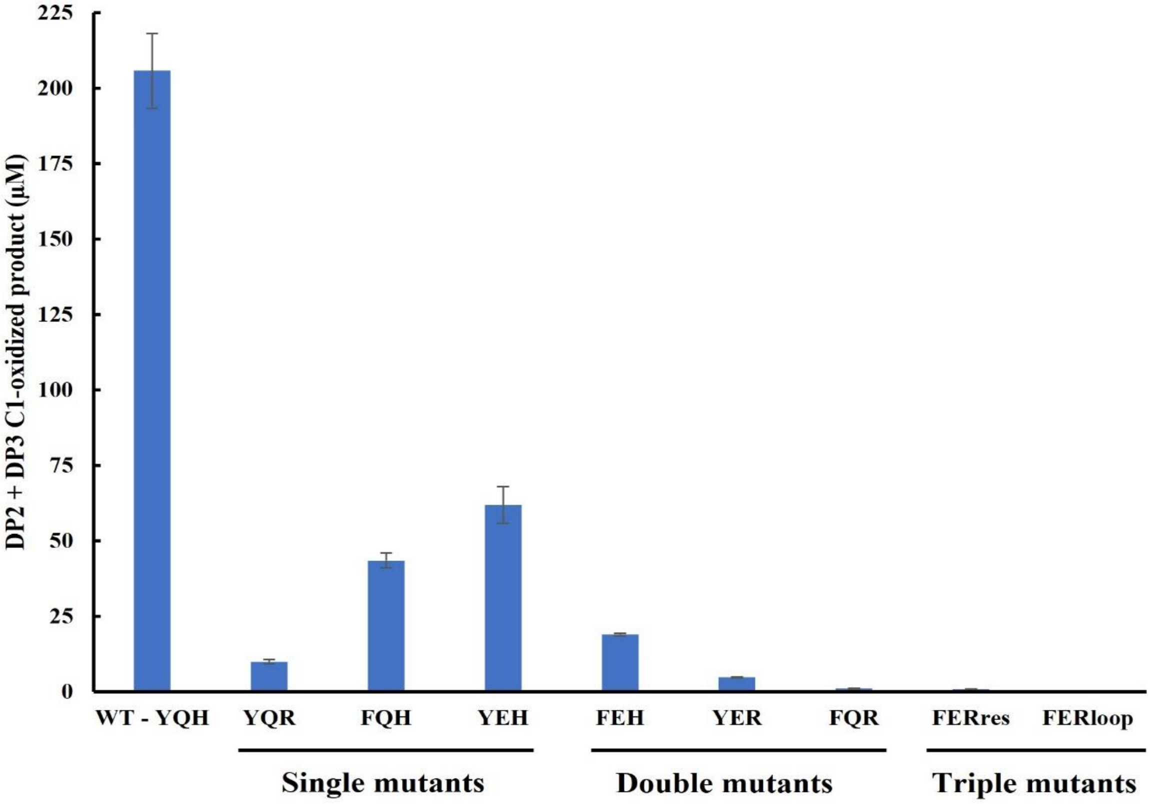

Figure 16. C1-oxidized product formation for MaLPMO10B WT and the mutants after incubation for 24 hours. *The Y-axis shows the C1-oxidized product concentration in µM generated by each protein after incubation at 40 °C and 1000 rpm for 24 hours. 1 µM of LPMO was incubated with 0.1 % w/v of PASC and 1 mM ascorbic acid in 50 mM sodium phosphate buffer pH 6. The reactions were incubated with TfCel6A prior to analysis. The error bars indicate the standard deviation between three independent replicates.*

*Ma*LPMO10B WT exhibited more C4-oxidized activity than the mutants, as was also evident for C1-oxidized activity (Figure 17). *Ma*LPMO10B WT had a concentration of C4-oxidized cello-oligosaccharides of 42 ± 3 µM. All the mutants except YQR displayed activity towards C4-oxidation, although the C4-activity of the FEH mutant was extremely low (0.5 ± 0.03 µM). The FQH mutant showed the highest activity towards C4-oxidation among the mutants (6 ± 0.2 µM). The YER mutant produced 3 ± 0.3 µM of C4-oxidized cello-oligosaccharides, while the remaining YEH, FQR, FER$_{res}$, and FER$_{loop}$ mutants had a product concentration below 1.5 µM. Overall, *Ma*LPMO10B WT and most mutants appeared to favor C1-oxidation over C4-oxdiation.

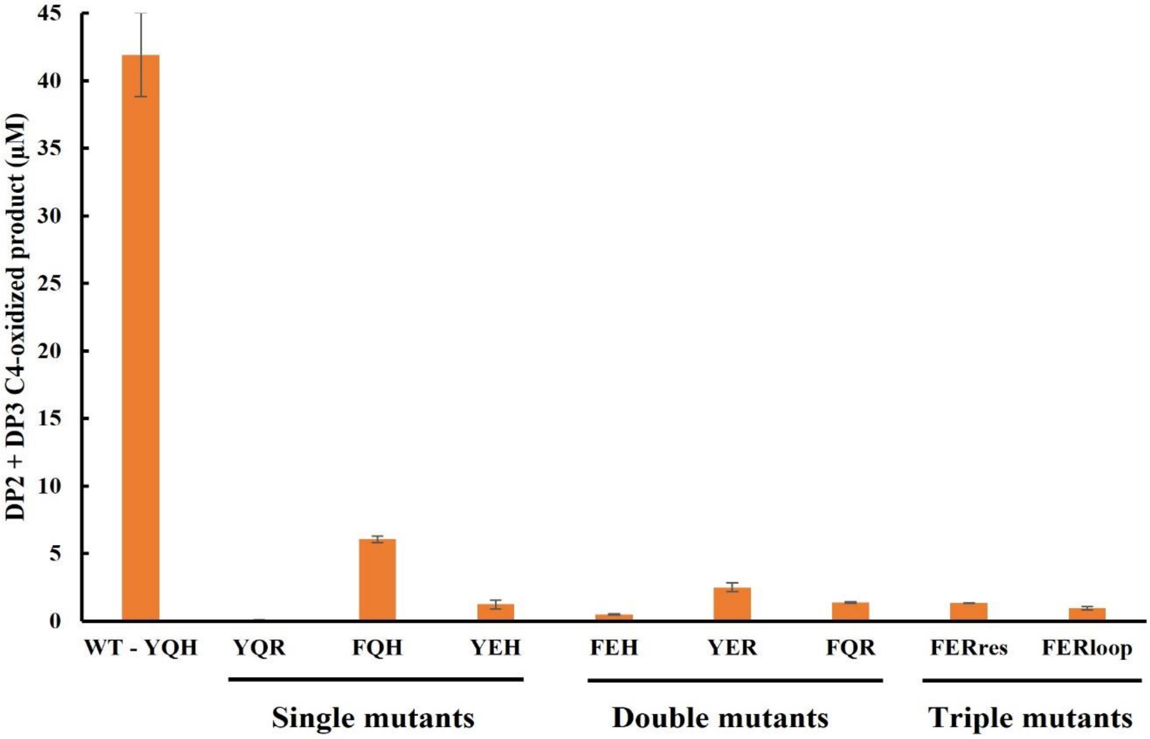

Figure 17. C4-oxidized product formation after incubation for 24 hours for MaLPMO10B WT and the mutants. *1 µM of LPMO was incubated with 0.1 % w/v of PASC and 1 mM ascorbic acid in 50 mM sodium phosphate buffer pH 6 at 40 °C and 1000 rpm for 24 hours. The reactions were treated with TfCel6A prior to analysis. The Y-axis shows the concentration of C4-oxidized cello-oligosaccharides and the error bars indicate the standard deviation between three independent replicates.*

4.3.2 The Ratio between C1- and C4-Oxidized Cello-Oligosaccharides

Figure 18 shows that C1-oxdiation of PASC was favored by *Ma*LPMO10B WT, the single mutants YQR, FQH, and YEH, and by the FEH double mutant as C1-oxidized product made up over 80 % of the total product concentration. The YER mutant also favored C1-oxidation where over 60 % of the total product concentration originated from C1-oxidized product (Figure 18). The two triple mutants, FER$_{res}$ and FER$_{loop}$, and the FQR double mutant preferentially produced C4-oxidized product (Figure 18). It is worth noting that the C1-oxidized product concentration was very low for some of the mutants, especially for FER$_{loop}$, FER$_{res}$, and FQR mutants, along with minimal C4-product concentration for the YQR and FEH mutants. This meant that small changes in product concentration could alter the ratio substantially. Since C1-oxidized products were the predominant product produced by the majority of the *Ma*LPMO10B proteins, and the method used to simultaneously analyze both C1- and C4-oxidized cello-oligosaccharides is time consuming, only C1-oxidized cello-oligosaccharides were analyzed in the following experiments.

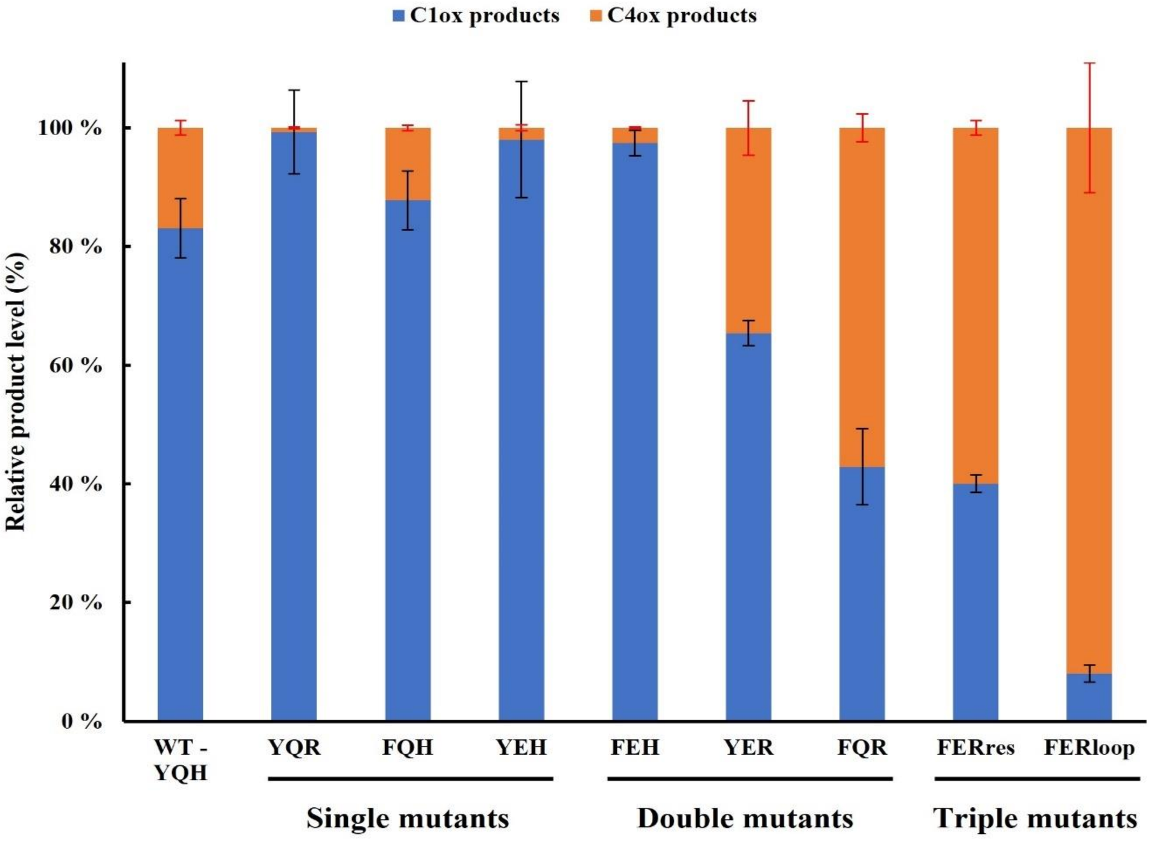

Figure 18. The C1 to C4 ratio of oxidized cello-oligosaccharides for MaLPMO10B WT and the mutants. The Y-axis shows the relative product level (%) of C1- and C4-oxidized cello-oligosaccharides for MaLPMO10B WT and the mutants. C4-oxidized product is indicated in orange and C1-oxidized product is indicated in blue. Black error bars represent the standard deviation of the C1-oxidized products, while the red error bars represent the standard deviation for the C4-oxidized products. Three independent repeats were performed for each condition. The conditions were the same as described for Figure 16 and Figure 17.

4.3.3 Activity towards β-Chitin

The activity towards β-chitin for *Ma*LPMO10B WT and the mutants was established by analysis of oxidized chito-oligosaccharides with DP2 (A2ox). The reaction contained 1 µM of LPMO, 1 % w/v β-chitin, and 1 mM ascorbic acid in 50 mM sodium phosphate buffer pH 6 and was incubated at 40 °C and 1000 rpm for 24 hours. Samples were collected after 1 hour and 24 hours and all the reactions were then treated with *Sm*CHB prior to analysis with UHPLC

(Section 3.3.3). A standard curve for A2ox was generated for quantification of A2ox product (Figure A 14). Product concentration was only shown for the 24-hour time point, as coelution of reduced ascorbic acid with A2ox was apparent after 1 hour.

The concentration of A2ox generated by *Ma*LPMO10B WT and the mutants after 24 hours is shown in Figure 19. Significant activity towards β-chitin was observed for *Ma*LPMO10B WT and the YEH mutant. Interestingly, the YEH mutant generated twice the amount of A2ox (157 ± 49 µM) compared with *Ma*LPMO10B WT (69 ± 4 µM). The YER mutant produced the third most product (19 ± 0.2 µM). The *Ma*LPMO10B YQR, FQH, FEH, FQR, FER_{res}, and FER_{loop} mutants displayed activity towards β-chitin, albeit at very low levels.

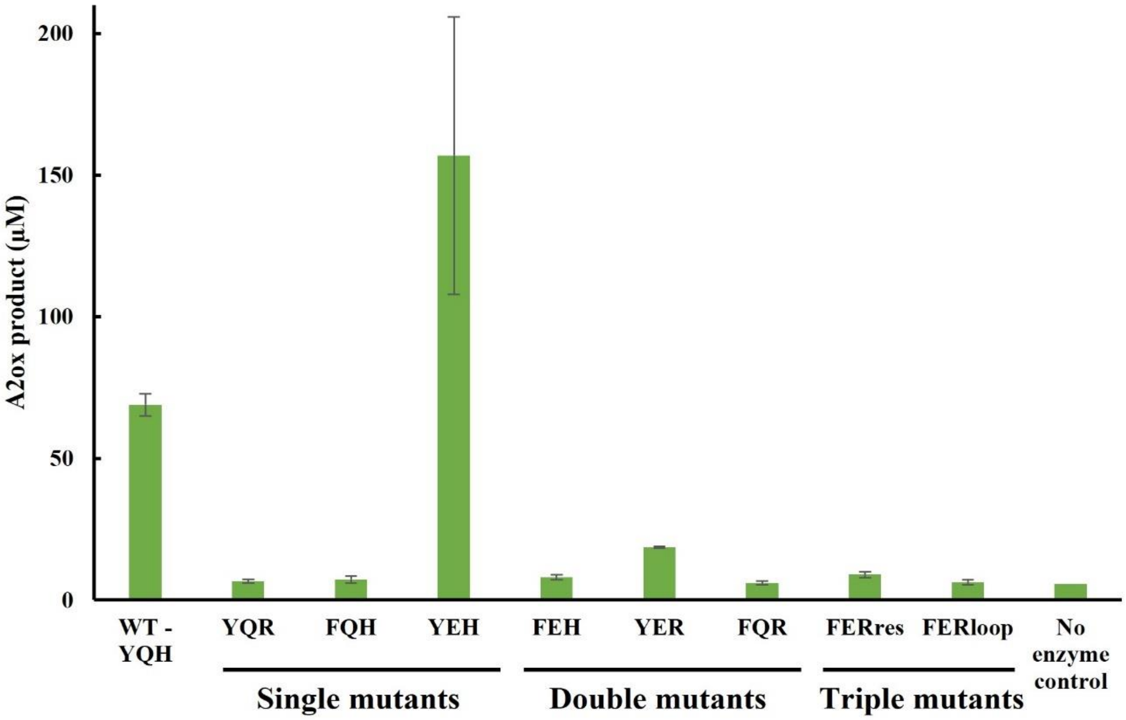

Figure 19. A2ox product formation from β-chitin for MaLPMO10B WT and the mutants. *The Y-axis shows the concentration of A2ox product in µM released after incubation of the LPMO at 40 °C and 1000 rpm for 24 hours. 1 µM of LPMO was incubated with 1 % w/v β-chitin and 1 mM ascorbic acid in 50 mM sodium phosphate buffer pH 6. The error bars display the standard deviation between three independent replicates.*

4.3.4 Analysis of C1-Oxidized Products in O_2-driven Reactions

The reaction conditions in this experiment were identical to the reaction conditions described in Section 4.3.1, but samples were taken at 15 and 30 minutes, and 1, 2, 4, 8, and 24 hours. These samples were analyzed by using the 26-minute method (described in Section 3.3.2) and only C1-oxidized cello-oligosaccharides were quantified. This experiment was performed to observe how the reactions changed over time and at which rate C1-oxidized cello-oligosaccharides were produced.

The reaction with *Ma*LPMO10B WT did not reach completion and generated 228 ± 27 µM C1-oxidized product during the reaction time of 24 hours (Figure 20A). The highest activity among the *Ma*LPMO10B mutants was observed for the YEH mutant. Interestingly, the YEH mutant displayed an initial rate of approximately 0.7 µM/s, almost seven times faster than the initial rate of *Ma*LPMO10B WT (0.1 µM/s). However, the YEH mutant appeared to inactivate after 4 hours as the final product concentration was lower than for *Ma*LPMO10B WT (Figure 20B, top). The single mutants, YQR and FQH, generated cello-oligosaccharides throughout the reaction time of 24 hours, although at a substantially slower rate (Figure 20B, top). A slow initial rate was also observed for the FEH double mutant (0.02 µM/s), but the reaction plateaued after 8 hours (Figure 20B, middle). The FQR and the YER double mutants displayed a fast initial rate (Figure 20B, middle). However, these mutants generated low amounts of product and were inactivated after only 15 minutes (Figure 20B, middle). An accurate initial rate could therefore not be determined. The FER_{res} and FER_{loop} mutants displayed little C1-activity towards PASC, as previously observed in Section 4.3.1 (Figure 20, bottom).

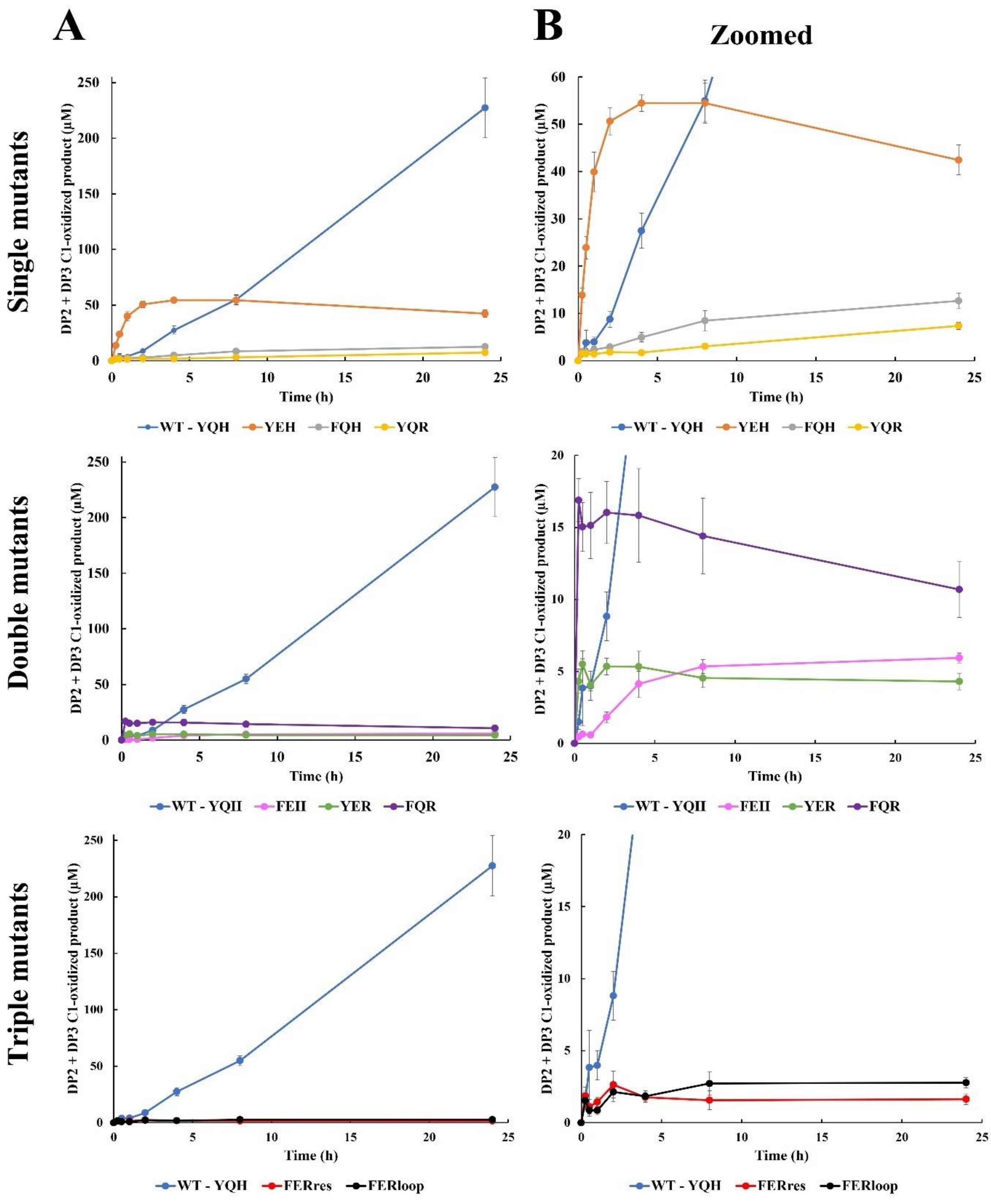

Figure 20. ***Production of C1-oxidized cello-oligosaccharides over 24 hours for MaLPMO10B WT and the mutants in reactions driven by molecular oxygen.*** *(A) Production of oxidized cello-oligosaccharides over time for the single mutants (top); YEH (orange), FQH (grey), and YQR (yellow), the double mutants (middle); FEH (pink), YER (green), and FQR (purple), and the triple mutants (bottom); FER$_{res}$ (red) and FER$_{loop}$ (black). (B) Zoomed in versions of the figures in (A). The Y-axis shows the concentration of C1-oxidized products (µM) and the X-axis shows the time (h). MaLPMO10B WT (blue) is displayed in all plots. 1 µM of LPMO was incubated with 0.1 % w/v PASC and 1 mM ascorbic acid in 50 mM sodium phosphate buffer pH 6 at 40 °C and 1000 rpm for 24 hours. All samples were treated with TfCel6A prior to analysis. The time points (15 and 30 minutes, and 1, 2, 4, 8, and 24 hours) are displayed as dots. The error bars represent the standard deviation between three independent replicates at each time point.*

4.3.5 Oxidase Activity of *Ma*LPMO10B WT and Mutants, mgLPMO10, and *Sc*LPMO10C

The oxidase activity is an LPMO's ability to produce hydrogen peroxide using molecular oxygen and a reductant. Hydrogen peroxide drives the reaction where glycosidic bonds of recalcitrant polysaccharides are oxidatively cleaved by the LPMO. Therefore, the rate at which the LPMO's intrinsically produce hydrogen peroxide were measured. The initial hydrogen peroxide production rates were obtained by mixing 2 µM of LPMO with 100 µM amplex red, 5 U/mL HRP, and 1 mM ascorbic acid in 50 mM sodium phosphate buffer pH 6. A hydrogen peroxide standard curve was generated to calculate the initial hydrogen peroxide production rates (Figure A 15). The UV signal of resorufin molecules were measured as described in Section 3.3.4. Figure 21 shows the initial rate obtained for *Ma*LPMO10B WT, *Ma*LPMO10B mutants, mgLPMO10, *Sc*LPMO10C, a free copper positive control, and a no enzyme negative control. *Sc*LPMO10C and mgLPMO10 were included in these measurements because FER residues occur as their natural second sphere residues. Their ability produce hydrogen peroxide was therefore of interest.

*Ma*LPMO10B WT had an initial hydrogen peroxide production rate (0.02 ± 0.0002 µM/s) similar to the initial rate of mgLPMO10 (0.02 ± 0.002 µM/s) (Figure 21B). The YEH mutant had the highest initial rate of all the proteins in this assay (0.1 ± 0.02 µM/s) and was approximately five times faster than the *Ma*LPMO10B WT (Figure 21B). The initial hydrogen peroxide production of the YER mutant (0.03 ± 0.003 µM/s) was also 1.5 times faster than *Ma*LPMO10B WT.

The YQR and FQH single mutants and the FEH and FQR double mutants displayed a low initial rate of hydrogen peroxide production. Interestingly, the two triple mutants, FER_{res} (0.007 ± 0.0003 µM/s) and FER_{loop} (0.009 ± 0.0005 µM/s), displayed a faster initial hydrogen peroxide production rate than the YQR, FQH, FEH, and FQR mutants. *Sc*LPMO10C also had a low initial hydrogen peroxide production rate (0.003 ± 0.0003 µM/s). The free copper positive control had a high initial hydrogen peroxide production rate indicating that the assay worked properly (Figure 21A). The no enzyme control displayed minimal activity and was measured because ascorbic acid can be involved in side-reactions where small amounts of hydrogen peroxide is produced. All the *Ma*LPMO10B mutants displayed a higher initial rate than the no enzyme control, indicating true activity.

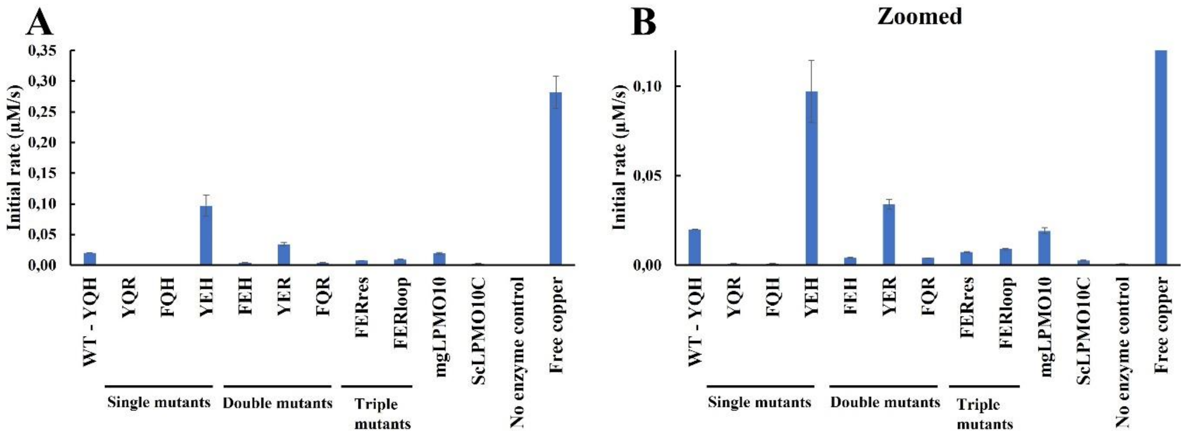

Figure 21. Oxidase activity of MaLPMO10B WT, MaLPMO10B mutants, mgLPMO10, and ScLPMO10C. *(A) Initial hydrogen peroxide production for MaLPMO10B WT, MaLPMO10B mutants, mgLPMO10, and ScLPMO10C. (B) Zoomed in version of (A). Initial hydrogen peroxide production rate is shown on the Y-axis in µM/s. The reaction mixtures contained 2 µM of LPMO (or* $CuSO_4$*), 100 µM amplex red, 5 U/mL HRP, and 1 mM ascorbic acid in 50 mM sodium phosphate buffer pH 6. The error bars indicate the standard deviation of three independent replicates for each reaction. The initial rates were divided by two to obtain the initial rate per 1 µM of protein.*

4.3.6 Analysis of C1-Oxidized Products using Hydrogen Peroxide as Co-Substrate

LPMOs are able to use hydrogen peroxide as a co-substrate in a reaction to oxidatively cleave recalcitrant polysaccharides, such as cellulose or chitin (Bissaro *et al.*, 2017). The ability of *Ma*LPMO10B WT and the mutants to oxidatively cleave PASC in the presence of supplemented hydrogen peroxide was monitored. 1 µM of LPMO was incubated with 0.1 % w/v PASC, 100 µM H_2O_2, and 10 µM ascorbic acid in 50 mM sodium phosphate buffer pH 6 at 40 °C and 1000 rpm for 30 minutes (1800 seconds). Figure 22 shows the concentration of C1-oxidized cello-oligosaccharides produced by *Ma*LPMO10B WT and the mutants over a 30-minute period with samples collected at 30 seconds and 1, 5, 10, and 30 minutes.

The estimated initial rate for *Ma*LPMO10B WT was 0.2 µM/s (Figure 22A). All the *Ma*LPMO10B mutants exhibited slower initial rates than *Ma*LPMO10B WT, with the YEH mutant among the slowest (0.002 µM/s). All the *Ma*LPMO10B mutants also generated less than one tenth of the C1-oxidized cello-oligosaccharide concentration compared to *Ma*LPMO10B WT. The highest product concentration among the mutants was observed for the YER mutant (2 ± 0.5 µM) (Figure 22B, middle). This suggests that the enzymes were inactivating before the reaction had reached completion. The YER, FQH, and YQR mutants appeared to inactivate after approximately 300 seconds, while the YQR and the YEH single mutants, and the FEH double mutant appeared to inactivate after 600 seconds (Figure 22B). The triple mutants generated less than 0.5 µM of C1-oxidized cello-oligosaccharides with slow initial rates.

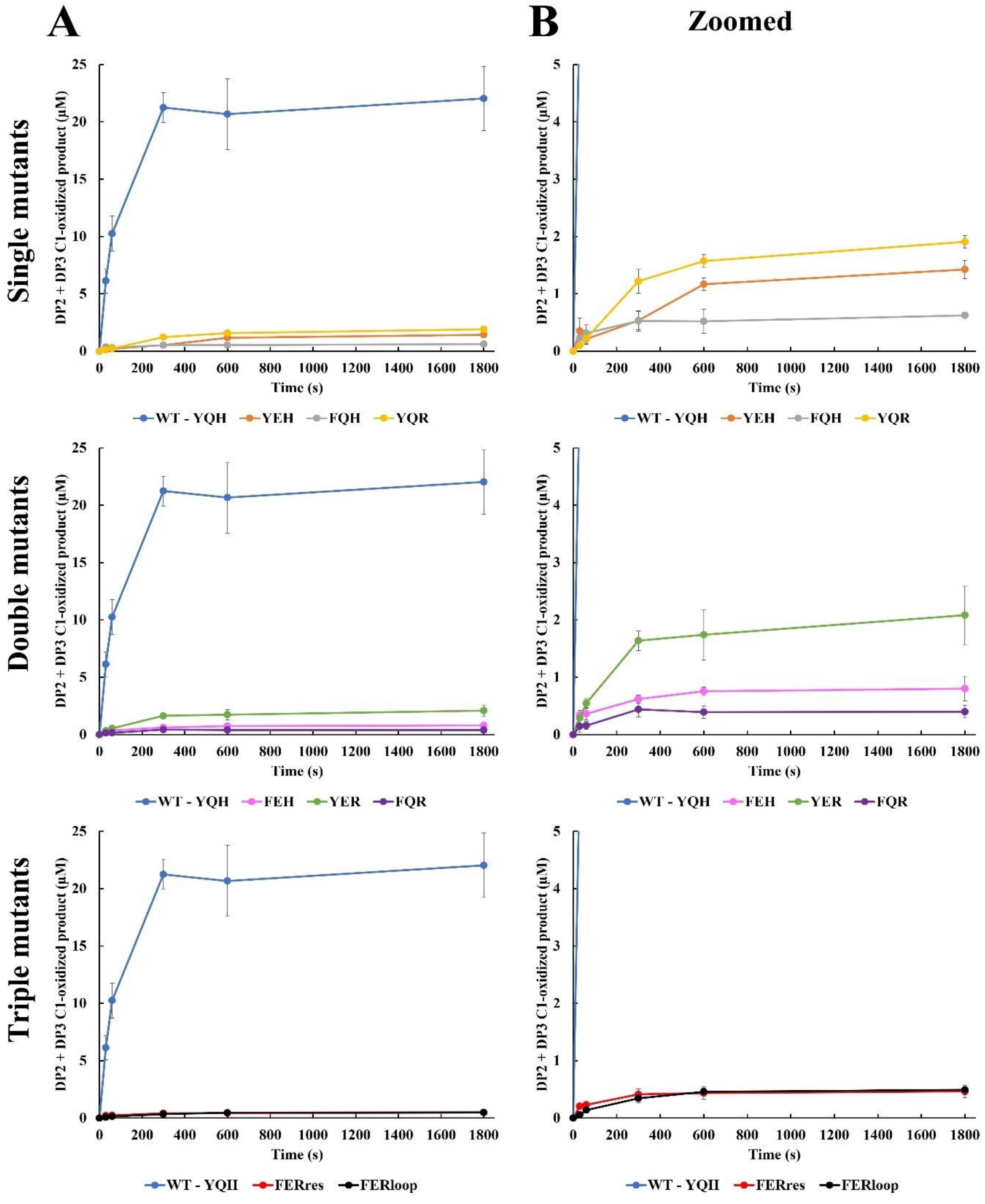

__Figure 22. Production of C1-oxidized cello-oligosaccharides over time for MaLPMO10B WT and the mutants in reactions supplemented with hydrogen peroxide.__ (A) Production of oxidized cello-oligosaccharides over time for the single mutants (top); YEH (orange), FQH (grey), and YQR (yellow), the double mutants (middle); FEH (pink), YER (green), and FQR (purple), and the triple mutants (bottom); FER$_{res}$ (red) and FER$_{loop}$ (black). (B) Zoomed in versions of the figures in (A). The Y-axis shows the concentration of C1-oxidized products (µM) and the X-axis shows the time (s). MaLPMO10B WT (blue) is displayed in all plots. 1 µM of LPMO was incubated with 0.1 % w/v PASC, 100 µM H_2O_2, and 10 µM ascorbic acid in 50 mM sodium phosphate buffer pH 6 for 30 minutes at 40 °C and 1000 rpm. All samples were treated with TfCel6A prior to analysis. The time points (30 seconds, and 1, 5, 10, and 30 minutes) are displayed as dots. The error bars indicate the standard deviation between three independent replicates at each time point.

It was unexpected that only 21 ± 1 µM of C1-oxidized cello-oligosaccharides were produced in the reaction performed by *Ma*LPMO10B WT when 100 µM of hydrogen peroxide was supplemented (Figure 22A). If hydrogen peroxide was completely converted, 100 µM of oxidized product should have been generated. The reaction performed by *Ma*LPMO10B WT stopped after only 10 minutes and we assumed that something was causing the reaction to plateau prematurely. A hydrogen peroxide-driven reaction with identical reaction conditions as explained in the beginning of this Section was used in this experiment. 100 µM H_2O_2 or 1 mM ascorbic acid and/or 1 µM of *Ma*LPMO10B WT was added to the reaction after 11 minutes in an attempt to reinitiate the reaction and to determine why the reaction was plateauing prematurely. Addition of ascorbic acid or LPMO (Figure 23A) or addition of hydrogen peroxide (Figure 23B) did not reinitiate the reaction. In contrast, more C1-oxidized cello-oligosaccharides were generated after addition of both ascorbic acid and fresh *Ma*LPMO10B WT (Figure 23B). This indicated that both the ascorbic acid was depleted and that *Ma*LPMO10B WT was inactivated after 10 minutes.

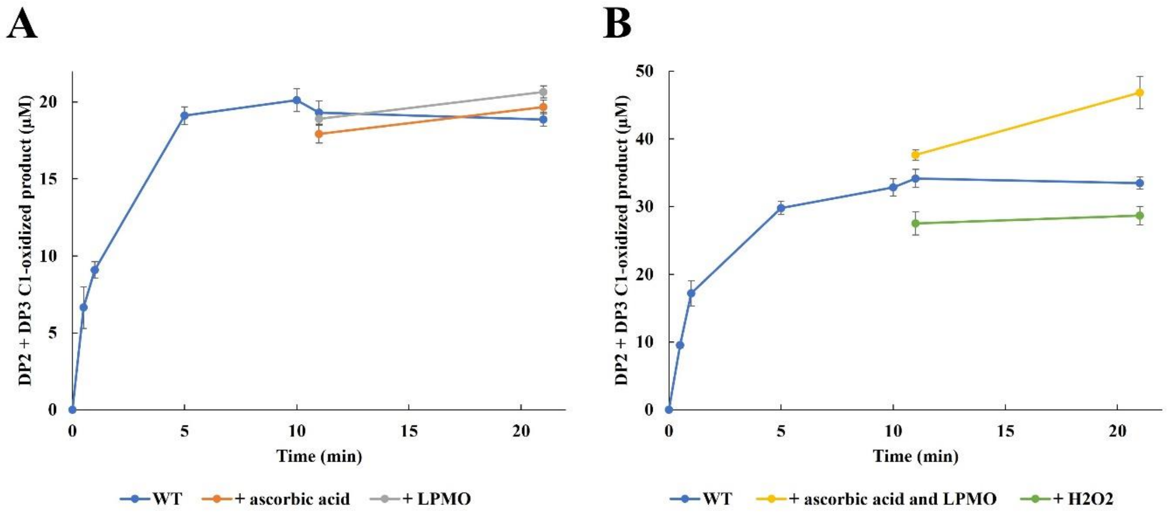

Figure 23. Production of C1-oxidized cello-oligosaccharides over time for MaLPMO10B WT in reactions supplemented with hydrogen peroxide with addition of hydrogen peroxide, ascorbic acid, and MaLPMO10B WT. *(A) Production of C1-oxidized products (Y-axis, µM) over time (X-axis, min) for MaLPMO10B WT (blue) with addition of 10 µM ascorbic acid (orange) or 1 µM LPMO (grey) after 11 minutes. (B) Production of C1-oxidized products (Y-axis, µM) over time (X-axis, min) for MaLPMO10B WT (blue) with addition of 10 µM ascorbic acid and 1 µM LPMO (yellow) or 100 µM* H_2O_2 *(green). Both reactions contained 1 µM of MaLPMO10B WT incubated with 100 µM* H_2O_2*, 10 µM ascorbic acid, and 0.1 % w/v PASC in 50 mM sodium phosphate buffer pH 6. After 10 minutes, the reactions were split in three separate tubes where one tube remained unchanged and different combinations of ascorbic acid, LPMO, and hydrogen peroxide were added to the other tubes. Samples were taken at 30 seconds, and 1, 5, 10, 11, and 21 minutes and are represented as dots. The error bars indicate the standard deviation between three independent replicates at each time point.*

4.3.7 Peroxidase Activity of *Ma*LPMO10B WT and Mutants

The peroxidase activity is the LPMOs ability to utilize hydrogen peroxide. In this assay, we assessed how well the LPMOs could turnover hydrogen peroxide when 2,6-DMP was used as both substrate and reductant. The reactions contained 1 µM LPMO, 100 µM H_2O_2, and 1 mM 2,6-DMP in 50 mM sodium phosphate buffer pH 6.

*Ma*LPMO10B WT oxidized 2,6-DMP with a rate of 0.0002 ± 0.00001 A_{473}/s, while the *Ma*LPMO10B mutants displayed minimal activity towards 2,6-DMP compared with *Ma*LPMO10B WT (Figure 24). The highest initial rate among the *Ma*LPMO10B mutants was observed for the YER mutant (0.00003 ± 0.000003 A_{473}/s) (Figure 24). The FER_{res} triple mutant also displayed higher activity towards 2,6-DMP compared with the remaining mutants (Figure 24). The remaining *Ma*LPMO10B mutants (YQR, FQH, YEH, FEH, and FER_{loop}) had an initial rate lower than 0.00002 A_{473}/s, suggesting that hydrogen peroxide turnover was low when 2,6-DMP was used as substrate and reductant.

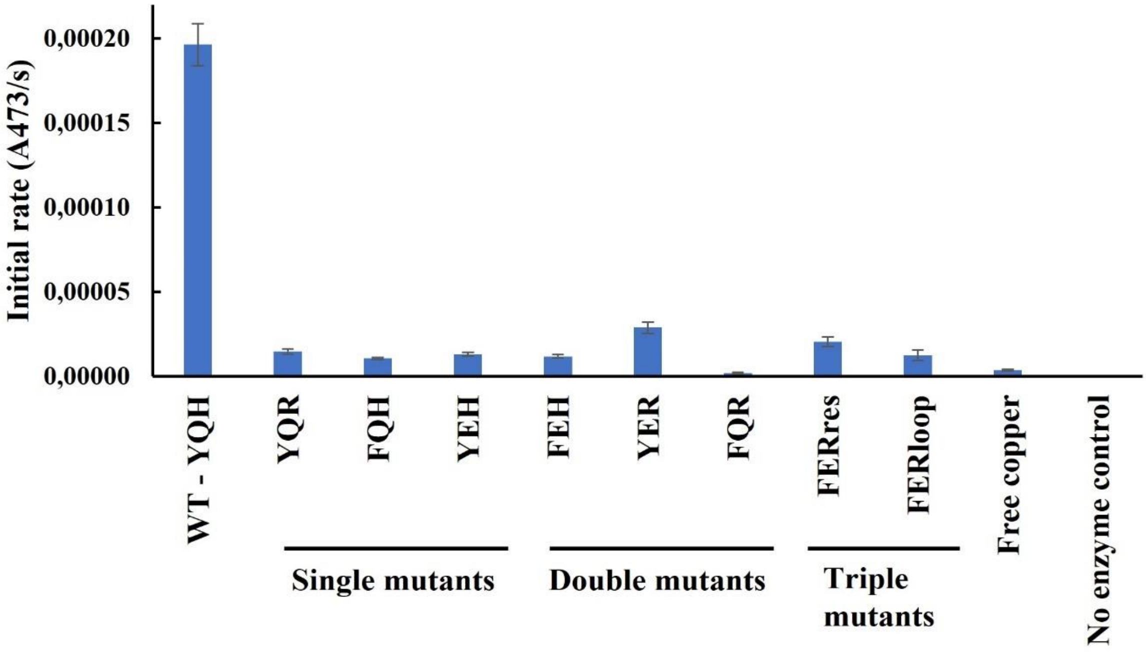

Figure 24. Peroxidase activity of MaLPMO10B WT and the mutants. *Initial coerulignone production rate (which indirectly shows hydrogen peroxide consumption) is shown on the Y-axis in* A_{473}*/s for MaLPMO10B WT and the mutants. All the reactions contained 1 µM of LPMO (or* $CuSO_4$*, except the control without enzyme), 100 µM* H_2O_2*, and 1 mM 2,6-DMP in 50 mM sodium phosphate buffer pH 6. The error bars indicate the standard deviation of three independent replicates.*

4.3.8 Enzyme Kinetics – Redox potential

The redox potential of the LPMO-Cu^{2+}/LPMO-Cu^{1+} redox couple for *Ma*LPMO10B WT, the *Ma*LPMO10B mutants, mgLPMO10, and *Sc*LPMO10C was determined as described in Section

3.3.6. 150 µM TMP$_{red}$ and 35 µM LPMO-Cu^{2+} was mixed in a cuvette and once the reaction reached equilibrium, the absorbance of TMP$_{ox}$ was measured at 610 nm.

4.3.8.1 Redox Potential of MaLPMO10B WT in PIPES and Sodium Phosphate Buffer

Standard practice in our laboratory group is to measure the redox potential using PIPES buffer, but due to the low yield obtained for the *Ma*LPMO10B mutants (Table 15) it was desired to measure the proteins in their storage buffer (20 mM sodium phosphate buffer pH 6). This is because some protein was likely to be lost during an exchange into another buffer. It was therefore tested whether the redox potential of *Ma*LPMO10B WT was comparable in PIPES buffer pH 6 *versus* sodium phosphate buffer pH 6. The redox potential of three replicates of *Ma*LPMO10B WT in 20 mM PIPES buffer pH 6 was determined to be 196 ± 5 mV, while the redox potential of three replicates of *Ma*LPMO10B WT in 20 mM sodium phosphate buffer pH 6 was determined to be 192 ± 14 mV. It was concluded that the redox potential in PIPES and sodium phosphate buffer was comparable and that the redox potential of the *Ma*LPMO10B mutants could be measured in 20 mM sodium phosphate buffer pH 6.

4.3.8.2 Redox Potential of MaLPMO10B WT and Mutants, mgLPMO10, and ScLPMO10C

The redox potential of *Ma*LPMO10B WT, the *Ma*LPMO10B mutants, mgLPMO10, and *Sc*LPMO10C were measured with the same TMP$_{red}$ solution, prepared on the same day to avoid differences due to batch variation. *Ma*LPMO10B WT had the highest redox potential of 244 ± 7 mV, followed by the YER mutant (228 ± 19 mV) (Table 16). It is worth noting that the difference in redox potential determined in this Section and in Section 4.3.8.1 for *Ma*LPMO10B WT was most likely due to that different stocks of TMP$_{red}$ and different enzyme batches were used. The lowest redox potential was determined for the FQR double mutant (134 ± 9 mV). The YQR and FQH single mutants, and the FEH double mutant displayed redox potentials between 161 and 175 mV. The two triple mutants, FER$_{res}$ (209 ± 16 mV) and FER$_{loop}$ (191 ± 0 mV), and the YEH single mutant (194 ± 5 mV) had a comparable ability to accept electrons. Due to low yield (Table 15), only two replicates of the FER$_{loop}$ mutant were measured. These replicates showed the exact same absorbance, resulting in a standard deviation of zero. *Sc*LPMO10C and mgLPMO10 had comparable redox potentials of 214 ± 19 mV and 191 ± 31 mV, respectively.

Table 16. The redox potential of MaLPMO10B WT, the MaLPMO10B mutants, mgLPMO10, and ScLPMO10C. The redox potential of MaLPMO10B WT, the MaLPMO10B mutants, mgLPMO10, ScLPMO10C and free copper is shown in mV with the standard deviation obtained between three replicates, and the relative standard deviation (%). The FER$_{loop}$ mutant shows the standard deviation between two replicates due to low yield during purification. The redox potential was determined by measuring the absorbance of TMP$_{ox}$ at 610 nm in a reaction between 35 µM of LPMO-Cu^{2+} and 150 µM of TMP$_{red}$. The cell potential of the reaction was then calculated to determine the redox potential using the equations shown in Section 3.3.6.

	Amino acid code	**Redox potential (mV)**	**STD**	**RSTD (%)**
WT	YQH	244	7	3.0
Single mutants	YQR	169	3	1.7
	FQH	175	9	4.9
	YEH	194	5	2.5
Double mutants	FEH	161	6	4.0
	YER	228	19	8.5
	FQR	134	9	7.1
Triple mutants	FER$_{res}$	209	16	7.5
	FER$_{loop}$	191	0	0.0
***Sc*LPMO10C**	FER	214	19	8.7
mgLPMO10	FER	191	31	16.5
	Free copper	213	8	3.8

4.3.8.3 Correlation between Redox Potential and Oxidase Activity

A regression and a correlation analysis were performed to see if there was a correlation between the LPMO's ability to produce hydrogen peroxide (oxidase activity) and the ability to accept electrons (redox potential). The regression analysis was performed with a level of significance of 0.05 and yielded a p-value of 0.01. Since the p-value was lower than the level of significance, the variation in redox potential could be explained by the oxidase activity for *Sc*LPMO10C, mgLPMO10, *Ma*LPMO10B WT and the mutants, except for the YEH mutant (Figure 25). The correlation analysis showed a strong positive correlation (r = 0.75) between *Sc*LPMO10C, mgLPMO10, *Ma*LPMO10B WT and the mutants, except for the YEH mutant. The YEH mutant appeared to be an outlier and was therefore not included in the regression or correlation analysis.

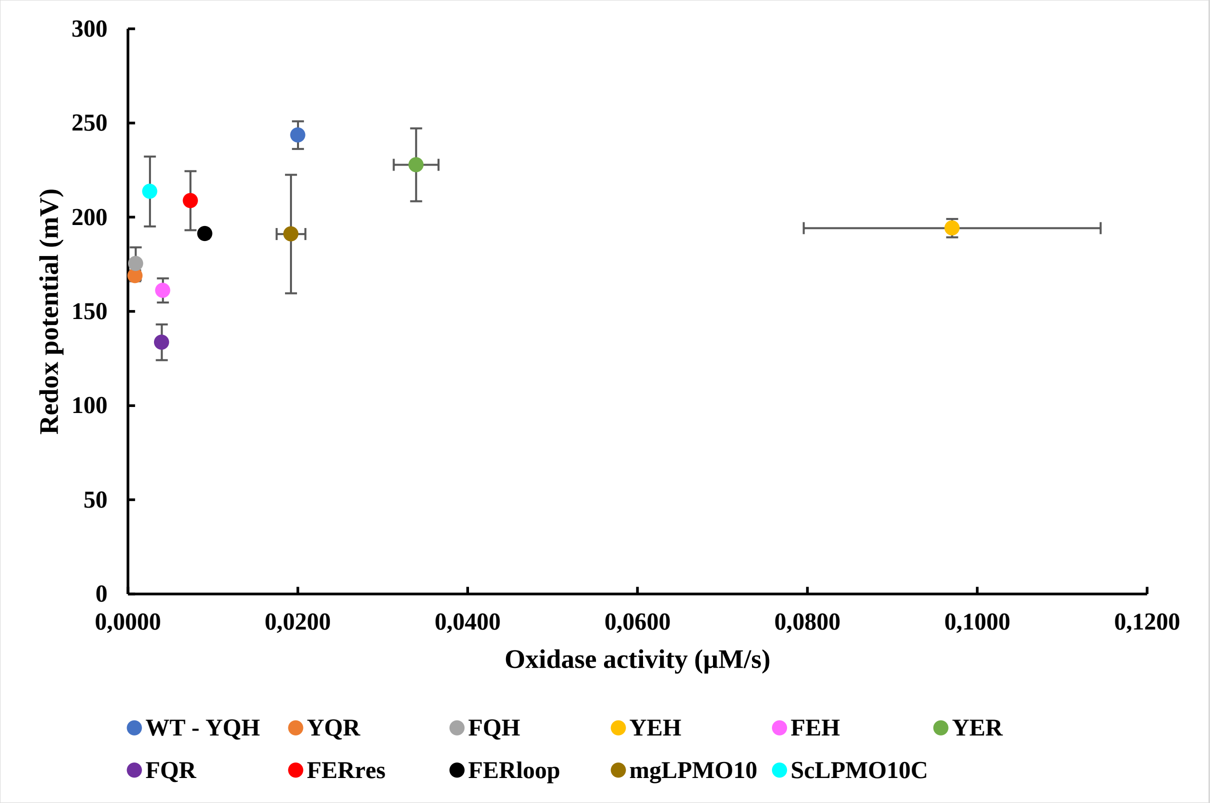

Figure 25. Correlation between the redox potential and oxidase activity for MaLPMO10B WT, the MaLPMO10B mutants, mgLPMO10, and ScLPMO10C. *The redox potential (Y-axis, mV) was determined as described in Section 3.3.6 and under Table 16. The oxidase activity (X-axis, µM/s) was obtained as described in Section 3.3.4 and Figure 21. The correlation between redox potential and oxidase activity is shown for the MaLPMO10B WT (blue), YQR (orange), FQH (grey), YEH (yellow), FEH (pink), YER (green), FQR (purple), FER*$_{res}$ *(red), and FER*$_{loop}$ *mutant (black), as well as mgLPMO10 (brown) and ScLPMO10C (cyan).*

4.4 Reductant and pH Effects on *Ma*LPMO10B WT and the YEH Mutant

4.4.1 Oxidase Activity of *Ma*LPMO10B WT and the YEH Mutant at pH 6 and pH 8

The oxidase activity of *Ma*LPMO10B WT and the YEH mutant was studied at pH 6 and pH 8 with ascorbic acid, gallic acid, or cysteine as reductants to investigate the impact pH and reductant have on the oxidase activity (Figure 26). The reactions contained 2 µM of LPMO, 100 µM amplex red, 5 U/mL HRP, and 1 mM reductant in 50 mM sodium phosphate buffer pH 6 or pH 8. The initial rates were divided by two to obtain the initial rate of oxidase activity per 1 µM of protein.

An increase in initial hydrogen peroxide production rate from pH 6 to pH 8 was observed for *Ma*LPMO10B WT and the YEH mutant when ascorbic acid was used as a reductant (Figure 26). The same trend was observed for *Ma*LPMO10B WT (0.01 ± 0.002 µM/s at pH 6 to 0.05 ± 0.02 µM/s at pH 8) and the YEH mutant (0.02 ± 0.004 µM/s at pH 6 to 0.05 ± 0.01 µM/s at pH 8) when cysteine was used as a reductant (Figure 26). The ascorbic acid only control, the cysteine only control, and the free copper control with cysteine as reductant displayed a slightly increased initial rate at pH 8 compared with pH 6.

The initial hydrogen peroxide production rate was lower for *Ma*LPMO10B WT (0.002 ± 0.0006 µM/s) and the YEH mutant (0.003 ± 0.0008 µM/s) when gallic acid was used as a reductant at pH 6 compared with when cysteine or ascorbic acid was used at the same pH (Figure 26A). Low initial rates were also observed for the free copper control and the gallic acid only control (Figure 26A). A 20-fold increase in the oxidase activity was observed at pH 8 for *Ma*LPMO10B WT (0.04 ± 0.01 µM/s) when gallic acid was used as a reductant (Figure 26B). An increase in oxidase activity, albeit lower than for *Ma*LPMO10B WT, was also observed for the YEH mutant (0.04 ± 0.01 µM/s) at pH 8 when gallic acid was used as a reductant (Figure 26B). The initial rates obtained for the gallic acid only control and the free copper control were equal to the initial rates obtained for *Ma*LPMO10B WT and the YEH mutant at both pH 6 and pH 8 (Figure 26). This suggests that gallic acid was the main factor for hydrogen peroxide production in the reactions were gallic acid was used as a reductant.

Overall, the initial hydrogen peroxide production rate increased from pH 6 to pH 8 with all of the reductants, with the exception of the free copper control with ascorbic acid as reductant.

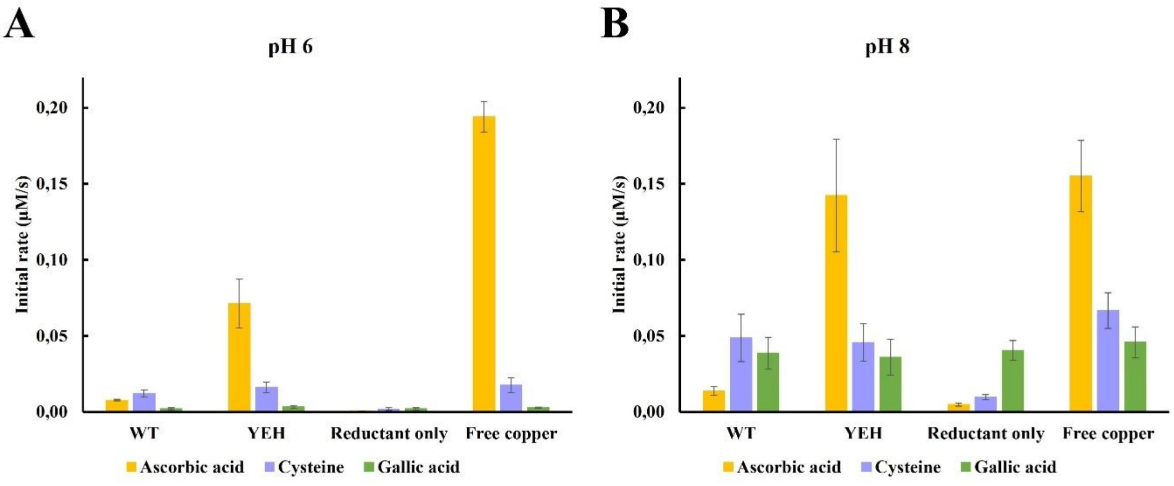

Figure 26. Oxidase activity for MaLPMO10B WT and the YEH mutant at pH 6 and pH 8 with ascorbic acid, gallic acid, or cysteine. *The initial hydrogen peroxide production rate (Y-axis, µM/s) for MaLPMO10B WT, the YEH mutant, the reductant only control, and free copper at (A) pH 6 or (B) pH 8 with either ascorbic acid (yellow), cysteine (purple), or gallic acid (green) as reductants. All reactions contained 2 µM of LPMO or $CuSO_4$ (except the reaction with only reductant), 1 mM reductant, 100 µM amplex red, and 5 U/mL HRP in 50 mM sodium phosphate buffer pH 6 or pH 8. The error bars indicate the standard deviation between three independent replicates. The initial rate was divided in two, to report the initial rate per 1 µM of protein.*

4.4.2 Analysis of Product Formation at pH 8 and pH 6 with Different Reductants

The type of reductant and the pH used yielded differences in oxidase activity (Section 4.4.1). To expand on this, the difference in C1-oxidized cello-oligosaccharide formation at pH 6 and pH 8 with ascorbic acid, gallic acid, or cysteine as reductants was explored. The reactions contained 1 µM of *Ma*LPMO10B WT or the YEH mutant, 1 mM reductant, and 0.1 % w/v PASC in 50 mM sodium phosphate buffer at pH 6 or pH 8. Figure 27 shows the differences in formation of C1-oxidized cello-oligosaccharides over time for *Ma*LPMO10B WT and the YEH mutant at pH 6 (A) or pH 8 (B) with ascorbic acid, gallic acid, or cysteine as reductants.

*Ma*LPMO10B WT had a rate of 0.1 µM/s when ascorbic acid was used as a reductant at pH 6, while the YEH mutant had an initial rate of 0.7 µM/s with the same conditions (previously mentioned in Section 4.3.4). The rate at which *Ma*LPMO10B WT produced C1-oxidized cello-oligosaccharides increased to 0.6 µM/s at pH 8, six times faster than at pH 6. At pH 8, the reaction reached completion after only 8 hours, whereas at pH 6 the reaction had still not plateaued after 24 hours (Figure 27A and B, top). However, the product concentration was equal at pH 6 and pH 8 for *Ma*LPMO10B WT, indicating that the reaction was likely completed. The YEH mutant still had a faster initial rate (0.9 µM/s) than *Ma*LPMO10B WT at pH 8 with ascorbic acid as a reductant. Inactivation of the YEH mutant occurred after only 1 hour at pH 8, while at pH 6, the YEH mutant inactivated after 4 hours with approximately twice the amount of product produced than observed at pH 8 (Figure 27A and B, top).

The rate of C1-oxidized cello-oligosaccharide formation increased substantially for *Ma*LPMO10B WT from pH 6 to pH 8 with gallic acid as reductant (Figure 27A and B, middle). The estimated initial product formation rate increased from 0.5 µM/s at pH 6 to 12.8 µM/s at pH 8. At pH 8, the reaction reached completion after only 15 minutes compared to after 8 hours at pH 6 (Figure 27A and B, middle). When gallic acid was used as a reductant, the YEH mutant no longer had a faster initial rate than *Ma*LPMO10B WT at either pH tested, but the rate did increase from pH 6 to pH 8 (0.2 µM/s to 1.3 µM/s). Inactivation occurred after 30 minutes at pH 8 and after 2 hours at pH 6 for the YEH mutant (Figure 27A and B, middle).

It was predicted that the rate of C1-oxidation would be faster at pH 8 than pH 6 with cysteine as a reductant. This was not the case, and an approximately eight times faster initial rate was observed at pH 6 (2.3 µM/s), than at pH 8 (0.3 µM/s) for *Ma*LPMO10B WT (Figure 27A and B, bottom). The reaction with *Ma*LPMO10B WT plateaued after 1 hour at pH 6 with less product produced than expected (75 ± 3 µM) (Figure 27A, bottom). At pH 8, the reaction with *Ma*LPMO10B WT plateaued after 2 hours with an even lower product concentration (33 ± 1 µM) (Figure 27B, bottom). The YEH mutant showed the same trend as *Ma*LPMO10B WT with cysteine as a reductant, with an estimated initial rate of 0.2 µM/s at pH 6 and 0.01 µM/s at pH 8. However, product concentration was very low for the YEH mutant when cysteine was used as a reductant at either pH (Figure 27A and B, bottom).

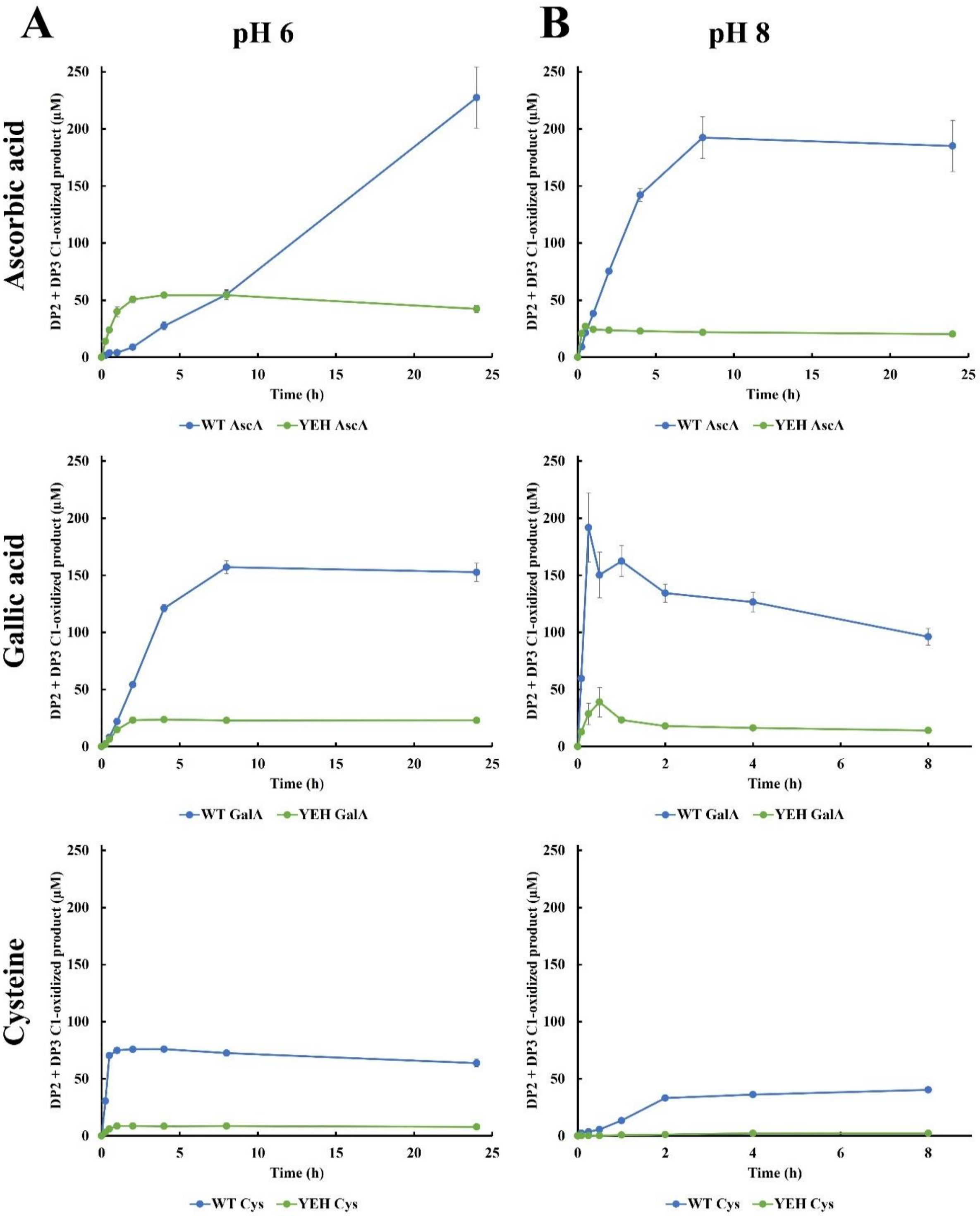

*Figure 27. **Production of C1-oxidized cello-oligosaccharides over time for MaLPMO10B WT and the YEH mutant at pH 6 or pH 8 with ascorbic acid, gallic acid, or cysteine as reductant.** Concentration of C1-oxidized cello-oligosaccharides (µM) over time (h) for MaLPMO10B WT (blue) and the YEH mutant (green) at (A) pH 6 and (B) pH 8 with ascorbic acid (AscA, top), gallic acid (GalA, middle), or cysteine (Cys, bottom) as the reductant. 1 µM of LPMO was incubated with 0.1 % w/v PASC and 1 mM reductant in 50 mM sodium phosphate pH 6 or pH 8 up to 24 hours. The reactions with gallic acid or cysteine as reductant at pH 8 were incubated over 8 hours. All samples were treated with TfCel6A prior to analysis. The error bars indicate the standard deviation for between three independent replicates at each time point, shown as dots. Error bars are not visible for some time points due to a low standard deviation.*

5 Discussion

LPMOs effectively degrade recalcitrant polysaccharides and are central in the shift towards a more sustainable economy. Therefore, understanding the catalytic mechanism resulting in oxidative cleavage of glycosidic bonds is of high importance. A conserved catalytic triad at the active site, also termed second sphere motif, was investigated to acquire knowledge on the catalytic mechanism of LPMOs. This work details the cloning and expression of eight *Ma*LPMO10B mutants with a second sphere motif found in other cellulose-active LPMOs (FER motif) and single and double mutants going from YQH to FER motifs in *Ma*LPMO10B.

5.1 Cloning and Expression

The cloning was successful for all the *Ma*LPMO10B mutants. Site-directed mutagenesis using whole-plasmid PCR amplification and NEBuilder DNA assembly were therefore suitable methods for introducing up to two and more than two mutations, respectively. Although cloning was successful, expression was low for all the *Ma*LPMO10B mutants, including *Ma*LPMO10B WT (Table 15). This is, as previously mentioned, an ongoing problem in our research group and the causes of these expression problems are not yet known. However, alterations in the media components by the manufacturer may be the issue. Some mutants, in particular the $\mathrm{FER}_{\mathrm{loop}}$ mutant, contained contaminating proteins after purification (Figure 15). The purification method could therefore be optimized to obtain more pure enzymes, e.g., by testing other pH values for the anion-exchange chromatography buffer so that the protein would bind the column and elute with a salt gradient. Despite the expression problems experienced throughout this thesis work, several series of purification yielded a sufficient amount of each *Ma*LPMO10B protein to proceed with characterization.

5.2 Activity towards Cellulose and Chitin

All mutants displayed activity towards cellulose (PASC) in the preliminary activity assay, albeit the two triple mutants and the FQR double mutants generated a low concentration of C1-oxidized product (Figure 16). These three mutants appeared to prefer C4-oxidation, while the remaining *Ma*LPMO10B mutants and *Ma*LPMO10B WT favored C1-oxidation of cellulose (Figure 18). The FQH mutant in particular favored C1-oxidation of cellulose, as C4-oxidation was almost completely abolished (Figure 17). It is worth noting that the product concentration was low for some of the mutants, therefore small changes in product concentration could drastically alter the presented C1:C4 ratio (Figure 18). This activity assay suggests that mutations in the active site catalytic triad of *Ma*LPMO10B may alter both the functionality and regioselectivity of the enzyme.

It was postulated that the enzymes that displayed higher activity towards C4-oxidation of cellulose might display higher activity towards β-chitin. This is because LPMOs that exhibit C1- and C4-oxidation of cellulose may also be active towards chitin, whereas LPMOs that only oxidize cellulose at the C1-carbon have not shown activity towards chitin (Forsberg *et al.*, 2018). The YEH and YER mutants appeared to favor C1-oxidation of PASC, similarly to *Ma*LPMO10B WT (Figure 18). However, the YER mutant displayed more C4-oxidation relative to C1-oxidation than *Ma*LPMO10B WT and the YEH mutant. The YEH and YER mutants were therefore not proposed to have increased chitin activity. However, these two mutants (YEH and YER) with a glutamine to glutamate mutation at position 219 appeared to generate more A2ox product than the other *Ma*LPMO10B mutants (Figure 19). Interestingly, the YEH mutant generated twice as much A2ox product than *Ma*LPMO10B WT that displayed the second highest A2ox product concentration. This was surprising due to the apparent regioselectivity of the YEH mutant, but also because *Ma*LPMO10B WT produced more oxidized cello-oligosaccharides than the YEH mutant (Figure 16 and Figure 17). The glutamine residue at position 219 could be involved in affinity towards or oxidation of β-chitin. To investigate whether this residue is involved in binding, affinity towards β-chitin and cellulose could be analyzed by measuring depletion of the YEH mutant in solution as assessed by UV/Vis spectrophotometry compared to *Ma*LPMO10B WT (Vaaje-Kolstad *et al.*, 2005b). The glutamine residue at position 219 has been proposed to be involved in the positioning of hydrogen peroxide and the generated hydroxyl radical, and maybe the N-acetyl-glucosamine units of β-chitin support hydrogen peroxide positioning when the glutamine at position 219 is mutated to a glutamate (Bissaro *et al.*, 2020).

5.3 *In Situ* Production of Hydrogen Peroxide Enhances the Rate of Oxidized Cello-Oligosaccharide Formation

In situ production of hydrogen peroxide without substrate present, i.e., the oxidase activity, was affected by the mutations introduced to the catalytic center of *Ma*LPMO10B. The initial hydrogen peroxide production rate for the YEH mutant was five times higher than the oxidase activity for *Ma*LPMO10B WT (Figure 21). The YER mutant also displayed a higher initial hydrogen peroxide production rate than *Ma*LPMO10B WT. These results clearly suggest that the glutamine to glutamate mutation at position 219 is involved in enhancing *in situ* generation of hydrogen peroxide. On the contrary, the two single mutants, YQR and FQH, appeared to have lost the ability to produce hydrogen peroxide. Similarly, the FEH and FQR second sphere motifs showed reduced hydrogen peroxide production. These results suggest that the tyrosine to phenylalanine mutation at position 221, e.g., in the FEH mutant, reduces generation of hydrogen peroxide. This suggestion is supported by the higher oxidase activity observed for the YEH and YER mutant compared with the FEH mutant, as the FEH mutant has both the enhancing glutamate mutation and the reducing phenylalanine mutation, whereas the YEH and YER mutants do not include the tyrosine to phenylalanine mutation. Both triple mutants with the FER motif produce hydrogen peroxide, albeit at reduced capacity compared with *Ma*LPMO10B WT or with mgLPMO10 that has FER as its natural second sphere motif. *Sc*LPMO10C also has a natural FER motif but generates less hydrogen peroxide than the FER_{res} and FER_{loop} mutants. However, the FER_{loop} mutant displays a slightly higher oxidase activity than the FER_{res} mutant, which indicates that the extra space introduced with the loop or the histidine to aspartate mutation at position 216, also evident in mgLPMO10 and *Sc*LPMO10B, may be involved in stabilizing the FER second sphere motif. These results also suggest that there are likely other residues in mgLPMO10, not yet investigated, which cause the increase in hydrogen peroxide generation. Overall, it appears as if a tyrosine in combination with a glutamate is important for optimal oxidase activity in bacterial LPMOs, since a phenylalanine and glutamate combination in the second sphere motif have a lower oxidase activity, as observed for bacterial AA10 LPMOs. This is a clear observation that should gain more attention and dedicated research.

Analysis of the generated C1-oxidized cello-oligosaccharides showed that the YEH mutant produced oxidized product seven times faster than *Ma*LPMO10B WT (Figure 20). Since the YEH mutant also has a higher initial hydrogen peroxide production rate than *Ma*LPMO10B, this supports previous findings that *in situ* generation of hydrogen peroxide is driving the rate of oxidized product formation (Bissaro *et al.*, 2017; Stepnov *et al.*, 2021). However, the YEH mutant inactivates after 4 hours as the total product concentration was lower than observed for *Ma*LPMO10B WT. In contrast, *Ma*LPMO10B WT generated oxidized product throughout the reaction time, supporting the theory that a steady and controlled supply of hydrogen peroxide is important to avoid enzyme inactivation (Bissaro *et al.*, 2017). The YEH mutant may inactivate prematurely as the glutamine residue at position 219 is predicted to be involved in stabilizing the generated hydroxyl radical (Bissaro *et al.*, 2020). Contrasting the YEH single mutant, the two other single mutants, FQH and YQR, have a slow and steady generation of C1-oxidized cello-oligosaccharides, corresponding to the low oxidase activity observed. The hydrogen peroxide used to produce the oxidized cello-oligosaccharides for these two mutants likely originates from a side-reaction between ascorbic acid and molecular oxygen (Bissaro *et al.*, 2017; Stepnov *et al.*, 2022b). The FEH double mutant displayed a slow rate of product formation, in line with the low oxidase activity observed with this second sphere motif. In contrast, both the YER and FQR double mutants had a fast initial rate of product formation, although the rate could not be determined accurately as rapid inactivation occurred. For the YER mutant, the fast rate may be explained by the enzyme's ability to generate hydrogen peroxide. However, this could not be the case for the FQR mutant, which generated a low amount of hydrogen peroxide (Figure 21). A reason for the fast initial rate of the FQR mutant could be that the mutant effectively utilizes the hydrogen peroxide available in the reaction, produced in side-reactions between ascorbic acid and molecular oxygen. Although a problem with this suggestion is that the hydrogen peroxide production between ascorbic acid and molecular oxygen normally is slow (Bissaro *et al.*, 2017). However, the speed of this reaction will increase as LPMOs inactivate and release free copper into solution (Stepnov *et al.*, 2022b). Therefore, it may be that some FQH mutants inactivate and release free copper into solution, whereas others are still oxidizing substrate, utilizing the accumulating hydrogen peroxide until the remaining product generating FQH mutants inactivate and catalysis cease. The two triple mutants, FER_{res} and FER_{loop}, appear to not produce much C1-oxidized product and the reaction plateaued early (Figure 20), although the rate of hydrogen peroxide production was higher for both these mutants than for the YQR, FQH, FEH, and FQR mutants (Figure 21). This may suggest that the two triple mutants are not very stable and that other residues in LPMOs, not yet investigated, help stabilize the second sphere motif. It is also worth noting that C1-oxidized product was analyzed and that both triple mutants appeared to favor C4-oxidation (Figure 18).

5.4 Utilization of Supplemented Hydrogen Peroxide

The LPMOs' ability to utilize hydrogen peroxide when 2,6-DMP is used as a substrate and a reductant was analyzed using the Breslmayr assay, which is suggested to be a peroxidase activity. All the *Ma*LPMO10B mutants displayed low peroxidase activity compared with *Ma*LPMO10B WT (Figure 24). Mutations to the catalytic center could have lowered the affinity towards 2,6-DMP, and potentially be involved in substrate binding. Especially the glutamine residue at position 219 may be involved in substrate binding as this residue is located closer to the surface of the enzyme compared with the tyrosine at position 221 and the alanine at position 214 in *Ma*LPMO10B WT. Another reason for the low observed peroxidase activity for the

*Ma*LPMO10B mutants could be that they are prone to inactivation upon external addition of hydrogen peroxide.

The generation of C1-oxidized cello-oligosaccharides in the peroxygenase reactions was low for all *Ma*LPMO10B mutants, and the mutants only produced one tenth of the product concentration observed for *Ma*LPMO10B WT (Figure 22). This again indicates that the *Ma*LPMO10B mutants are vulnerable to inactivation upon external addition of hydrogen peroxide. Also, the YEH mutant had a slower initial rate of C1-oxidized product formation than *Ma*LPMO10B WT. This is likely because hydrogen peroxide was externally added and the high oxidase activity of the YEH mutant was no longer a benefit during oxidation of cellulose.

The peroxygenase reaction with *Ma*LPMO10B WT plateaued prematurely with a lower product concentration (21 µM) than expected (Figure 22). External addition of 100 µM of hydrogen peroxide would have an expected yield of at least 100 µM of oxidized product, as hydrogen peroxide is most likely the limiting factor in LPMO reactions (Bissaro *et al.*, 2017; Müller *et al.*, 2018). It is worth considering that since *Ma*LPMO10B WT exhibit C1- and C4-activity towards cellulose, and only C1-oxidized product was quantified, some product may have been generated as C4-oxidized cello-oligosaccharides. However, it is unlikely that approximately 80 % of the total product concentration would be generated as C4-oxidized product since *Ma*LPMO10B WT favors C1-oxdiation (Figure 18). The attempts to reinitiate the plateaued reaction showed that both reductant and fresh enzyme had to be added to generate more C1-oxidized cello-oligosaccharides (Figure 23). This indicates that *Ma*LPMO10B WT inactivated prematurely concomitant depletion of the reductant. However, the amount of reductant added (10 µM) should not have been depleted during this time, as one electron is enough to drive the peroxygenase reaction for several catalytic cycles (Bissaro *et al.*, 2017). The reductant is likely depleted as oxidatively damaged LPMOs in solution can release free copper that enhances hydrogen peroxide production in a side-reaction where the reductant reduces free copper, which in turn reacts with molecular oxygen (Stepnov *et al.*, 2022b).

5.5 Correlation between Redox Potential and Oxidase Activity

It was expected that LPMOs with high oxidase activity would display a low redox potential and *vice versa*. This is because the first step in hydrogen peroxide production is the endergonic formation of $O_2^{\bullet-}$. Low reduction potential of LPMOs energetically favors the conversion of molecular oxygen to $O_2^{\bullet-}$ compared to LPMOs with a high reduction potential. However, a correlation analysis between the redox potential and oxidase activity of *Ma*LPMO10B WT, mgLPMO10, *Sc*LPMO10C, and all *Ma*LPMO10B mutants except for the YEH mutant showed a positive correlation. The YEH mutant was not included as it appeared to be an outlier (Figure 25). The observed positive correlation indicates that a high redox potential would give a high oxidase activity, which is the opposite of what was expected. Many of the *Ma*LPMO10B mutants did not display much activity in any of the characterization assays, which indicates that the mutants were not functioning optimally. Further, TMP_{red} may not be an optimal reductant for LPMOs and in association with the low activity observed for most mutants, the measurements may not reflect the differences between the *Ma*LPMO10B mutants. Other methods to measure the redox potential could potentially yield different results. However, the correlation observed here is likely a result of the low activity of the *Ma*LPMO10B mutants.

5.6 Altering the Second Sphere Residues in the Active Site of *Ma*LPMO10B

Mutating the second sphere residues in the active site of *Ma*LPMO10B gave insight into the complexity of LPMO second sphere motifs. The tyrosine residue (221), the histidine residue (216), and possibly the alanine residue (214) seem to be very important for LPMO activity, as activity decreased tremendously upon mutating these residues. Although hydrogen peroxide production was almost completely abolished, the *Ma*LPMO10B mutants with a YQR (containing the arginine mutation) or an FQH (containing the phenylalanine mutation) second sphere motif appeared to still be active and stable during oxidation of cellulose. In contrast, mutating the glutamine residue (219) to a glutamate residue increased hydrogen peroxide generation immensely and enhanced the initial rate of oxidized cello-oligosaccharide formation. Bissaro *et al.* (2020) observed the opposite for generation of oxidized product upon mutating the corresponding glutamate residue in *Sm*LPMO10A to a glutamine residue. Therefore, it was suggested that this glutamate residue is involved in hydrogen peroxide turnover and stabilization of both hydrogen peroxide and the hydroxyl radical (Bissaro *et al.*, 2020). Our results support that a glutamate residue in this position improves hydrogen peroxide turnover and *in situ* generation of hydrogen peroxide. The mutant with a YEH (containing the glutamate mutation) second sphere motif produced the highest concentration of oxidized product among the *Ma*LPMO10B mutants but inactivated during cellulose degradation. In contrast, the mutants with a YQR (containing the arginine mutation) and an FQH (containing the phenylalanine mutation) motif remained stable and active, albeit with very low generation of oxidized product. Therefore, all the second sphere residues investigated in this thesis appear to be crucial for the activity and stability of *Ma*LPMO10B.

Several of the second sphere motifs generated in this thesis can be found in Nature. The FER motif is common in the AA10 family, where the FQH motif also is present. The FQH motif is also evident in the AA9 family, along with the YEH and FEH second sphere motifs. Only three of the second sphere motifs generated in this thesis (YQR, YER, and FQR) have not yet been discovered as natural second sphere motifs among the LPMOs of family AA9 or AA10 in the CAZy database. The *Ma*LPMO10B mutant with an FQH motif was stable during degradation of cellulose. This may be because this motif can be found as a natural second sphere motif in AA10s and AA9s. The *Ma*LPMO10B mutants with a YEH or YER motif likely inactivated prematurely due to the high generation of hydrogen peroxide *in situ*. Furthermore, the YER motif is not found among the AA10 family in Nature, which could be one reason for the premature inactivation and instability of this mutant. The latter reasoning also applies for the mutant with an FQR second sphere motif which also appeared to be unstable and inactivate prematurely.

The FER second sphere motif is common among AA10-type LPMOs and is present in mgLPMO10 and *Sc*LPMO10C. However, the *Ma*LPMO10B mutants with this motif were less stable upon generation of C1-oxidized cello-oligosaccharides. Even though *Sc*LPMO10C and mgLPMO10 have the same second sphere motif, *Sc*LPMO10C showed low oxidase activity, whereas high oxidase activity was observed for mgLPMO10. It is tempting to speculate that the differences in oxidase activity could be a consequence of that these two LPMOs have evolved in different environments, as *Sc*LPMO10C originates from a soil bacterium, whereas mgLPMO10 was discovered in the metagenome of compost (Simmons *et al.*, 2014). Different environments may yield differences in activity as the external factors are unique to the environment and the requirements for each LPMO may therefore be different. There are likely residues outside the second sphere that account for this difference in oxidase activity. Other residues not yet investigated may also stabilize the FER motif in *Sc*LPMO10C and mgLPMO10. *Ma*LPMO10B may not contain these residues, which could explain why mutants with the FER motif generated little oxidized product and appeared to be less stable than other mutants. The FER_{loop} mutant generated slightly more hydrogen peroxide *in situ* than the FER_{res} mutant, which again suggests that residues in the loop region are involved in stabilizing the motif.

Since other residues likely stabilize the second sphere motif in AA10-type LPMOs, it can be assumed that this is the case for AA9-type LPMOs as well. Mutants with a natural AA9-type second sphere motif appeared to be more stable and active. This suggests that *Ma*LPMO10B may be more similar to LPMOs of family AA9, despite being a bacterial LPMO. The CAZy database group LPMOs based on sequence identity, not structure similarity (Levasseur *et al.*, 2013). Therefore, the way that *Ma*LPMO10B folds may resemble the folding of an AA9-type LPMO, and the residues that stabilize the second sphere motifs could be similarly positioned.

5.7 Type of Reductant and pH Affect the Rate of Cello-Oligosaccharide Formation

The mutant with the YEH second sphere motif showed the highest activity among the *Ma*LPMO10B mutants in the presence of molecular oxygen and an external reductant. This mutant displayed a higher oxidase activity, a higher initial rate of C1-oxidized cello-oligosaccharide formation, and a higher final A2ox product concentration than *Ma*LPMO10B WT. Further research therefore compared the YEH mutant and *Ma*LPMO10B WT, where the effect of changing pH and type of reductant was investigated.

To assess how different reductants (ascorbic acid, gallic acid, and cysteine) and pH affect the activity of *Ma*LPMO10B WT and the YEH mutant, we first investigated how *in situ* hydrogen peroxide production changed under various conditions. The oxidase activity increased from pH 6 to pH 8 with all reductants for *Ma*LPMO10B WT and the YEH mutant (Figure 26). Thus, we assumed that the initial rate of C1-oxidized product formation would increase from pH 6 to pH 8 to varying degrees depending on the type of reductant. The increase in oxidase activity is likely due to that the reductants are more deprotonated at pH 8 than at pH 6. This will increase the rate at which LPMO-Cu(II) is reduced as the reductants donate electrons more easily.

The YEH mutant was sevenfold faster than *Ma*LPMO10B WT at generating C1-oxidized cello-oligosaccharides at pH 6 with ascorbic acid as reductant (Figure 20 and Figure 27A). Increasing the pH from 6 to 8 with ascorbic acid increased the rate at which *Ma*LPMO10B WT produced C1-oxidized cello-oligosaccharides by sixfold (Figure 27). The initial rate of the YEH mutant also increased and was still faster than the rate observed for *Ma*LPMO10B WT at pH 8. This suggests that the hydrogen peroxide production by the YEH mutant at either pH provides an advantage for generating C1-oxidized product. However, the YEH mutant inactivated after only 1 hour at pH 8, in contrast to after 4 hours at pH 6 with twice the amount of product observed than at pH 8. This indicates that the YEH mutant functions more optimally at pH 6 than at pH 8, whereas *Ma*LPMO10B WT appears to be more stable and withstand changes in pH better. The reaction with *Ma*LPMO10B WT also plateaued earlier at pH 8 than at pH 6, where the reaction did not plateau, but this was likely due to that the reaction reached completion, not enzyme inactivation. This pattern is also evident for *Ma*LPMO10B WT in reactions where gallic acid was used as a reductant.

In reactions where gallic acid was used as a reductant, the rate at which *Ma*LPMO10B WT generated C1-oxidized product increased by 25-fold from pH 6 to pH 8 (Figure 27). This suggests that gallic acid is more prone to auto-oxidation at pH 8 compared to at pH 6. The initial rate of C1-oxidized product formation for the YEH mutant was slower at both pH 6 and pH 8 compared with *Ma*LPMO10B WT. The opposite was observed when ascorbic acid was used as a reductant, which suggests that type of reductant influences *in situ* generation of hydrogen peroxide and hydrogen peroxide production from auto-oxidation of the reductant. The oxidase activity assay showed a similar rate of *in situ* hydrogen peroxide production for *Ma*LPMO10B WT and the YEH mutant when gallic acid was used as a reductant, in contrast to the different initial rates observed for C1-oxidized cello-oligosaccharide formation (Figure 26). Interestingly, the reaction without enzyme in the oxidase activity assay showed the same initial rate of hydrogen peroxide production as the reactions with enzyme (Figure 26). This suggests that auto-oxidation of gallic acid accounts for most of the hydrogen peroxide production when used as a reductant. A similar trend was observed by Stepnov *et al.* (2021) where the reaction without enzyme showed approximately the same oxidase activity as the reaction with enzyme. The YEH mutant also inactivated faster at pH 8 than at pH 6, which supports the indication that this mutant functions optimally at pH 6.

The rate at which *Ma*LPMO10B WT generated C1-oxidized product was enhanced at pH 6 with cysteine as reductant compared to when ascorbic acid or gallic acid was used, although the enzyme inactivated prematurely (Figure 27). This correlates with recent results from a similar experiment with a different LPMO (Stepnov *et al.*, 2022a). We expected to observe an enhanced initial rate at pH 8 for the reactions with cysteine as well, since the oxidase activity increased from pH 6 to pH 8 and because cysteine also will be more deprotonated at pH 8. On the contrary, the rate at which *Ma*LPMO10B WT generated C1-oxidized cello-oligosaccharides decreased by almost eightfold from pH 6 to pH 8 (Figure 27). A similar trend was observed for the YEH mutant, although product concentration was very low.

The p*K*a of cysteine is approximately 8.2 (Nelson & Cox, 2005). This means that at pH 8, approximately half of the cysteine in the deprotonated form will be in equilibrium with the other half in the protonated form. At pH 6, most of the cysteine molecules will be in the protonated form. Interestingly, the concentration of generated C1-oxidized cello-oligosaccharides was approximately half at pH 8 compared with pH 6 upon inactivation of *Ma*LPMO10B WT when cysteine was used as a reductant (Figure 27). It is tempting to speculate that the deprotonated form of cysteine is more capable of binding or reacting with other cysteine molecules or components in the reaction. Evidence for this comes from a stopped-flow spectrophotometry study of cysteine reduction of *Sm*LPMO10A where the plot of observed rates with cysteine concentration yielded a sigmoidal curve resembling a binding isotherm (I. Ayuso-Fernandez, pers. com., 2022). This proposed binding process is likely to be more favored at high than low pH since the presence of an anionic charge would render the cysteine a better nucleophile than when it is neutral.

6 Conclusion and Future Perspectives

In this thesis work, we established that the second sphere residues of LPMOs are crucial for activity. Mutations to the second sphere residues investigated in this thesis displayed differences in activity towards PASC and β-chitin depending on which residue that was altered, and the number of mutations introduced. A single glutamine to glutamate mutation at position 219 (the YEH mutant) improved the product yield from degradation of β-chitin, whereas the product yield from cellulose degradation decreased compared to *Ma*LPMO10B WT under equal conditions. Modifications to the second sphere motif may also alter the regioselectivity of the protein and possibly the substrate affinity. However, a substrate binding assay should be performed to establish if substrate affinity is changed, although this would require removal of the CBM to assess the substrate affinity of the catalytic domain as the CBM often appears to be the dominating part in substrate binding. The YEH mutant was interesting as both the rate of oxidized cello-oligosaccharide formation and the rate of *in situ* hydrogen peroxide generation increased. This supports previous suggestions that a glutamate in this position may improve hydrogen peroxide turnover (Bissaro *et al.*, 2020). It is also highly likely that other residues are involved in stabilizing the second sphere residues as mutants with the FER motif, mgLPMO10, and *Sc*LPMO10C display differences in generation of hydrogen peroxide, despite containing the same second sphere motif. The clear observation that a tyrosine and a glutamate residue in the catalytic triad increase oxidase activity in AA10-type LPMOs, whereas a phenylalanine in combination with a glutamate decrease oxidase activity, should be devoted more research.

Further investigations in this thesis focused on how changes in pH and type of reductant affected the properties of the YEH mutant and *Ma*LPMO10B WT. The results showed that the oxidase activity increased from pH 6 to pH 8 with all reductants tested for both *Ma*LPMO10B WT and the YEH mutant. *Ma*LPMO10B WT generated comparable concentrations of oxidized cello-oligosaccharides at both pH 6 and pH 8, whereas the YEH mutant had optimal activity at pH 6. The type of reductant used appeared to influence the hydrogen peroxide production, both *in situ* by the enzyme and by auto-oxidation of the reductant. This again affects the rate of oxidized cello-oligosaccharide formation.

Future investigations to gain more insight into how alterations to the second sphere motifs, change in pH, and type of reductant affect LPMOs may yield valuable understanding to improve existing applications. Attempts to discover other residues involved in stabilizing the residues in the second sphere motif should be of interest to generate mutants with higher activity. However, they may be difficult to identify if the residues are not conserved alongside the second sphere motif. Further research to uncover why the YEH mutant displayed higher activity towards chitin may yield a better understanding of substrate specificity for C1- and C4-oxidizing LPMOs. In addition, knowledge about the optimal pH and reductant for each LPMO may be important in industrial settings. Optimization of polysaccharide degradation would result in a higher yield of valuable and sustainable products that can diminish the demand for petroleum-based products, and thereby reduce climate changes.

7 References

Agger, J. W., Isaksen, T., Varnai, A., Vidal-Melgosa, S., Willats, W. G. T., Ludwig, R., Horn, S. J., Eijsink, V. G. H. & Westereng, B. (2014). Discovery of LPMO activity on hemicelluloses shows the importance of oxidative processes in plant cell wall degradation. *Proceedings of the National Academy of Sciences of the United States of America*, 111 (17): 6287-6292. doi: 10.1073/pnas.1323629111.

Banerjee, S., Muderspach, S. J., Tandrup, T., Frandsen, K. E. H., Singh, R. K., Ipsen, J. O., Hernandez-Rollan, C., Norholm, M. H. H., Bjerrum, M. J., Johansen, K. S., et al. (2022). Protonation state of an important histidine from high resolution structures of lytic polysaccharide monooxygenases. *Biomolecules*, 12 (2): 15. doi: 10.3390/biom12020194.

Baruah, J., Nath, B. K., Sharma, R., Kumar, S., Deka, R. C., Baruah, D. C. & Kalita, E. (2018). Recent trends in the pretreatment of lignocellulosic biomass for value-added products. *Frontiers in Energy Research*, 6: 19. doi: 10.3389/fenrg.2018.00141.

Beeson, W. T., Phillips, C. M., Cate, J. H. D. & Marletta, M. A. (2012). Oxidative cleavage of cellulose by fungal copper-dependent polysaccharide monooxygenases. *Journal of the American Chemical Society*, 134 (2): 890-892. doi: 10.1021/ja210657t.

Bertini, L., Breglia, R., Lambrughi, M., Fantucci, P., De Gioia, L., Borsari, M., Sola, M., Bortolotti, C. A. & Bruschi, M. (2018). Catalytic mechanism of fungal lytic polysaccharide monooxygenases investigated by first-principles calculations. *Inorganic Chemistry*, 57 (1): 86-97. doi: 10.1021/acs.inorgchem.7b02005.

Bissaro, B., Rohr, A. K., Muller, G., Chylenski, P., Skaugen, M., Forsberg, Z., Horn, S. J., Vaaje-Kolstad, G. & Eijsink, V. G. H. (2017). Oxidative cleavage of polysaccharides by monocopper enzymes depends on H2O2. *Nature Chemical Biology*, 13 (10): 1123-1131. doi: 10.1038/nchembio.2470.

Bissaro, B., Streit, B., Isaksen, I., Eijsink, V. G. H., Beckham, G. T., DuBois, J. L. & Rohr, A. K. (2020). Molecular mechanism of the chitinolytic peroxygenase reaction. *Proceedings of the National Academy of Sciences of the United States of America*, 117 (3): 1504-1513. doi: 10.1073/pnas.1904889117.

Breslmayr, E., Hanzek, M., Hanrahan, A., Leitner, C., Kittl, R., Santek, B., Oostenbrink, C. & Ludwig, R. (2018). A fast and sensitive activity assay for lytic polysaccharide monooxygenase. *Biotechnology for Biofuels*, 11: 13. doi: 10.1186/s13068-018-1063-6.

Brown, R. M. (2004). Cellulose structure and biosynthesis: what is in store for the 21st century? *Journal of Polymer Science Part a-Polymer Chemistry*, 42 (3): 487-495. doi: 10.1002/pola.10877.

Cataldi, T. R. I., Campa, C. & De Benedetto, G. E. (2000). Carbohydrate analysis by high-performance anion-exchange chromatography with pulsed amperometric detection: the potential is still growing. *Fresenius Journal of Analytical Chemistry*, 368 (8): 739-758. doi: 10.1007/s002160000588.

Cheah, W. Y., Sankaran, R., Pau, L. S., Ibrahim, T., Chew, K. W., Culaba, A. & Chang, J. S. (2020). Pretreatment methods for lignocellulosic biofuels production: current advances, challenges and future prospects. *Biofuel Research Journal*, 7 (1): 1115-1127. doi: 10.18331/brj2020.7.1.4.

Chylenski, P., Bissaro, B., Sørlie, M., Røhr, Å. K., Várnai, A., Horn, S. J. & Eijsink, V. G. H. (2019). Lytic polysaccharide monooxygenases in enzymatic processing of lignocellulosic biomass. *ACS Catalysis*, 9 (6): 4970-4991. doi: 10.1021/acscatal.9b00246.

Couturier, M., Ladeveze, S., Sulzenbacher, G., Ciano, L., Fanuel, M., Moreau, C., Villares, A., Cathala, B., Chaspoul, F., Frandsen, K. E., et al. (2018). Lytic xylan oxidases from wood-decay fungi unlock biomass degradation. *Nature Chemical Biology*, 14 (3): 306-310. doi: 10.1038/nchembio.2558.

Danneels, B., Tanghe, M. & Desmet, T. (2019). Structural features on the substrate-binding surface of fungal lytic polysaccharide monooxygenases determine their oxidative regioselectivity. *Biotechnology Journal*, 14 (3): 10. doi: 10.1002/biot.201800211.

Duchesne, L. C. & Larson, D. W. (1989). Cellulose and the evolution of plant life. *Bioscience*, 39 (4): 238-241. doi: 10.2307/1311160.

Epiphyte. (2022). *LEX bioreactors*. Available at: https://www.epiphyte3.com/LEX (accessed: 22.03.22).

Filiatrault-Chastel, C., Navarro, D., Haon, M., Grisel, S., Herpoel-Gimbert, I., Chevret, D., Fanuel, M., Henrissat, B., Heiss-Blanquet, S., Margeot, A., et al. (2019). AA16, a new lytic polysaccharide monooxygenase family identified in fungal secretomes. *Biotechnology for Biofuels*, 12: 15. doi: 10.1186/s13068-019-1394-y.

Forsberg, Z., Vaaje-Kolstad, G., Westereng, B., Bunaes, A. C., Stenstrom, Y., MacKenzie, A., Sorlie, M., Horn, S. J. & Eijsink, V. G. H. (2011). Cleavage of cellulose by a CBM33 protein. *Protein Science*, 20 (9): 1479-1483. doi: 10.1002/pro.689.

Forsberg, Z., Mackenzie, A. K., Sorlie, M., Rohr, A. K., Helland, R., Arvai, A. S., Vaaje-Kolstad, G. & Eijsink, V. G. H. (2014). Structural and functional characterization of a conserved pair of bacterial cellulose-oxidizing lytic polysaccharide monooxygenases. *Proceedings of the National Academy of Sciences of the United States of America*, 111 (23): 8446-8451. doi: 10.1073/pnas.1402771111.

Forsberg, Z., Bissaro, B., Gullesen, J., Dalhus, B., Vaaje-Kolstad, G. & Eijsink, V. G. H. (2018). Structural determinants of bacterial lytic polysaccharide monooxygenase functionality. *Journal of Biological Chemistry*, 293 (4): 1397-1412. doi: 10.1074/jbc.M117.817130.

Gardner, K. H. & Blackwell, J. (1974). Hydrogen-bonding in native cellulose. *Biochimica Et Biophysica Acta*, 343 (1): 232-237. doi: 10.1016/0304-4165(74)90256-6.

Gardner, K. H. & Blackwell, J. (1975). Refinement of the structure of beta-chitin. *Biopolymers*, 14 (8): 1581-95. doi: 10.1002/bip.1975.360140804.

Gooday, G. W. (1990). The ecology of chitin degradation. *Advances in Microbial Ecology*, 11: 387-430. doi: 10.1007/978-1-4684-7612-5_10.

Hamre, A. G., Eide, K. B., Wold, H. H. & Sørlie, M. (2015). Activation of enzymatic chitin degradation by a lytic polysaccharide monooxygenase. *Carbohydrate Research*, 407: 166-169. doi: 10.1016/j.carres.2015.02.010.

Hamre, A. G., Stromnes, A. G. S., Gustavsen, D., Vaaje-Kolstad, G., Eijsink, V. G. H. & Sorlie, M. (2019). Treatment of recalcitrant crystalline polysaccharides with lytic polysaccharide monooxygenase relieves the need for glycoside hydrolase processivity. *Carbohydrate Research*, 473: 66-71. doi: 10.1016/j.carres.2019.01.001.

Igarashi, K., Uchihashi, T., Koivula, A., Wada, M., Kimura, S., Okamoto, T., Penttila, M., Ando, T. & Samejima, M. (2011). Traffic jams reduce hydrolytic efficiency of cellulase on cellulose surface. *Science*, 333 (6047): 1279-1282. doi: 10.1126/science.1208386.

Karkehabadi, S., Hansson, H., Kim, S., Piens, K., Mitchinson, C. & Sandgren, M. (2008). The first structure of a glycoside hydrolase family 61 member, Cel61B from Hypocrea jecorina, at 1.6 angstrom resolution. *Journal of Molecular Biology*, 383 (1): 144-154. doi: 10.1016/j.jmb.2008.08.016.

Kim, S., Stahlberg, J., Sandgren, M., Paton, R. S. & Beckham, G. T. (2014). Quantum mechanical calculations suggest that lytic polysaccharide monooxygenases use a copper-oxyl, oxygen-rebound mechanism. *Proceedings of the National Academy of*

Sciences of the United States of America, 111 (1): 149-154. doi: 10.1073/pnas.1316609111.

Kittl, R., Kracher, D., Burgstaller, D., Haltrich, D. & Ludwig, R. (2012). Production of four Neurospora crassa lytic polysaccharide monooxygenases in Pichia pastoris monitored by a fluorimetric assay. *Biotechnology for Biofuels*, 5. doi: 10.1186/1754-6834-5-79.

Kumar, A. K. & Sharma, S. (2017). Recent updates on different methods of pretreatment of lignocellulosic feedstocks: a review. *Bioresources and Bioprocessing*, 4: 19. doi: 10.1186/s40643-017-0137-9.

Kumar, R., Tabatabaei, M., Karimi, K. & Horvath, I. S. (2016). Recent updates on lignocellulosic biomass derived ethanol - a review. *Biofuel Research Journal*, 3 (1): 347-356. doi: 10.18331/brj2016.3.1.4.

Kuusk, S., Bissaro, B., Kuusk, P., Forsberg, Z., Eijsink, V. G. H., Sorlie, M. & Valjamae, P. (2018). Kinetics of H2O2-driven degradation of chitin by a bacterial lytic polysaccharide monooxygenase. *Journal of Biological Chemistry*, 293 (2): 523-531. doi: 10.1074/jbc.M117.817593.

Levasseur, A., Drula, E., Lombard, V., Coutinho, P. M. & Henrissat, B. (2013). Expansion of the enzymatic repertoire of the CAZy database to integrate auxiliary redox enzymes. *Biotechnology for Biofuels*, 6: 14. doi: 10.1186/1754-6834-6-41.

Li, X., Beeson, W. T., Phillips, C. M., Marletta, M. A. & Cate, J. H. D. (2012). Structural basis for substrate targeting and catalysis by fungal polysaccharide monooxygenases. *Structure*, 20 (6): 1051-1061. doi: 10.1016/j.str.2012.04.002.

Limayem, A. & Ricke, S. C. (2012). Lignocellulosic biomass for bioethanol production: current perspectives, potential issues and future prospects. *Progress in Energy and Combustion Science*, 38 (4): 449-467. doi: 10.1016/j.pecs.2012.03.002.

Liu, Y. N., Seefeldt, L. C. & Parker, V. D. (1997). Entropies of redox reactions between proteins and mediators: the temperature dependence of reversible electrode potentials in aqueous buffers. *Analytical Biochemistry*, 250 (2): 196-202. doi: 10.1006/abio.1997.2222.

Loose, J. S. M., Forsberg, Z., Fraaije, M. W., Eijsink, V. G. H. & Vaaje-Kolstad, G. (2014). A rapid quantitative activity assay shows that the Vibrio cholerae colonization factor GbpA is an active lytic polysaccharide monooxygenase. *Febs Letters*, 588 (18): 3435-3440. doi: 10.1016/j.febslet.2014.07.036.

Loose, J. S. M., Forsberg, Z., Kracher, D., Scheiblbrandner, S., Ludwig, R., Eijsink, V. G. H. & Vaaje-Kolstad, G. (2016). Activation of bacterial lytic polysaccharide monooxygenases with cellobiose dehydrogenase. *Protein Science*, 25 (12): 2175-2186. doi: 10.1002/pro.3043.

Maurya, D. P., Singla, A. & Negi, S. (2015). An overview of key pretreatment processes for biological conversion of lignocellulosic biomass to bioethanol. *3 Biotech*, 5 (5): 597-609. doi: 10.1007/s13205-015-0279-4.

Menon, V. & Rao, M. (2012). Trends in bioconversion of lignocellulose: biofuels, platform chemicals & biorefinery concept. *Progress in Energy and Combustion Science*, 38 (4): 522-550. doi: 10.1016/j.pecs.2012.02.002.

Miller, J. M. (2005). *Chromatography: concepts and contrasts*. 2nd ed.: John Wiley & Sons Inc.

Minke, R. & Blackwell, J. (1978). The structure of alpha-chitin. *Journal of Molecular Biology*, 120 (2): 167-181. doi: 10.1016/0022-2836(78)90063-3.

Müller, G., Varnai, A., Johansen, K. S., Eijsink, V. G. H. & Horn, S. J. (2015). Harnessing the potential of LPMO-containing cellulase cocktails poses new demands on processing conditions. *Biotechnology for Biofuels*, 8: 9. doi: 10.1186/s13068-015-0376-y.

Müller, G., Chylenski, P., Bissaro, B., Eijsink, V. G. H. & Horn, S. J. (2018). The impact of hydrogen peroxide supply on LPMO activity and overall saccharification efficiency of a commercial cellulase cocktail. *Biotechnology for Biofuels*, 11: 17. doi: 10.1186/s13068-018-1199-4.

Nelson, D. L. & Cox, M. M. (2005). *Lehninger principles of biochemistry*. 7th ed.: W.H. Freeman and Company.

NewEnglandBioLabsInc. (2022a). *NEBuilder HiFi DNA assembly reaction protocol*. Available at: https://international.neb.com/protocols/2014/11/26/nebuilder-hifi-dna-assembly-reaction-protocol (accessed: 08.03.22).

NewEnglandBioLabsInc. (2022b). *Protocol for Q5® high-fidelity 2 x master mix*. Available at: https://international.neb.com/protocols/2012/12/07/protocol-for-q5-high-fidelity-2x-master-mix-m0492 (accessed: 08.03.22).

Nishiyama, Y., Langan, P. & Chanzy, H. (2002). Crystal structure and hydrogen-bonding system in cellulose 1 beta from synchrotron X-ray and neutron fiber diffraction. *Journal of the American Chemical Society*, 124 (31): 9074-9082. doi: 10.1021/ja0257319.

Nishiyama, Y., Sugiyama, J., Chanzy, H. & Langan, P. (2003). Crystal structure and hydrogen bonding system in cellulose 1 alpha from synchrotron X-ray and neutron fiber diffraction. *Journal of the American Chemical Society*, 125 (47): 14300-14306. doi: 10.1021/ja037055w.

O'Sullivan, A. C. (1997). Cellulose: the structure slowly unravels. *Cellulose*, 4 (3): 173-207. doi: 10.1023/a:1018431705579.

Parthasarathi, R., Bellesia, G., Chundawat, S. P. S., Dale, B. E., Langan, P. & Gnanakaran, S. (2011). Insights into hydrogen bonding and stacking interactions in cellulose. *Journal of Physical Chemistry A*, 115 (49): 14191-14202. doi: 10.1021/jp203620x.

Payne, C. M., Baban, J., Horn, S. J., Backe, P. H., Arvai, A. S., Dalhus, B., Bjoras, M., Eijsink, V. G. H., Sorlie, M., Beckham, G. T., et al. (2012). Hallmarks of processivity in glycoside hydrolases from crystallographic and computational studies of the Serratia marcescens chitinases. *Journal of Biological Chemistry*, 287 (43): 36322-36330. doi: 10.1074/jbc.M112.402149.

Phillips, C. M., Beeson, W. T., Cate, J. H. & Marletta, M. A. (2011). Cellobiose dehydrogenase and a copper-dependent polysaccharide monooxygenase potentiate cellulose degradation by Neurospora crassa. *ACS Chemical Biology*, 6 (12): 1399-1406. doi: 10.1021/cb200351y.

Prasad, A., Sotenko, M., Blenkinsopp, T. & Coles, S. R. (2016). Life cycle assessment of lignocellulosic biomass pretreatment methods in biofuel production. *The International Journal of Life Cycle Assessment*, 21 (1): 44-50. doi: 10.1007/s11367-015-0985-5.

Quinlan, R. J., Sweeney, M. D., Leggio, L. L., Otten, H., Poulsen, J. C. N., Johansen, K. S., Krogh, K., Jorgensen, C. I., Tovborg, M., Anthonsen, A., et al. (2011). Insights into the oxidative degradation of cellulose by a copper metalloenzyme that exploits biomass components. *Proceedings of the National Academy of Sciences of the United States of America*, 108 (37): 15079-15084. doi: 10.1073/pnas.1105776108.

Reilly, P. J. (2007). Chapter 5 - Amylase and cellulase structure and function. In Yang, S.-T. (ed.) *Bioprocessing for Value-Added Products from Renewable Resources*, pp. 119-130. Amsterdam: Elsevier.

Rieder, L., Petrovic, D., Valjamae, P., Eijsink, V. G. H. & Sorlie, M. (2021). Kinetic characterization of a putatively chitin-active LPMO reveals a preference for soluble substrates and absence of monooxygenase activity. *ACS Catalysis*, 11 (18): 11685-11695. doi: 10.1021/acscatal.1c03344.

Rooni, V., Raud, M. & Kikas, T. (2017). The freezing pre-treatment of lignocellulosic material: a cheap alternative for Nordic countries. *Energy*, 139: 1-7. doi: 10.1016/j.energy.2017.07.146.

Rudall, K. M. & Kenchington, W. (1973). The chitin system. *Biological Reviews*, 48 (4): 597-633. doi: 10.1111/j.1469-185X.1973.tb01570.x.

Sabbadin, F., Hemsworth, G. R., Ciano, L., Henrissat, B., Dupree, P., Tryfona, T., Marques, R. D. S., Sweeney, S. T., Besser, K., Elias, L., et al. (2018). An ancient family of lytic polysaccharide monooxygenases with roles in arthropod development and biomass digestion. *Nature Communications*, 9: 12. doi: 10.1038/s41467-018-03142-x.

Sabbadin, F., Urresti, S., Henrissat, B., Avrova, A. O., Welsh, L. R. J., Lindley, P. J., Csukai, M., Squires, J. N., Walton, P. H., Davies, G. J., et al. (2021). Secreted pectin monooxygenases drive plant infection by pathogenic oomycetes. *Science*, 373 (6556): 774-779. doi: 10.1126/science.abj1342.

Sharma, H. K., Xu, C. B. & Qin, W. S. (2019). Biological pretreatment of lignocellulosic biomass for biofuels and bioproducts: an overview. *Waste and Biomass Valorization*, 10 (2): 235-251. doi: 10.1007/s12649-017-0059-y.

Simmons, C. W., Reddy, A. P., D'Haeseleer, P., Khudyakov, J., Billis, K., Pati, A., Simmons, B. A., Singer, S. W., Thelen, M. P. & VanderGheynst, J. S. (2014). Metatranscriptomic analysis of lignocellulolytic microbial communities involved in high-solids decomposition of rice straw. *Biotechnology for Biofuels*, 7: 13. doi: 10.1186/s13068-014-0180-0.

Sorlie, M., Seefeldt, L. C. & Parker, V. D. (2000). Use of stopped-flow spectrophotometry to establish midpoint potentials for redox proteins. *Analytical Biochemistry*, 287 (1): 118-125. doi: 10.1006/abio.2000.4826.

Stepnov, A. A., Forsberg, Z., Sorlie, M., Nguyen, G. S., Wentzel, A., Rohr, A. K. & Eijsink, V. G. H. (2021). Unraveling the roles of the reductant and free copper ions in LPMO kinetics. *Biotechnology for Biofuels*, 14 (1). doi: 10.1186/s13068-021-01879-0.

Stepnov, A. A., Christensen, I. A., Forsberg, Z., Aachmann, F. L., Courtade, G. & Eijsink, V. G. H. (2022a). The impact of reductants on the catalytic efficiency of a lytic polysaccharide monooxygenase and the special role of dehydroascorbic acid. *FEBS LETTERS*, 596 (1): 53-70. doi: 10.1002/1873-3468.14246.

Stepnov, A. A., Eijsink, V. G. H. & Forsberg, Z. (2022b). Enhanced in situ H2O2 production explains synergy between an LPMO with a cellulose-binding domain and a single-domain LPMO. *Scientific Reports*, 12 (1): 6129. doi: 10.1038/s41598-022-10096-0.

Teeri, T. T. (1997). Crystalline cellulose degradation: new insight into the function of cellobiohydrolases. *Trends in Biotechnology*, 15 (5): 160-167. doi: 10.1016/s0167-7799(97)01032-9.

ThermoFisherScientific. (2022). *Chemically competent cells*. Available at: https://www.thermofisher.com/no/en/home/life-science/cloning/competent-cells-for-transformation/chemically-competent.html (accessed: 08.03.22).

Tokin, R., Ipsen, J. O., Westh, P. & Johansen, K. S. (2020). The synergy between LPMOs and cellulases in enzymatic saccharification of cellulose is both enzyme- and substrate-dependent. *Biotechnology Letters*, 42 (10): 1975-1984. doi: 10.1007/s10529-020-02922-0.

Tran, T. T. A., Le, T. K. P., Mai, T. P. & Nguyen, D. Q. (2019). Production from lignocellulosic biomass. In *Alcohol Fuels - Current Technologies and Future Prospect*: IntechOpen.

Vanderhart, D. L. & Atalla, R. H. (1984). Studies of microstructure in native celluloses using solid-state C-13 NMR. *Macromolecules*, 17 (8): 1465-1472. doi: 10.1021/ma00138a009.

Vanholme, B., Desmet, T., Ronsse, F., Rabaey, K., Van Breusegem, F., De Mey, M., Soetaert, W. & Boerjan, W. (2013). Towards a carbon-negative sustainable bio-based economy. *Frontiers in Plant Science*, 4. doi: 10.3389/fpls.2013.00174.

Vu, V. V., Beeson, W. T., Span, E. A., Farquhar, E. R. & Marletta, M. A. (2014). A family of starch-active polysaccharide monooxygenases. *Proceedings of the National Academy of Sciences of the United States of America*, 111 (38): 13822-13827. doi: 10.1073/pnas.1408090111.

VWR. (2022). *VWR Red Taq DNA polymerase master mix* Version: VWR 05/2017 Cat. no. 733-2546.

Vaaje-Kolstad, G., Horn, S. J., van Aalten, D. M. F., Synstad, B. & Eijsink, V. G. H. (2005a). The non-catalytic chitin-binding protein CBP21 from Serratia marcescens is essential for chitin degradation. *Journal of Biological Chemistry*, 280 (31): 28492-28497. doi: 10.1074/jbc.M504468200.

Vaaje-Kolstad, G., Houston, D. R., Riemen, A. H. K., Eijsink, V. G. H. & van Aalten, D. M. F. (2005b). Crystal structure and binding properties of the Serratia marcescens chitin-binding protein CBP21. *Journal of Biological Chemistry*, 280 (12): 11313-11319. doi: 10.1074/jbc.M407175200.

Vaaje-Kolstad, G., Westereng, B., Horn, S. J., Liu, Z. L., Zhai, H., Sorlie, M. & Eijsink, V. G. H. (2010). An oxidative enzyme boosting the enzymatic conversion of recalcitrant polysaccharides. *Science*, 330 (6001): 219-222. doi: 10.1126/science.1192231.

Wang, B. J., Johnston, E. M., Li, P. F., Shaik, S., Davies, G. J., Walton, P. H. & Rovira, C. (2018). QM/MM studies into the H2O2-dependent activity of lytic polysaccharide monooxygenases: evidence for the formation of a caged hydroxyl radical intermediate. *ACS Catalysis*, 8 (2): 1346-1351. doi: 10.1021/acscatal.7b03888.

Westereng, B., Agger, J. W., Horn, S. J., Vaaje-Kolstad, G., Aachmann, F. L., Stenstrom, Y. H. & Eijsink, V. G. H. (2013). Efficient separation of oxidized cello-oligosaccharides generated by cellulose degrading lytic polysaccharide monooxygenases. *Journal of Chromatography A*, 1271: 144-152. doi: 10.1016/j.chroma.2012.11.048.

Williams, N. (2008). Biofuel debate deepens. *Current Biology*, 18 (19): R891-R892. doi: 10.1016/j.cub.2008.09.020.

Wolfenden, R., Lu, X. D. & Young, G. (1998). Spontaneous hydrolysis of glycosides. *Journal of the American Chemical Society*, 120 (27): 6814-6815. doi: 10.1021/ja9813055.

Wu, M., Beckham, G. T., Larsson, A. M., Ishida, T., Kim, S., Payne, C. M., Himmel, M. E., Crowley, M. F., Horn, S. J., Westereng, B., et al. (2013). Crystal structure and computational characterization of the lytic polysaccharide monooxygenase GH61D from the Basidiomycota fungus Phanerochaete chrysosporium. *Journal of Biological Chemistry*, 288 (18): 12828-12839. doi: 10.1074/jbc.M113.459396.

Zamocky, M., Schumann, C., Sygmund, C., O'Callaghan, J., Dobson, A. D. W., Ludwig, R., Haltrich, D. & Peterbauer, C. K. (2008). Cloning, sequence analysis and heterologous expression in Pichia pastoris of a gene encoding a thermostable cellobiose dehydrogenase from Myriococcum thermophilum. *Protein Expression and Purification*, 59 (2): 258-265. doi: 10.1016/j.pep.2008.02.007.

Zikakis, J. P. (1984). *Chitin, chitosan, and related enzymes*: Orlando : Academic Press.

Zugenmaier, P. (2001). Conformation and packing of various crystalline cellulose fibers. *Progress in Polymer Science*, 26 (9): 1341-1417. doi: 10.1016/s0079-6700(01)00019-3.

ZymoResearch. (2021). *DNA clean & concentrator®-5*. Version: 1.3.1 Cat. no. D4014.

Østby, H., Jameson, J. K., Costa, T., Eijsink, V. G. H. & Arntzen, M. O. (2022). Chromatographic analysis of oxidized cello-oligomers generated by lytic polysaccharide monooxygenases using dual electrolytic eluent generation. *Journal of Chromatography A*, 1662: 11. doi: 10.1016/j.chroma.2021.462691.

Aachmann, F. L., Sorlie, M., Skjak-Braek, G., Eijsink, V. G. H. & Vaaje-Kolstad, G. (2012). NMR structure of a lytic polysaccharide monooxygenase provides insight into copper binding, protein dynamics, and substrate interactions. *Proceedings of the National Academy of Sciences of the United States of America*, 109 (46): 18779-18784. doi: 10.1073/pnas.1208822109.

Appendix

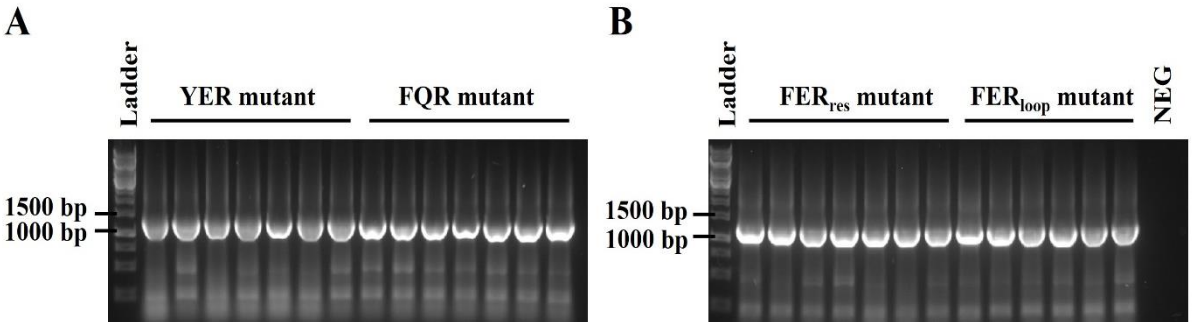

Figure A 1. PCR screen of MaLPMO10B mutants transformed into E. coli BL21 (DE3). *(A) PCR screen for the YER double mutant and FQR single mutant transformed into E. coli BL21 (DE3). (B) PCR screen for the FER*$_{res}$ *and FER*$_{loop}$ *single mutants transformed into E. coli BL21 (DE3). All images display the ladder on the left side where 1000 bp and 1500 bp are labelled. The negative control (NEG) contains the reaction mix without a colony sample.*

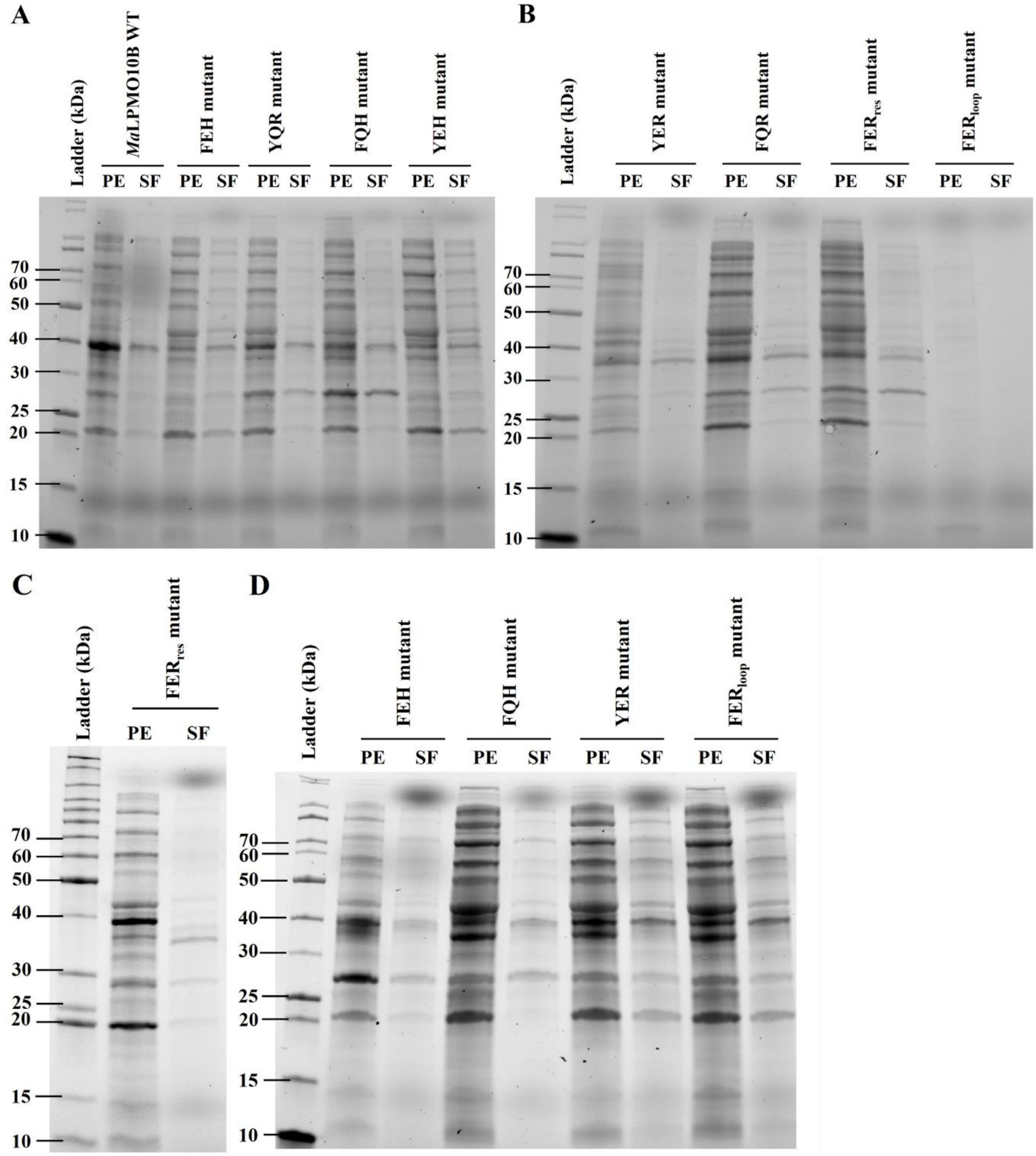

Figure A 2. SDS-PAGE gel of the expression test on MaLPMO10B mutants at 30 °C and 37 °C. *(A) Expression test of MaLPMO10B WT, the FEH mutant, YQR mutant, FQH mutant, and YEH mutant at 30 °C. (B) Expression test of the YER, FQR, FER$_{res}$, and FER$_{loop}$ mutants at 30 °C. (C) Expression test of the FER$_{res}$ mutant at 37 °C. (D) Expression test of the FEH, FQH, YER, and FER$_{loop}$ mutants at 37 °C. The expression tests show the periplasmic extract (PE) and the sucrose fraction (SF). The ladder on the left side of all images shows sizes of each band ranging from 10 to 70 kDa.*

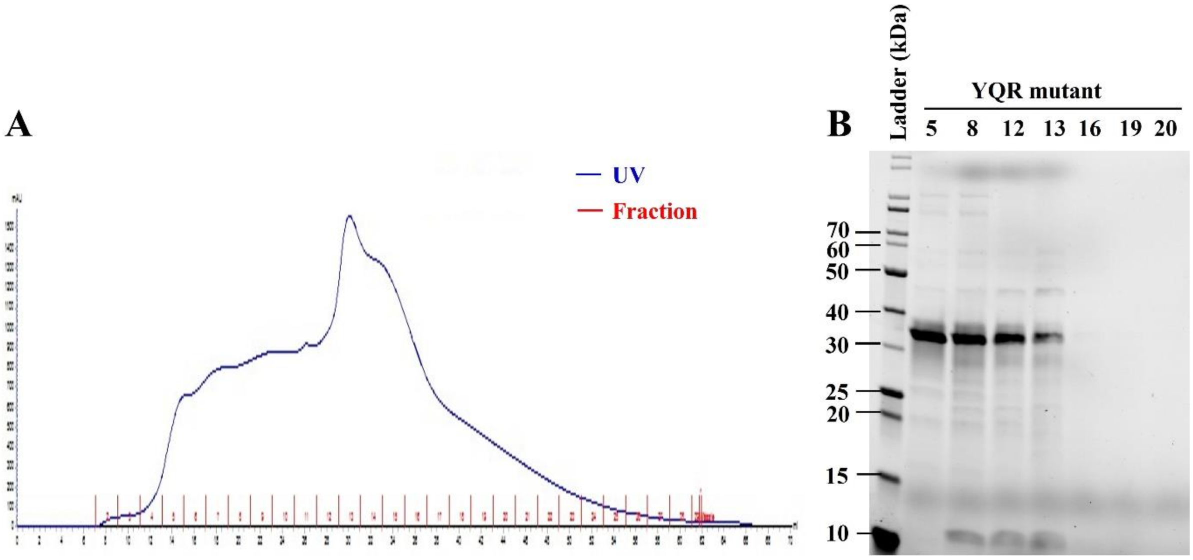

Figure A 3. Anion exchange chromatography of the YQR mutant. *(A) A representative example of anion exchange chromatography of the YQR mutant showing the UV signal obtained during binding of the periplasmic extract to the column. The Y-axis displays the UV absorbance (mAU) and the X-axis shows the volume of eluent used in mL. The UV trace line (blue) indicates protein eluting from the column and the red lines show the collected fractions. (B) SDS-PAGE analysis of the fractions collected during anion exchange chromatography. The ladder is located on the left, showing protein size in kDa. The numbers at the top of each well in (B) corresponds to the fractions (red) in (A).*

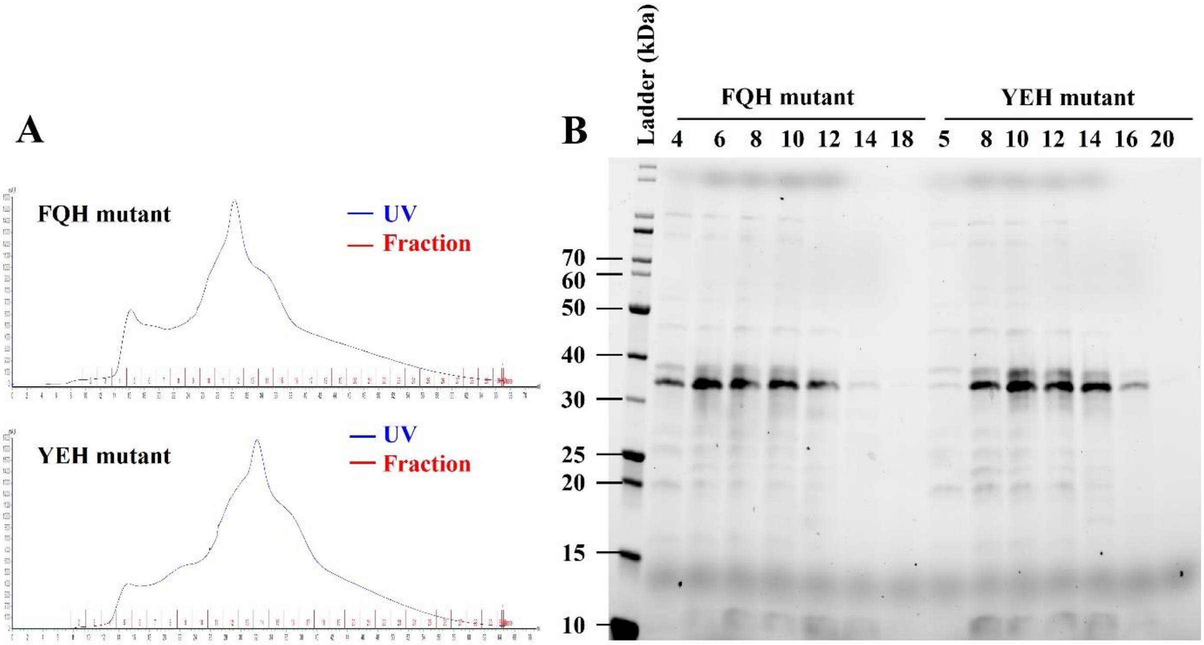

Figure A 4. Anion exchange chromatography of the FQH mutant and the YEH mutant. *(A) A representative example of anion exchange chromatography of the FQH mutant (top) and the YEH mutant (bottom) showing the UV signal obtained during binding of the periplasmic extract to the column. The Y-axis displays the UV absorbance (mAU) and the X-axis shows the volume of eluent used in mL. The UV trace line (blue) indicates protein eluting from the column and the red lines show the collected fractions. (B) SDS-PAGE analysis of the fractions collected during anion exchange chromatography. The ladder is located on the left, showing protein size in kDa. The numbers at the top of each well in (B) corresponds to the fractions (red) in (A).*

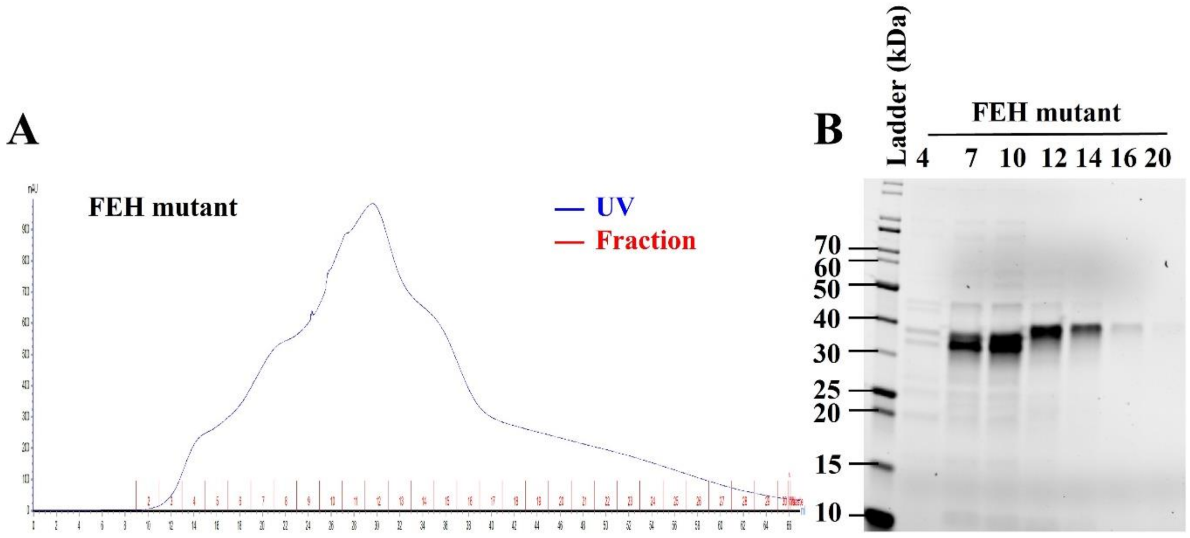

Figure A 5. Anion exchange chromatography of the FEH mutant. *(A) A representative example of anion exchange chromatography of the FEH mutant showing the UV signal obtained during binding of the periplasmic extract to the column. The Y-axis displays the UV absorbance (mAU) and the X-axis shows the volume of eluent used in mL. The UV trace line (blue) indicates protein eluting from the column and the red lines show the collected fractions. (B) SDS-PAGE analysis of the fractions collected during anion exchange chromatography. The ladder is located on the left, showing protein size in kDa. The numbers at the top of each well in (B) corresponds to the fractions (red) in (A).*

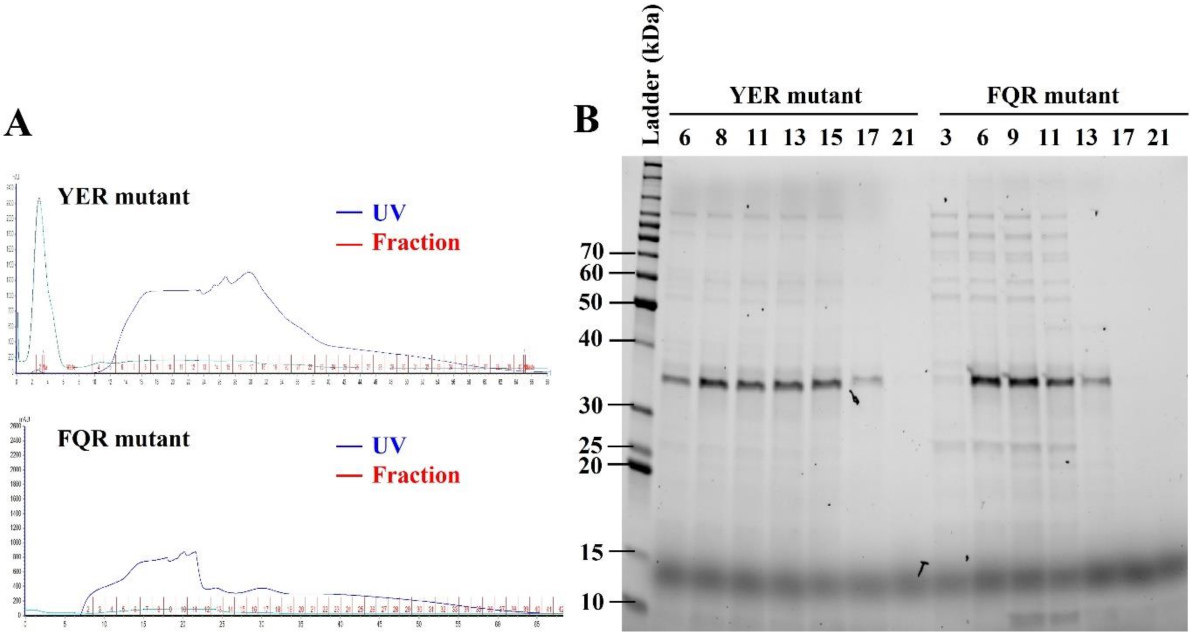

Figure A 6. Anion exchange chromatography of the YER mutant and the FQR mutant. *(A) A representative example of anion exchange chromatography of the YER mutant (top) and the FQR mutant (bottom) showing the UV signal obtained during binding of the periplasmic extract to the column. The Y-axis displays the UV absorbance (mAU) and the X-axis shows the volume of eluent used in mL. The UV trace line (blue) indicates protein eluting from the column and the red lines show the collected fractions. (B) SDS-PAGE analysis of the fractions collected during anion exchange chromatography. The ladder is located on the left, showing protein size in kDa. The numbers at the top of each well in (B) corresponds to the fractions (red) in (A).*

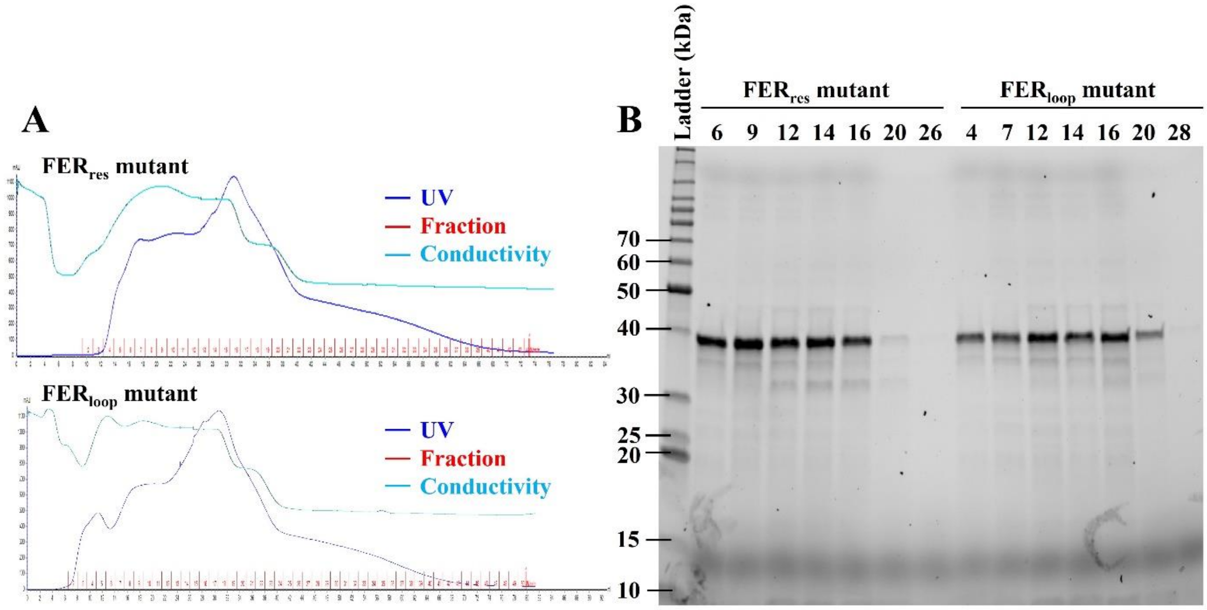

*Figure A 7. **Anion exchange chromatography of the FER$_{res}$ mutant and FER$_{loop}$ mutant.** (A) A representative example of anion exchange chromatography of the FER$_{res}$ mutant (top) and the FER$_{loop}$ mutant (bottom) showing the UV signal obtained during binding of the periplasmic extract to the column. The Y-axis displays the UV absorbance (mAU) and the X-axis shows the volume of eluent used in mL. The UV trace line (dark blue) indicates protein eluting from the column. The light blue trace line displays the conductivity over the column and the red lines show the collected fractions. (B) SDS-PAGE analysis of the fractions collected during anion exchange chromatography. The ladder is located on the left, showing protein size in kDa. The numbers at the top of each well in (B) corresponds to the fractions (red) in (A).*

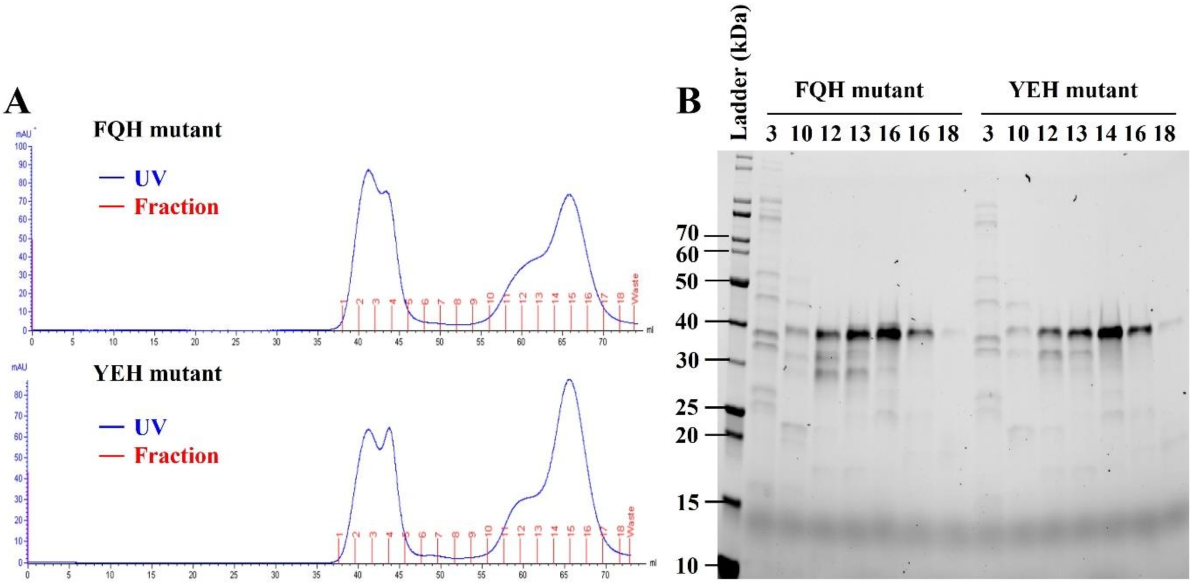

*Figure A 8. **Size exclusion chromatography of the FQH mutant and the YEH mutant.** (A) A representative example of SEC performed on the FQH mutant (top) and the YEH mutant (bottom). The Y-axis shows the UV absorbance (mAU) and the X-axis shows the volume of eluent in mL used during elution of the protein. The UV trace line (blue) indicates protein eluting from the column and the red lines show the fractions that were collected. (B) SDS-PAGE analysis of the fractions collected during SEC of the FQH mutant and the YEH mutant. The ladder is displayed on the left side and show protein size in kDa. The numbers on the top in (B) correspond to the fractions (red) in (A).*

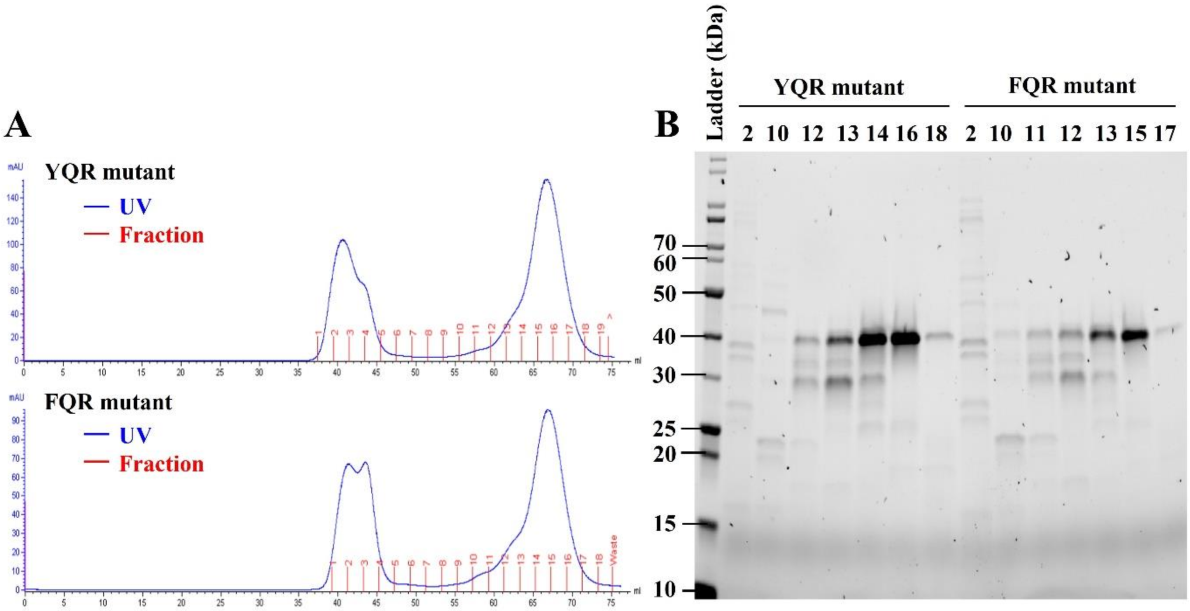

Figure A 9. Size exclusion chromatography of the YQR mutant and the FQR mutant. (A) A representative example of SEC performed on the YQR mutant (top) and the FQR mutant (bottom). The Y-axis shows the UV absorbance (mAU) and the X-axis shows the volume of eluent in mL used during elution of the protein. The UV trace line (blue) indicates protein eluting from the column and the red lines show the fractions that were collected. (B) SDS-PAGE analysis of the fractions collected during SEC of the YQR mutant and the FQR mutant. The ladder is displayed on the left side and show protein size in kDa. The numbers on the top in (B) correspond to the fractions (red) in (A).

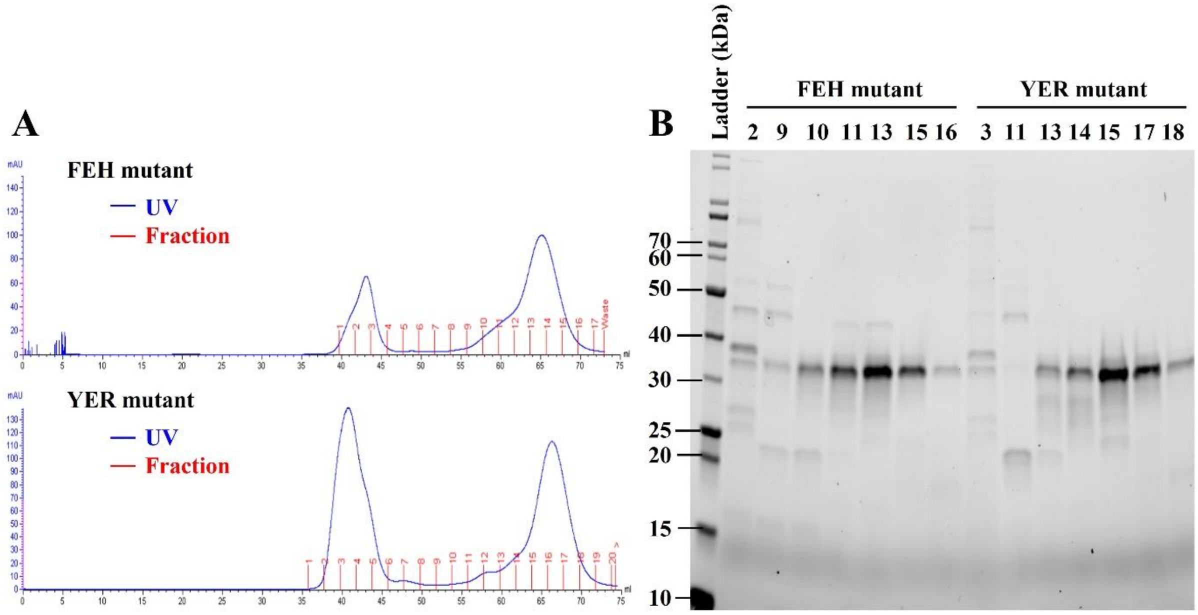

Figure A 10. Size exclusion chromatography of the FEH mutant and the YER mutant. (A) A representative example of SEC performed on the FEH mutant (top) and the YER mutant (bottom). The Y-axis shows the UV absorbance (mAU) and the X-axis shows the volume of eluent in mL used during elution of the protein. The UV trace line (blue) indicates protein eluting from the column and the red lines show the fractions that were collected. (B) SDS-PAGE analysis of the fractions collected during SEC of the FEH mutant and the YER mutant. The ladder is displayed on the left side and show protein size in kDa. The numbers on the top in (B) correspond to the fractions (red) in (A).

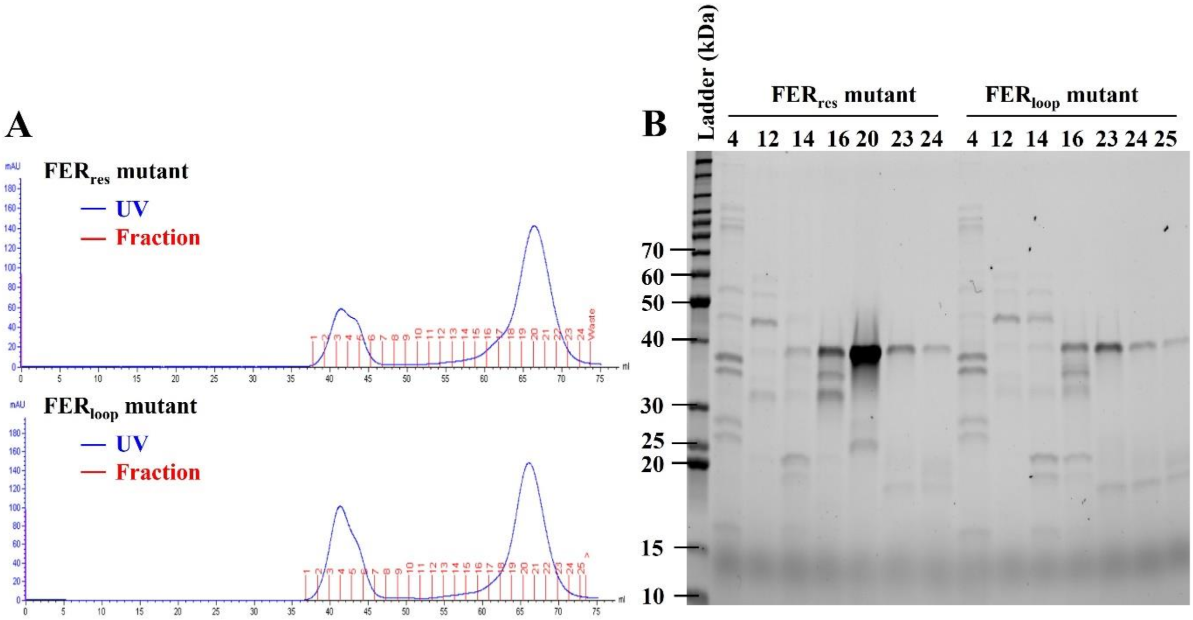

Figure A 11. Size exclusion chromatography of the FER$_{res}$ mutant and the FER$_{loop}$ mutant. *(A) A representative example of SEC performed on the FER$_{res}$ mutant (top) and the FER$_{loop}$ mutant (bottom). The Y-axis shows the UV absorbance (mAU) and the X-axis shows the volume of eluent in mL used during elution of the protein. The UV trace line (blue) indicates protein eluting from the column and the red lines show the fractions that were collected. (B) SDS-PAGE analysis of the fractions collected during SEC of the FER$_{res}$ mutant and the FER$_{loop}$ mutant. The ladder is displayed on the left side and show protein size in kDa. The numbers on the top in (B) correspond to the fractions (red) in (A).*

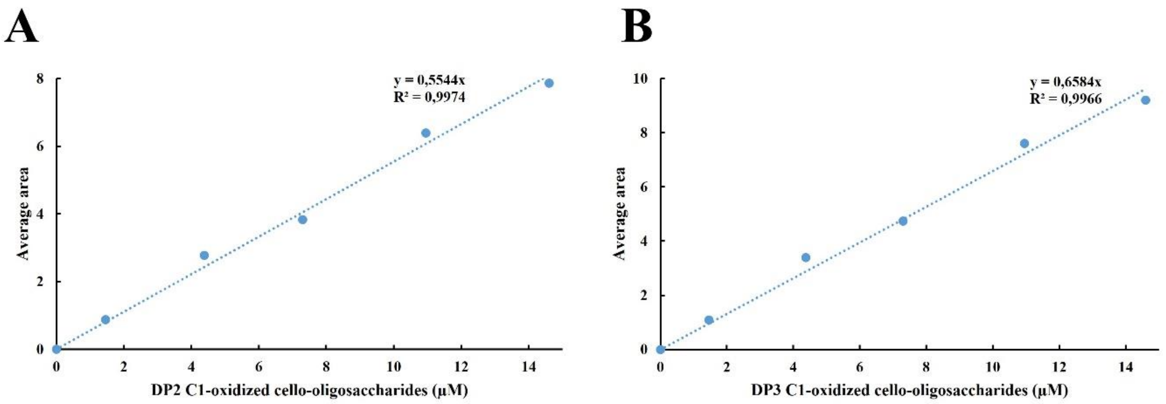

Figure A 12. Standard curve of DP2 and DP3 C1-oxidized cello-oligosaccharides. *A representative example of a standard curve for (A) DP2 and (B) DP3 C1-oxidized cello-oligosaccharides. The Y-axis displays the average peak area of three independent replicates and the X-axis shows the concentration of (A) DP2 or (B) DP3 C1-oxidized cello-oligosaccharides in µM. The regression line and the R^2 value are shown.*

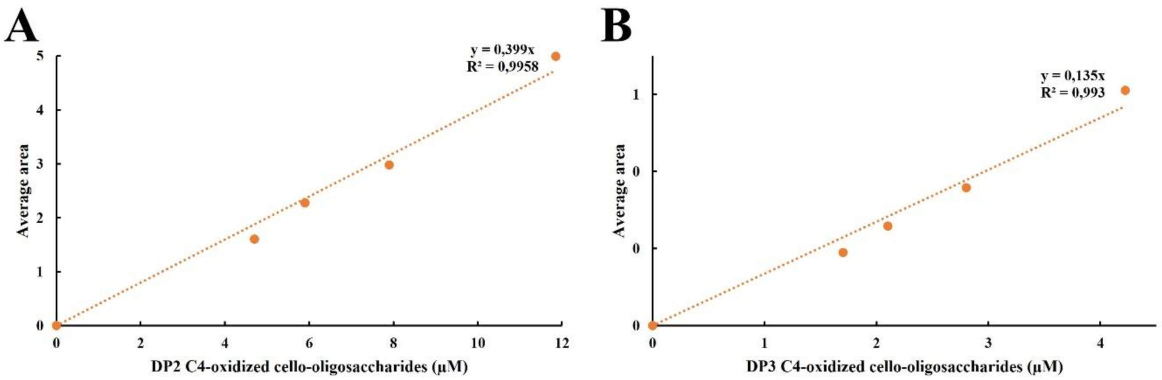

Figure A 13. Standard curve of DP2 and DP3 C4-oxidized cello-oligosaccharides. *A representative example of a standard curve for (A) DP2 and (B) DP3 C4-oxidized cello-oligosaccharides. The Y-axis displays the average peak area of three independent replicates and the X-axis shows the concentration of (A) DP2 or (B) DP3 C4-oxidized cello-oligosaccharides in µM. The regression line and the* R^2 *value are shown.*

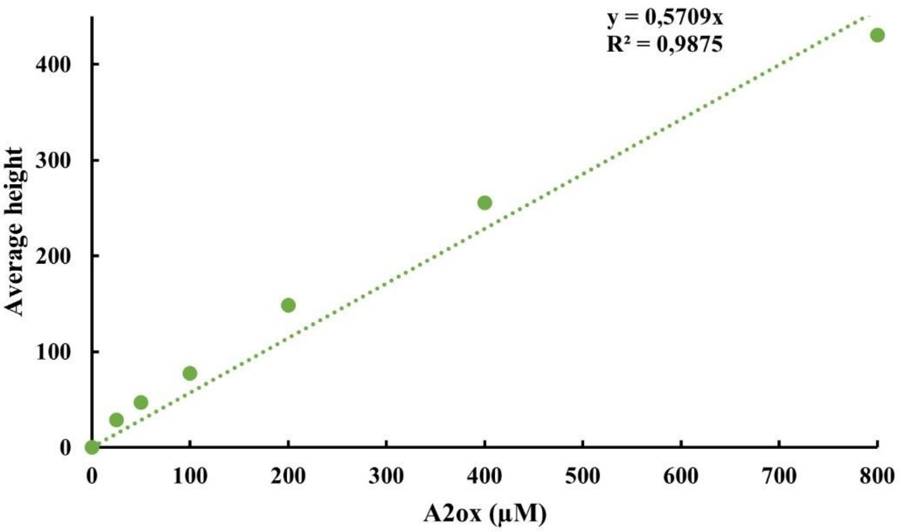

Figure A 14. Standard curve of A2ox. *The standard curve of A2ox product used to calculate the product concentration upon degradation of β-chitin. The Y-axis displays the average peak height of three independent replicates and the X-axis shows the concentration of A2ox in µM. The regression line and the* R^2 *value are shown.*

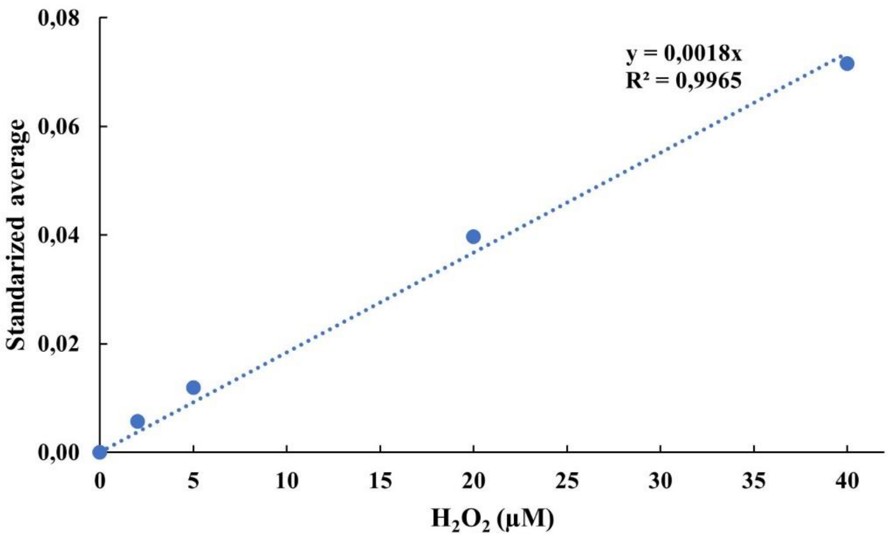

Figure A 15. Standard curve of H_2O_2. *A representative example of a standard curve for H_2O_2 used to calculate the concentration of H_2O_2 in the amplex red assays. The Y-axis displays the standardized average of three independent replicates and the X-axis shows the concentration of H_2O_2 in µM. The regression line and the R^2 value are shown.*

Table A 1. The amino acid sequences of MaLPMO10B WT and the mutants with signal peptide (yellow), catalytic domain (no color), linker region (green), and CBM (cyan). The mutated amino acids are highlighted in red.

Amino acid code	**Amino acid sequence**
WT - YQH	MSTPYRRPLPLAAAILGVCAVVAALLTTAFSGPASAHGSVVDPASRSYSCWQRWGGDFQNPAMATQDPMCWQAWQADPNAMWNWNGLFREGVAGNHQGAIPDGQLCSGGRTQSGRYNALDTVGAWKTVPVTNNFRVKFFDQASHGADYIRVYVTKQGYNALTSPLRWSDLELVGQIGNTPASQWTREVDGVSIQIPANAPGRTGRHVVYTIWQASHLDQSYYLCSDVDFGGSGPTTPPTSTPPTSTPPTSTPPTSPPPTTPNPAGGCTATYAITGSWGGGFQADVKVTNGSGSPIRGWSVSWNYQNGQQVNSAWNATVTTSGTLVTARNVAYNGSLAPGASTSFGFTGSAGATNPVPSIVSCTTTS
YQR (A214R, H216G)	MSTPYRRPLPLAAAILGVCAVVAALLTTAFSGPASAHGSVVDPASRSYSCWQRWGGDFQNPAMATQDPMCWQAWQADPNAMWNWNGLFREGVAGNHQGAIPDGQLCSGGRTQSGRYNALDTVGAWKTVPVTNNFRVKFFDQASHGADYIRVYVTKQGYNALTSPLRWSDLELVGQIGNTPASQWTREVDGVSIQIPANAPGRTGRHVVYTIWQRSGLDQSYYLCSDVDFGGSGPTTPPTSTPPTSTPPTSTPPTSPPPTTPNPAGGCTATYAITGSWGGGFQADVKVTNGSGSPIRGWSVSWNYQNGQQVNSAWNATVTTSGTLVTARNVAYNGSLAPGASTSFGFTGSAGATNPVPSIVSCTTTS
FQH (Y221F)	MSTPYRRPLPLAAAILGVCAVVAALLTTAFSGPASAHGSVVDPASRSYSCWQRWGGDFQNPAMATQDPMCWQAWQADPNAMWNWNGLFREGVAGNHQGAIPDGQLCSGGRTQSGRYNALDTVGAWKTVPVTNNFRVKFFDQASHGADYIRVYVTKQGYNALTSPLRWSDLELVGQIGNTPASQWTREVDGVSIQIPANAPGRTGRHVVYTIWQASHLDQSFYLCSDVDFGGSGPTTPPTSTPPTSTPPTSTPPTSPPPTTPNPAGGCTATYAITGSWGGGFQADVKVTNGSGSPIRG

	WSVSWNYQNGQQVNSAWNATVTTSGTLVTARNVAYNGSLAPGASTSFGFTGSAGATNPVPSIVSCTTTS
YEH (Q219E)	MSTPYRRPLPLAAAILGVCAVVAALLTTAFSGPASAHGSVVDPASRSYSCWQRWGGDFQNPAMATQDPMCWQAWQADPNAMWNWNGLFREGVAGNHQGAIPDGQLCSGGRTQSGRYNALDTVGAWKTVPVTNNFRVKFFDQASHGADYIRVYVTKQGYNALTSPLRWSDLELVGQIGNTPASQWTREVDGVSIQIPANAPGRTGRHVVYTIWQASHLDESYYLCSDVDFGGSGPTTPPTSTPPTSTPPTSTPPTSPPPTTPNPAGGCTATYAITGSWGGGFQADVKVTNGSGSPIRGWSVSWNYQNGQQVNSAWNATVTTSGTLVTARNVAYNGSLAPGASTSFGFTGSAGATNPVPSIVSCTTTS
FEH (Q219E, Y221F)	MSTPYRRPLPLAAAILGVCAVVAALLTTAFSGPASAHGSVVDPASRSYSCWQRWGGDFQNPAMATQDPMCWQAWQADPNAMWNWNGLFREGVAGNHQGAIPDGQLCSGGRTQSGRYNALDTVGAWKTVPVTNNFRVKFFDQASHGADYIRVYVTKQGYNALTSPLRWSDLELVGQIGNTPASQWTREVDGVSIQIPANAPGRTGRHVVYTIWQASHLDESFYLCSDVDFGGSGPTTPPTSTPPTSTPPTSTPPTSPPPTTPNPAGGCTATYAITGSWGGGFQADVKVTNGSGSPIRGWSVSWNYQNGQQVNSAWNATVTTSGTLVTARNVAYNGSLAPGASTSFGFTGSAGATNPVPSIVSCTTTS
YER (A214R, H216G, Q219E)	MSTPYRRPLPLAAAILGVCAVVAALLTTAFSGPASAHGSVVDPASRSYSCWQRWGGDFQNPAMATQDPMCWQAWQADPNAMWNWNGLFREGVAGNHQGAIPDGQLCSGGRTQSGRYNALDTVGAWKTVPVTNNFRVKFFDQASHGADYIRVYVTKQGYNALTSPLRWSDLELVGQIGNTPASQWTREVDGVSIQIPANAPGRTGRHVVYTIWQRSGLDESYYLCSDVDFGGSGPTTPPTSTPPTSTPPTSTPPTSPPPTTPNPAGGCTATYAITGSWGGGFQADVKVTNGSGSPIRGWSVSWNYQNGQQVNSAWNATVTTSGTLVTARNVAYNGSLAPGASTSFGFTGSAGATNPVPSIVSCTTTS
FQR (A214R, H216G, Y221F)	MSTPYRRPLPLAAAILGVCAVVAALLTTAFSGPASAHGSVVDPASRSYSCWQRWGGDFQNPAMATQDPMCWQAWQADPNAMWNWNGLFREGVAGNHQGAIPDGQLCSGGRTQSGRYNALDTVGAWKTVPVTNNFRVKFFDQASHGADYIRVYVTKQGYNALTSPLRWSDLELVGQIGNTPASQWTREVDGVSIQIPANAPGRTGRHVVYTIWQRSGLDQSFYLCSDVDFGGSGPTTPPTSTPPTSTPPTSTPPTSPPPTTPNPAGGCTATYAITGSWGGGFQADVKVTNGSGSPIRGWSVSWNYQNGQQVNSAWNATVTTSGTLVTARNVAYNGSLAPGASTSFGFTGSAGATNPVPSIVSCTTTS
FER$_{res}$ (A214R, H216G, Q219E, Y221F)	MSTPYRRPLPLAAAILGVCAVVAALLTTAFSGPASAHGSVVDPASRSYSCWQRWGGDFQNPAMATQDPMCWQAWQADPNAMWNWNGLFREGVAGNHQGAIPDGQLCSGGRTQSGRYNALDTVGAWKTVPVTNNFRVKFFDQASHGADYIRVYVTKQGYNALTSPLRWSDLELVGQIGNTPASQWTREVDGVSIQIPANAPGRTGRHVVYTIWQRSGLDESFYLCSDVDFGGSGPTTPPTSTPPTSTPPTSTPPTSPPPTTPNPAGGCTATYAITGSWGGGFQADVKVTNGSGSPIRGWSVSWNYQNGQQVNSAWNATVTTSGTLVTARNVAYNGSLAPGASTSFGFTGSAGATNPVPSIVSCTTTS

FER$_{loop}$ (A214R, H216D, L217S, D218Q, Q219E, Y221F)	MSTPYRRPLPLAAAILGVCAVVAALLTTAFSGPASAHGSVVDPASRSYSCWQRWGGDFQNPAMATQDPMCWQAWQADPNAMWNWNGLFREGVAGNHQGAIPDGQLCSGGRTQSGRYNALDTVGAWKTVPVTNNFRVKFFDQASHGADYIRVYVTKQGYNALTSPLRWSDLELVGQIGNTPASQWTREVDGVSIQIPANAPGRTGRHVVYTIWQRSDSQESFYLCSDVDFGGSGPTTPPTSTPPTSTPPTSTPPTSPPPTTPNPAGGCTATYAITGSWGGGFQADVKVTNGSGSPIRGWSVSWNYQNGQQVNSAWNATVTTSGTLVTARNVAYNGSLAPGASTSFGFTGSAGATNPVPSIVSCTTTS

Norges miljø- og biovitenskapelige universitet
Noregs miljø- og biovitskapelege universitet
Norwegian University of Life Sciences

Postboks 5003
NO-1432 Ås
Norway